Cell instructive biomaterials for neural tissue engineering

David Lomboni

Thesis submitted to the University of Ottawa in partial Fulfillment of the requirements for the

Doctor of Philosophy degree in Biomedical Engineering

Supervisor: Dr. Fabio Variola

Department of Biomedical Engineering

Faculty of Engineering

University of Ottawa

uOttawa

ACKNOWLEDGEMENTS

Firstly, I would like to express my most sincere gratitude to my supervisor, Dr. Fabio Variola, for giving me the opportunity to work in his lab at the University of Ottawa, and for his excellent mentorship, guidance, trust and support all these years.

I would also like to thank my OCIBME committee members, Dr. Xudong Cao, Dr. Michel Godin and Dr. Andrew Harris, as well as my external committee member, Dr. Houman Savoji, for dedicating their time and effort to reviewing my thesis.

I would like to take the opportunity to thank Dr. William Staines at the Cellular and Molecular Medicine (CMM) department of the University of Ottawa for giving me access to his cell culture lab as well as Dr. Chloe Van Oostende-Triple and the staff at CBIA Microscope core facility for their immense support and guidance in Microscopy and Image analysis.

I would also like to thank the current and former members of the Variola research group for their constant support and for creating a very positive and enjoyable work environment.

I would like to deeply thank Dr. Alp Ozgun for teaching me new techniques and for his great support and guidance. Your expertise in various techniques has been invaluable, but what I cherish the most are the coffee breaks we shared.

I would also like to express my sincere gratitude to my lab mates Alexander Steeves and Ryan Berthelot, who have both made my experience in the lab and transition to Canada significantly easier.

I would also like to thank my parents-in-law, Mario and Angela, for embracing me in their family as their son and for their great support during this journey.

Last but not least, I would like to express my deepest gratitude to my family members. Thanks mom, dad and Lois for always supporting my choice and for cheering me up from Italy.

I want to dedicate this thesis to my wife RoseMarie Addesa. You are the reason why 5 years ago I decided to stay in Canada and started my doctoral studies. You have been a constant source of inspiration and support during the challenges and difficult times. Thank you for always being there. I cannot wait to be reunited and start our life together.

ABSTRACT

Cells in multicellular organisms are surrounded by a complex three-dimensional macromolecular extracellular matrix (ECM). This matrix, traditionally thought to uniquely serve a structural function providing support and strength to cells within tissues, is increasingly being recognized to have pleiotropic effects in neurogenesis and regeneration processes such as neocortex folding, stem cell niche maintenance, peripheral nerve regeneration, axonal growth, and many more. ECM mediates these processes via cell-ECM interactions which provide the cells with a wealth of signals including biophysical and mechanical cues in a spatiotemporal manner. Owing to the importance of the surrounding microenvironment, modern neural tissue engineering strategies have focused on the development of engineered biomaterials capable of finely instructing the neuronal response according to their physicochemical characteristics. Neurons and neural stem cells are in fact sensitive to their mechanical and topographical environment, and cell–substrate binding contributes to this sensitivity by activating specific signaling pathways for basic cell function. In addition, the advances in nanotechnology have opened the possibility of introducing decorative nano-motifs that interact with cells at the molecular level. Successful strategies in tissue engineering are driven by not only advances in the synthesis of highly instructive biomaterials but also greatly depend on the right selection of cell sources. As a matter of fact, advances in neural tissue engineering have been strongly hampered by the poor availability of cell sources, considering that primary neurons are the only type of cells that do not proliferate. The discovery of induced pluripotent stem cells (iPSCs) has addressed many of the cell-related limitations in neural tissue engineering, offering the possibility to consistently produce a wide range of neural cell lines. Advances in cell biology have led to the development of iPSCs-derived brain spheroid, which surely represent the most promising tools for several neural tissue engineering applications

ranging from *in vitro* modelling of neurodegenerative diseases (i.e., Parkinson's, Huntington's and Alzheimer's), biomaterials testing and drug screening platforms.

The overarching goal of my doctoral work was to engineer biomaterials with instructive physicochemical properties to elicit beneficial cellular responses that are suitable for different neural tissue engineering applications such as nerve regeneration and 3D *in vitro* modelling.

In the first study (**Chapter 2**), I evaluated the compounded effects of surface stiffness and micro-topography on dorsal root ganglion and human bone-marrow mesenchymal stem cells behavior. To this end, arrays of parallel microchannels of different geometries were introduced on the surface of chitosan films by electrophoretic replica deposition. In addition, a novel chemical crosslinking with citric acid was performed to both enhance the long-term stability of the chitosan films and fine-tune the surface stiffness for the investigation of its role in cell behavior.

In the second study (**Chapter 3**), I developed a novel nanocomposite consisting of a collagen hydrogel decorated with glycine-derived carbon nanodots (Gly-CNDs). After a comprehensive physicochemical characterization of the resulting nanocomposite, I evaluated the effects exerted on neuronal differentiation and electrophysiological maturation of mouse iPSCs-derived brain spheroid.

In the third study (**Chapter 4**), I optimized an alignable collagen-based hydrogel characterized by anisotropically oriented fibers with potential applications in both peripheral and central nervous system repair. I established a protocol that encompasses the introduction in the collagen solution of biodegradable laminin-functionalized magnetic microbeads and the time-controlled application of an external magnetic field. The regenerative potential of the hydrogel was unveiled using mouse iPSCs-derived neural stem cells.

STATEMENT OF ORIGINALITY

I, David J. Lomboni, state that the content of this Thesis is entirely original. The research and the corresponding manuscripts were done under the supervision of Dr. Fabio Variola, cross-appointed professor in both the Department of Mechanical Engineering and the Department of Cellular and Molecular Medicine at the University of Ottawa. The research presented in this Thesis consists of two experimental research manuscripts that have been either published (**Chapter 2****) or submitted for peer-reviewed scientific journals (**Chapter 3**) and a third one that is in the preparation stage (**Chapter 4**). Finally, the general thesis conclusions are discussed in **Chapter 5**.

Manuscripts included in this Thesis:

- Lomboni D.J., Steeves A.J., Schock S., Bonetti L., De Nardo L., Variola F., "Compounded topographical and physicochemical cueing by micro-engineered chitosan substrates on rat dorsal root ganglion neurons and human mesenchymal stem cells", *Soft Matter,* 17 (21), 2021.
- Ozgun A.*, Lomboni D.J.*, Arnott H., Staines W.A., Woulfe J., Variola F. "Biomaterials-based strategies for in vitro neural models", *Biomaterials Science*, 10(5), 2022. * *co-first author*
- Lomboni D.J., Ozgun A., de Medeiros T.V., Staines W., Woulfe J., Naccache R., Variola F., "Electroconductive Collagen-Carbon Nanodots nanocomposite elicits neurite outgrow, supports neurogenic differentiation and accelerates electrophysiological maturation of neural progenitor spheroids", *Advanced Healthcare Materials*, 2301894, 2023.

*** The preparation and optimization of the samples presented in this study was performed during my Master's thesis at Politecnico di Milano (Italy). Most of the material characterization and the totality of cell culture work was performed during my PhD. To ensure completeness, the full research (which was published in 2021 in a peer-reviewed article is presented.*

STATEMENT OF CONTRIBUTIONS

I, David J. Lomboni, contributed to most of the work presented in this Thesis. Firstly, I established the protocols that were employed to develop the biomaterials presented. I performed the vast majority of both material characterization and cell culture work. Moreover, I was the sole trust behind the experimental components of the research projects, which included confocal imaging, multi-electrode arrays (MEAs), as well as the analysis of images and data. I also took a primary role in the drafting of the scientific papers that are included in this Thesis.

STATEMENT OF OTHER CONTRIBUTIONS

While completing my Ph.D. thesis work, I also participated in the work and preparation of several publications. Additionally, the second study (**Chapter 3**) led to the preparation of a provisional patent. The details of all other contributions are listed below:

- Steeves A.J., Ho W., Munisso M.C., Lomboni D.J., Larranaga E., Omelon S., Martinez E., Spinello D., Variola F. "The implication of spatial statistics in human mesenchymal stem cell response to nanotubular architectures", *Int J Nanomedicine*, 15, 2020.

- Steeves A.J., Lomboni D.J., Vijay M., Tieu A. & Variola F. "Direct cueing by pulsed-waterjet treated titanium on fibroblast, osteoblastic and human stem cells for prospective use in dental implants", *Materials Letters*, 290, 2021.

- Munoz M., El-Khoury A., Cimenci C.E., Gonzalez-Gomez M., Hunter R.A., Lomboni D.J., Variola F, Rotstein B.H., Vono L.R., Rossi L.M., Edwards A.M., Alarcon E.I. "Riboflavin Surface Modification of Poly(vinyl chloride) for Light-Triggered Control of Bacterial Biofilm and Virus Inactivation", *ACS Appl Mater Interfaces*, 13(27), 2021.

- Ozgun A., Lomboni D.J., Staines W., Woulfe J., Variola F.," Unraveling the Assembloid: Real-Time Monitoring of Dopaminergic Neurites in an Inter-Organoid Pathway Connecting Midbrain and Striatal Regions", revisions requested, *Materials Today Bio*.

GENERAL OVERVIEW AND RATIONALE

Every year, traumatic injuries to the nervous system affect millions of people worldwide leading, in most cases, to life-long disability in patients, reduced quality of life and heavy economic and social burdens. Both peripheral (PNS) and central nervous system (CNS) are characterized by the formation of a highly impeding post-traumatic environment (i.e., glial scar formation) that ultimately impedes the complete functional restoration of the tissue. Nowadays, conventional medicine does not offer effective and successful treatments for traumatic injuries, and mitigating the symptoms is often the only solution. To address this clinical need, neural tissue engineering has emerged as a promising alternative that capitalizes on the use of versatile and highly engineered biomaterials to elicit desirable cellular responses. As a result of the concomitant advances of biomaterial fabrication techniques (i.e., nanoparticle synthesis, 3D bioprinting) and cell biology (i.e., induced pluripotent stem cells, advanced cell culture systems) it is now possible to exploit sophisticated *in vitro* models that enable the investigation of complex cellular activities that resemble the *in vivo* conditions, thereby offering a critical path toward the clinical translation of neural tissue engineering constructs. From a material standpoint, it is fundamental to recreate a biomimetic environment that offers specific cues that ultimately lead to desirable cellular outcome (i.e., contact guidance, neurite growth, electrophysiological maturation and neuronal differentiation). In addition, a deeper understanding of the signaling pathways initiated by the intrinsic physicochemical and structural properties of a biomaterial can unveil novel mechanistic insight and ultimately foster superiorly designed constructs able to elicit unique cellular responses.

Owing to the determining role play by the surrounding microenvironment's physicochemical properties, my doctoral work was mainly focused on the development of novel instructive biomaterials to elicit favourable cellular responses suitable for neural tissue engineering applications.

SPECIFIC OBJECTIVES

Objective 1 (Chapter 2)

Despite the well-known structure-function relationships governing cellular responses at interfaces, most studies have overlooked the compounded physicochemical and topographical effects exerted by the surrounding microenvironment on cell behavior. Focusing on the role of dissociated variables (i.e., surface topography, substrate's elasticity) does not provide a realistic representation of the *in vivo* complexity of cell-biomaterial interactions. In this study, I aimed at creating chitosan-based testing platforms offering variable surface micro-topography and tunable mechanical properties, thus enabling the evaluation of the compounded effects exerted on cellular responses by these two variables. To this end, I employed electrophoretic replica deposition to engender the surface of the deposited chitosan film with arrays of parallel micro-channel with variable width (i.e., 20 and 60 um). In addition, the mechanical properties and chemical make-up of the chitosan substrates were finely tuned by the application of a novel chemical crosslinking based on citric acid followed by a high temperature treatment. Bone marrow-derived human mesenchymal stem cells (hMSCs) and rat dorsal root ganglia (DRGs) neurons were employed to investigate the concerted topographical and physicochemical properties effects. This study provides novel insights into the interplay between chitosan's physicochemical properties and the activity of relevant cells for neural tissue engineering applications.

Objective 2 (Chapter 3)

One of the fundamental design criteria for effective clinical translation emphasizes the use of biomaterials that recapitulate key physicochemical features of the intended target tissue. In the context of neural tissue engineering, recent findings have highlighted the pivotal role of electroconductivity in guiding several developmental processes associated with cell proliferation and synaptic plasticity. Based on this evidence, the use of electroconductive hydrogels has emerged as an effective approach to recapitulate the physicochemical and electrical microenvironment of neural tissues. The extensive body of literature which investigated the potential of these candidate electroconductive nanocomposites for neuro-regeneration, mostly employed simplified experimental conditions (e.g., conventional monolayer) that do not recapitulate the native ECM and/or adopted primary immortalized cells (i.e., PC12 and SH-SY5Y) that do not replicate the cellular phenotype of mature differentiated neurons, ultimately widening the gap between *in vitro* research and the *in vivo* reality.

To bridge this gap, I investigate a novel electroconductive nanocomposite consisting of glycine-derived carbon nanodots (GlyCNDs) incorporated into a collagen matrix and validate its beneficial physicochemical and electro-active cueing to relevant cells. To this end, I employed mouse induced pluripotent stem cell (miPSC)-derived neural progenitor (NP) spheroids and 3D cultures of primary neurons. The findings from this study establish a foundation for an innovative biomaterial-based tissue engineering approach aimed at addressing neuronal disorders by restoring damaged/lost neurons and reestablishing neuroanatomical connectivity.

Objective 3 (Chapter 4):

Mammalian neuronal cells exhibit a limited post-traumatic self-regeneration capability, necessitating the use of biomimetic scaffolds that facilitate supportive environments for neuronal regeneration. Throughout the years, it has been shown that guiding and directing neuronal outgrowth during the regeneration period can enhance neuronal repair and recovery. The extracellular topography has been shown to play a key role in the modulation of cellular responses that are relevant for neuronal regeneration. Several methods have been used to fabricate scaffolds with aligned fibrils as cell-directing cues including electrospinning, microfluidics strain-induced alignment. In all reported studies, scaffolds were designed and fabricated *ex-vivo*, prior to the interaction with the cells or implantation site. Facilitating scaffold alignment *in situ* is still a compelling challenge.

In this study, I developed a novel collagen-based hydrogel decorated with paramagnetic beads that can be remotely aligned via the application of a magnetic field. Despite such approach has already been reported, this study presents novel distinct attributes encompassing: i) the functionalization of the paramagnetic beads with laminin, a biomolecule well-known for its neuronal affinity, ii) the establishment of an optimized timing for magnetic induction during collagen fibrillogenesis, a parameter which influence in modulating the resulting fibers alignment has been overlooked in previous studies and, distinctively from the vast majority of previous work, iii) the use of a 3D culture system. The biological activity of the composite was characterized using iPSCs-derived NSCs and primary mouse neurons. This study shed new light on the influence of aligned collagen fibers in fostering early neuronal differentiation, providing some initial evidence of the potential underlying mechanotransduction pathways implicated.

LIST OF FIGURES

Introduction

Chapter2

Chapter3

Chapter4

Appendix

LIST OF TABLES

TABLE OF CONTENT

CHAPTER 1: INTRODUCTION

1.1 Biomaterial-driven strategies in neural tissue engineering

The interdisciplinary approach adopted in tissue engineering (TE) has significantly impacted its growth in the last decade. The assimilation of knowledge and technical advancements from different fields such as material science, nanotechnology, cell biology, and developmental biology have surely determined tissue engineering booming and advances. Novel biomaterial, three-dimensional (3D) bioprinting technologies,[1] integration of nanotechnology,[2] stem cell technologies such as induced pluripotent stem cells (iPSCs),[3,4] and gene editing technology[5] represent great advancements that have benefited TE in recent years. From a material standpoint, successful tissue engineering strategies encompass the use of novel biomaterials, structures, and a variety of cues that enable to finely control cell behavior and promote regeneration.[6,7] This is particularly important for neural tissue engineering as the post-traumatic microenvironment probably represents the most impeding factor for the complete functional recovery of the tissue. Chemical, mechanical, and topographic extracellular matrix (ECM) cues have been extensively studied for their influence on cell behavior. Neurons and neural stem cells, as most other type of cells, are in fact sensitive to their mechanical and topographical environment, and cell–substrate binding contributes to this sensitivity to activate signaling pathways for basic cell functions.[8,9] Improving our knowledge of substrate-mediated mechanotransduction in the study of neural cells has the potential to advance material design for regenerative medicine, investigate neurodegenerative diseases, and better understand neural stem cells (NSCs) differentiation. In the next sections, after a general overview of the structural and physicochemical properties of the neural ECM, the influence of topographical, mechanical and chemical properties of the material substrate on neuronal behavior will be discuss in detail.

1.1.1 Neural ECM

1.1.1.1 Biochemical, structural and physicochemical properties of native neural tissues

In the nervous system, a notable portion (20-30%) of neural tissue is situated within the ECM, which, as in many other tissues in the body, supports cellular networks by dynamically adapting its physical and chemical properties to the needs of the cells, and plays a major role in regulating tissue function.[10,11] Surrounding the ECM and making up most of the remaining tissue, are dense networks of neurons and glial cells which rely on the ECM to express unique functions. To support a wide variety of cellular processes, the neural ECM is organized into basement membrane, peri-neuronal nets and interstitial matrix[12] as illustrated in **Figure 1.1**. While the basement membrane serves as a boundary and supplies the primary adhesion points for cells,[13] peri-neuronal nets undertake critical roles in the nervous system during development and plasticity by structuring the inter-neuronal space and compartmentalizing soluble factors in a way that facilitates neurite outgrowth, synaptic maturation and functions.[14] Being comprised of mostly soluble molecules, the interstitial matrix constitutes the least dense component of the ECM and can readily adapt to the chemical and structural needs of the surrounding neurons and glia.[15,16] When compared to the majority of other tissues, the neural ECM contains relatively small amounts of fibrous proteins such as collagen, elastin and laminin. [17] These stabilizing structural components are known to inhibit axonal growth in the neural parenchyma and are largely isolated to the basement membrane.[18] The major structural component of the neural basement membrane is laminin, which binds cell-surface receptors to not only provide anchorage but also to convey signals critical for neurite outgrowth,[19] axonal pathfinding,[20] myelination[21] and blood-brain barrier integrity.[22] The most essential elements in the interstitial matrix are the proteoglycans.[23] This family of molecules is characterized by a core protein decorated with linear saccharides called glycosaminoglycans (GAGs). Negatively charged groups on these GAGs attract water molecules and cause swelling in the matrix,

leading to a loosely packed structure permissive to axonal growth and cell migration.[24] GAGs are further divided into 5 sub-families according to saccharide structure, namely: hyaluronic acid, chondroitin sulfate (CS), heparan sulfate, dermatan sulfate and keratan sulfate. Each member of these sub-families plays distinct roles in the interstitial matrix in neural tissue development, activity and response to pathologies.[25] CS proteoglycans are the most abundant family within neural ECM but, interestingly, they are also associated with inhibition of neurite growth.[26]

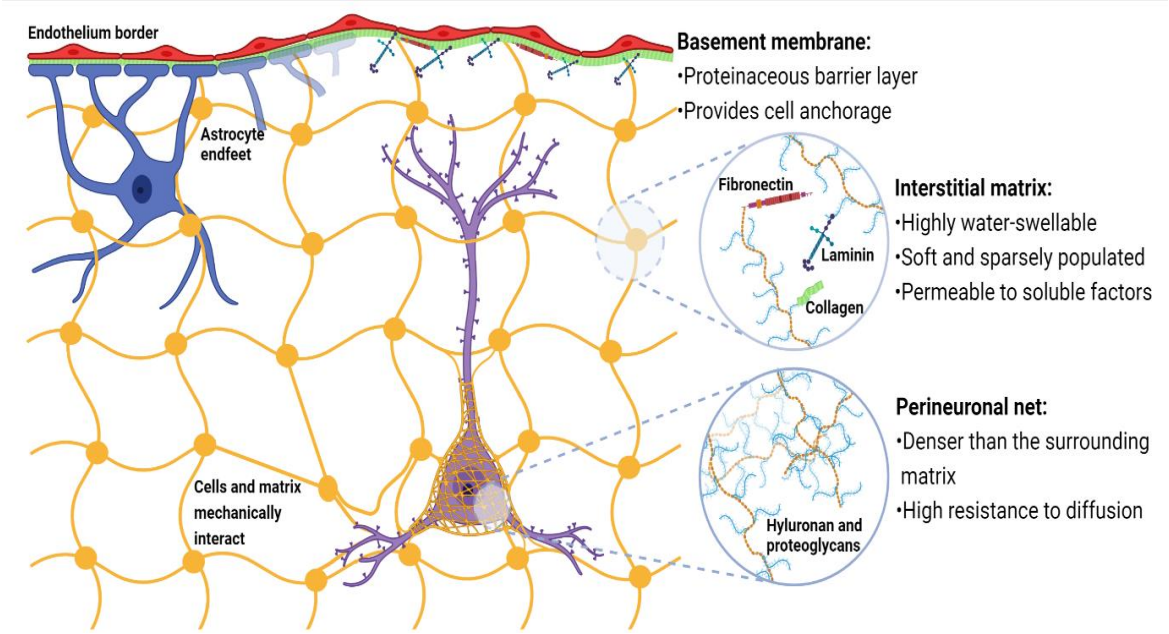

Figure 1.1: Structures and properties of neural ECM.[27] *The illustration was created with BioRender.com*

Their excessive deposition within scar tissues following neural trauma is in fact thought to be the major barrier to axonal growth, regeneration and functional recovery, which indicates a critical spatial regulatory role for CS proteoglycan deposition in tightly controlled axonal pathfinding processes.[28]

The high proteoglycan content of neural ECM imparts an exceptional water retention capability to neural tissues, which results in unique mechanical properties.[29] Neural tissues are the softest in the body with elastic modulus values as low as 0.1-1 kPa[30], opposed to 8-17 kPa

for skeletal muscle[31] and up to 3 GPa for bone.[32] Findings within the last decade showed that independently from chemical cues, cells are able to sense and respond to mechanical properties of the surrounding matrix, leading to the discovery of mechanical signaling pathways that play major roles in tissue development and functions.[33] In the nervous system, the extremely hydrated ECM provides the optimal mechanical cueing required for cell functions, as well as mechanically distinct regions and stiffness gradients in cell microenvironments, which play pivotal roles during development and regeneration.[34]

1.1.1.2 Importance of ECM

Although the ECM accounts for less volume in the brain compared to the cellular network, slight changes in its chemical, mechanical or biological properties can result in significant behavioral and morphological alterations in the cells, impacting the overall function of the neuronal network.[35] Of note, changes in ECM structure and function have been associated with neuropathologies including Alzheimer's disease,[36] traumatic brain injury,[37] and epilepsy.[38] Not surprisingly, the cellular response to synthetic/engineered ECM analogues *in vitro* is no different. As a matter of fact, while seeking biomaterial scaffolds that could act as native ECM analogues and support neuronal networks, studies have shown that minimal changes in the biomaterial's elasticity,[39] composition,[40] and topography,[41] have significant effects on cell-matrix adhesion, network electrophysiology, and long-term culture viability. Ideally, the 3D scaffolds should present cells with biomimetic entities of the ECM so that the neuronal networks mimic the *in vivo* structure-function relationships through cell-scaffold interactions. For this reason, from a material standpoint, it is crucial to replicate the ECM complexity and heterogeneity to boost the impact of *in vitro* studies. In the *in vivo* microenvironment, the ECM plays the role of providing anchorage points for neurons during maturation and growth. When attempting to culture neurons outside of the body, enhancing cell adhesion to provide those

anchorage points on engineered biomaterials is thus of critical importance.[42] For many cell types cultured *in vitro*, once seeded, whether in 2D or 3D, the cells need to adhere to a substrate/matrix within the first few hours for a viable culture. For successful cell adhesion, biomaterials are commonly functionalized with adhesive molecules derived from, or similar to those found in, the ECM such as poly-D-lysine[43] and laminin.[44]

Beyond providing a reservoir of soluble proteins such as growth factors and cytokines, recent studies have demonstrated the active role played by the ECM topographical cues in influencing several cellular responses such as adhesion, migration and differentiation. In the native nervous system, the ECM is mainly composed of glycosaminoglycans and fibrous proteins (e.g., collagen, elastin, fibronectin and laminin), assembled into a nanofibrillar network that provides structural support to the native cells.[45] To date, several biomaterials have been employed to develop electrospun scaffolds that mimic the *in vivo* fibrous morphology of ECM.[46,47] In particular, such studies highlighted the importance of several design parameters such as porosity,[48] fiber diameter[49] and orientation[50] (random or aligned) in dictating differential neuronal responses in terms of adhesion, neurite growth, morphology and network complexity.

Of primary interest in numerous studies aimed at recapitulating the ECM *in vitro* is also the influence of mechanical cues on neuronal network behavior, since neurons are known to be mechanosensitive.[51,52] Of these mechanical properties, the stiffness of a substrate has been shown to influence neuronal networks significantly.[39,51,53] Due to the high concentration of glycosaminoglycans, proteoglycans, and glycoproteins in neural ECM and its lack of fibrillary proteins, such as collagen and fibronectin, the elastic modulus of brain tissue is significantly lower than other tissues. For instance, the elastic modulus of white matter (outer layer consisting of cell bodies, dendrites, unmyelinated axons, and ECM) and grey matter (consisting

of primarily myelinated axons and ECM) ranges between 1-2 kPa[54] and from ~90-230 kPa in the spinal cord.[55]

1.1.2 Topographical cues

Since 1945, the contact guidance term has been used to emphasize that topographical features of the biomaterial surface can control biochemical and biophysical signaling pathways. Furthermore, there are several developmental instances in which neuronal cells migrate along tracts of glial cells or oriented extracellular matrix (ECM) fibers. For example, during the histogenesis of the cerebral cortex, cortical neurons are guided along radial glial cells. The migrating neurons wrap around the radial glia, which acts as both the scaffold and the source of new neurons.[56] Contact guidance also plays a role in the response to injury in both the peripheral and central nervous systems. Following a nerve transection in the peripheral nervous system, the myelin sheath undergoes longitudinal segmentation. SCs proliferate, forming a Büngner band, in addition to producing growth factors in response to denervation, cleaning up the debris of Wallerian degeneration, and laying down tracks which will then retract when reinnervation occurs.[57]

While most of the published studies discuss the ability of microtopography to direct cell orientation and neurite outgrowth, the effects are not limited to just morphological changes. Increasing evidence has shown that surface topography can trigger cellular responses and pathways that affect cell adhesion, polarity and differentiation.[58] For instance, it was reported that vinculin, a major cytoskeletal protein associates with focal adhesion sites, was increased in C6 glioma-astrocytoma rat cell line cultured on nano-dot substrates, resulting in induced FA plaques.[59]

Additionally, micropillars were shown to greatly affect the neuronal polarity (i.e., formation of axons and dendrites) as they upregulated N-cadherin and Golgi-centrosome complexes,

greatly implicated in the initial neurite formation area.[60] Different topographical patterns were shown to induce a different cell lineage, astrocytes or neurons. Linear micro-pattern and circular micro-pattern substrates with two different feature sizes (2 or 10 μm in width and spacing and 4 μm in depth) were reported to significantly enhance the differentiation of adult human neural stem cells (ANSCs) to neurons while depressing differentiation to astrocytes compared to control.[61]

Probably the most used continuous topography reported in the literature are anisotropic microgrooves and aligned nanofibers. Regarding the former, several studies have shown the critical role in designing proper geometrical features such as the widths and depths of the grooves.[62–64] For instance, when the range of groove size is a few mm to tens of mm, embryonic hippocampal neurons show a tendency to grow in parallel to the groove as the depth increases. Interestingly, the polarity of embryonic hippocampal neurons also adapts to changes in topography. Monopolar and bipolar cells grow into multipolar cells when the space between grooves becomes significantly larger than the size of neural cells.[65] In another study, mouse hippocampal nerve progenitor cell (mNPCs) elongation, alignment, and neuronal differentiation improved in response to the increase of the micro-grating depth (**Figure 1.2**).[66] Researchers have also started to investigate the effects of micro- and nano-topography on the expression of pivotal proteins involved in the integrin-mediated mechanotransduction. For instance, a recent study has unveiled the correlation between vinculin and FAK expression and the groove dimensions.[67] Results from this study clearly showed that specific groove patterns were able to greatly influence the expression and organization of representative focal adhesion assembly and mechanosensitive proteins. Surfaces with 300 nm ridges, 600 nm grooves, and 300 nm-diameter pillars displayed the greatest level of vinculin and FAK expression in human neural stem cells (hNSCs). Such patterns were also shown to efficiently induce the differentiation of hNSCs into neuronal and astrocyte lineages. In another study, it was shown

that hierarchically patterned substrates, consisting of microgrooves decorated with nanotubes, can synergistically enhance the differentiation of hNSCs, facilitate the alignment of the cytoskeleton and the formation of focal adhesions.[68]

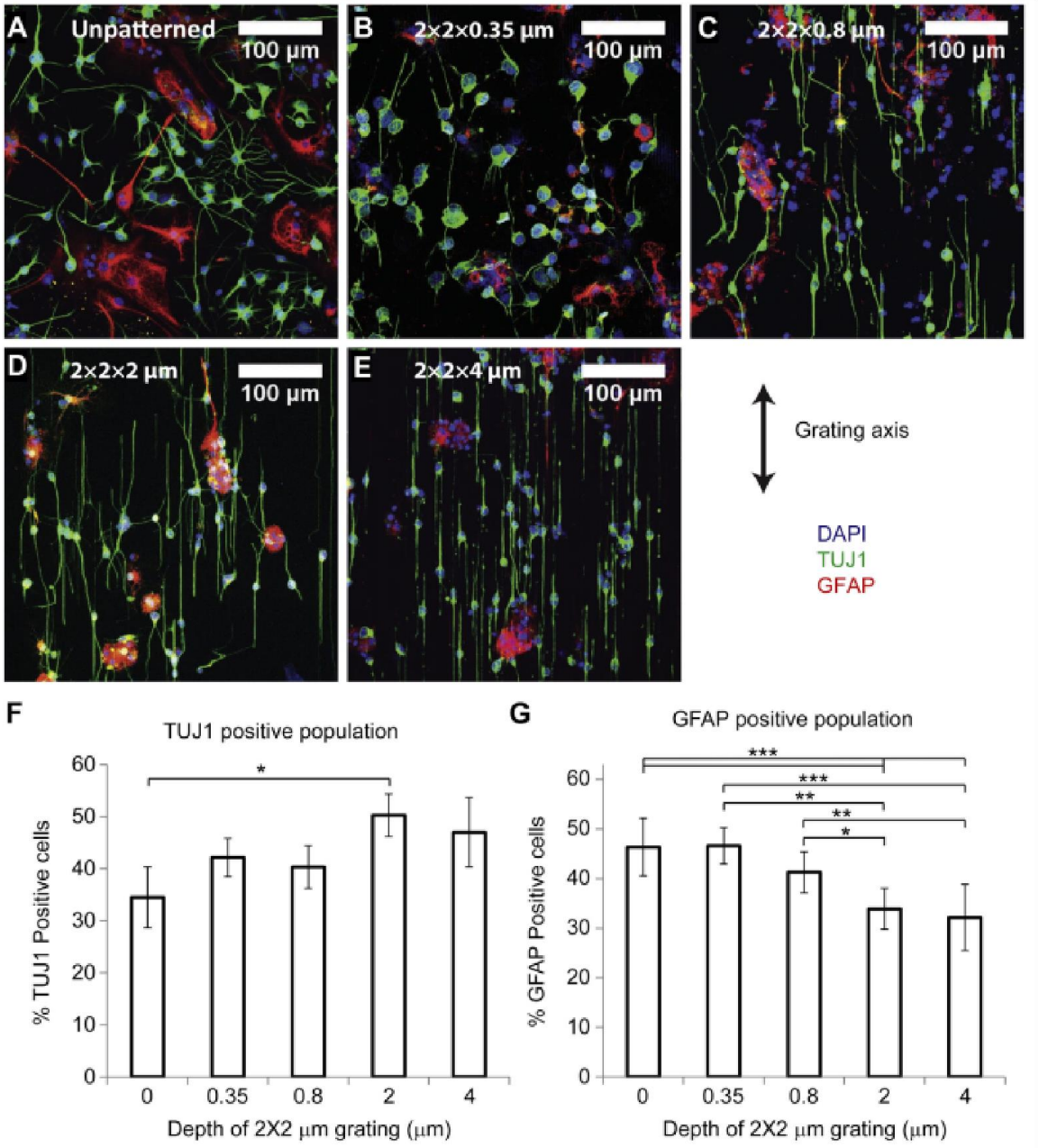

Figure 1.2: Neuronal differentiation of hippocampal mNPCs after 2 weeks on either unpatterned or micro-patterned PDMS. (A) unpatterned PDMS and PDMS gratings of dimensions (B) 2 x 2 x 0.35 mm (C) 2 x 2 x 0.8 m (D) 2 x 2 x 2 mm and (E) 2 x 2 x 4 mm; Percentage of TUJ1 (F) and GFAP (G) positive population on the different substrates; Significant difference is indicated by *** where $p < 0.005$, **where $p < 0.01$, and * where $p < 0.05$. [66] *Copyright © 2014 Elsevier Ltd.*

Results also demonstrated the importance of β_1 integrin-mediated binding and the intracellular Rho-associated protein kinase (ROCK) pathway in guiding neuronal differentiation. Treatment of the substrates with either an antibody against β1 integrin or Y27632, a ROCK inhibitor, significantly decreased neurite alignment and trumped the neurogenic differentiation of hNSCs, proving the fundamental role played by such proteins in guiding neuronal behavior.

Electrospun nanofibers have been probably the most extensively explored as a class of scaffolding materials for tissue regeneration, because of their unique capability to mimic some features and functions of the extracellular matrix, including the fibrous morphology and mechanical properties, and to a certain extent the chemical/biological cues. Thanks to the progress in fabrication techniques, researchers have been able to fine-tune the diameter, the orientation and the chemical make-up (i.e., biomolecule functionalization) of the nanofibers by which it is possible to elicit preferential neuronal and stem cell responses. For example, many groups have compared the effects of aligned and random fibers on neurite orientation, and some have used aligned fibers as a driving force for neuronal differentiation.[69,70] Generally neural cells grow in parallel with aligned or anisotropic nanofibers showing a preferential orientation when compared to random fiber structures. ANSCs cultured on aligned fibers elongated along the major fiber axis. Upon induction of differentiation with retinoic acid, a higher fraction of cells on aligned fibers exhibited markers of neuronal differentiation (MAP2 and Tuj1) as compared with cells on random fibers or un-patterned surfaces.[71] In another study, spinal cord-derived neural progenitor cells (NPCs) seeded on electrospun aligned collagen nanofibrous showed a faster neurite expansion and a higher proliferation when compared to randomly oriented fibers.[72] Furthermore, the authors revealed that the integrin binding to aligned collagen preferentially activates MAPK signaling cascades that lead cells to exit the G0/G1 phase cycle faster than randomly distributed fibers. Beyond directionality, other parameters such as the diameter or the density of fibers also influenced the guidance of neural cell growth.[73,74] When

testing poly-L-lactic acid (PLLA) fibers with diameters in the range of 300 nm to 1300 nm, larger diameter fibers promoted a longer, more directed neurite growth and increased SC migration distance. Functionalizing aligned fibers can also affect the time required for differentiation. Pluripotency markers decreased after only 1 day of culture on aligned YIGSR-tethered PCL fibers, followed closely by increased neural differentiation markers of Tuj1 and MAP2 by day 3. Controls contained fibers that were aligned, with no peptide, or randomly arranged with YIGSR.

1.1.3 Mechanical cues

Over the past decade, it has been established that cells are sensitive not only to the environmental topography but also to the mechanical properties of their surroundings. The environmental mechanical characteristics are in fact implicated in development but can also provide a unique signature of pathological conditions.[75] Years of research have focused on the mechanical properties of biomaterials influencing specific cellular behavior and function *in vitro*.[76–78] Accordingly, the manufacture and design of biomaterials have been expected to contribute to optimal tissue repair and development, based upon the activation of biomaterial mechanical stimulation. Several mechanical properties, including stress/strain, elasticity/stiffness, and certain time-dependent mechanical properties (e.g., viscoelasticity and stress relaxation, creep and strain recovery) have been shown to activate specific signaling pathways that govern fundamental cellular functions (**Table 1.1**).

It is now widely accepted that cells (from stem cells to mature cells) can sense and respond to substrate stiffness by three steps: mechanosensation, mechanotransduction, and downstream mechanoresponses.[79] Briefly, when cells first contact the substrate surface, large protein complexes called focal adhesions (FAs) are formed to tether the cell cytoskeleton to the substrate. Then the physical signals of the microenvironment are sensed and transduced into

biochemical signals, activating subsequent changes in cell behaviors, including cell morphology, growth, differentiation, and death.[80] Increasing evidence is pointing at the matrix's stiffness (either native ECM or engineered substrates) as the major mechanical characteristic affecting cellular decisions and tissue development via tissue engineering approaches. It is now well accepted that soft materials, close to that of neural tissue or <1 kPa elastic modulus, encourage neuron viability and neurite extension.[81] For example, cortical neurons extended longer neurites on 0.6 kPa elastic modulus, laminin-coated acrylamide gels, while astrocytes were rounded and had disrupted actin fibers on the same scaffolds. In contrast, neurite extension was strongly decreased on 27 kPa gels.[82] In a similar study, the effects of varying stiffness and protein coating on hippocampal neuron extension were explored focusing in particular on actin filament formation, FAK, growth cone formation, and neurite outgrowth through the ERK1/2 pathway.[83] Hippocampal neurons had the greatest neurite extension on 88 kPa elastic modulus fibronectin-coated polydimethylsiloxane (PDMS), which correlated to increased FAK and ERK1/2 phosphorylation compared to poly-L-lysine coated surfaces. The investigation of surface stiffness effects was also conducted on neural stem cells. For instance, embryonic NSCs were shown to differentiate into neurons and astrocytes on PDMS of a wide range of elastic moduli, but softer scaffolds promoted neuronal maturation and increased neurite outgrowth.[84] Specifically, scaffolds with stiffness ranging from 0.1 to 0.5 kPa favoured neuronal differentiation of NSCs, while more astrocytes formed on 1-10 kPa gels. Although the absolute range of scaffold stiffness between studies varies, an overall trend emerges where neurons prefer soft environments with similar stiffness to brain tissue (<1 kPa) and glia prefer stiffer environments (>5 kPa).

While it has been established that substrate stiffness can be exploited as a driving force to direct basic cellular functions including neurite outgrowth and neurogenic differentiation, it is pivotal to understand what are the key players that intervene and guide the

mechanotransduction signaling process. In this context, a recent study has highlighted the correlation between cell contractility (cytoskeleton shape) and NSC neuronal differentiation on 0.1-75 kPa laminin-coated PDMS surfaces.[94]

Table 1.1: Influence of biomaterial mechanical properties on cellular signaling pathways.

Mechanical property	***Pathway/cell effects***
Stress/strain	Affecting cell phenotypic change and functions.[85] Increasing mesenchymal stem cells (MSCs) differentiation in terms of ALP activity.[86] Activating the TGFβ pathway and the MEK/Erk1/2 pathway in VICs.[87]
Elasticity/Stiffness	Influencing the phenotype and functionalization of terminal cell types.[88] Inducing the differentiation of MSCs into various cell end points.[89] Activation of β-catenin transduction and integrin/FAK pathway in ASCs.[90]
Creep/strain recovery	Inducing increased cell spreading and cell traction in different cell lineage.[91] Enhanced human MSCs differentiation towards several lineages.[92] Mediated by a change in cytoskeletal tension in hMSCs.[93]

It was determined that the specific activation of Rho GTPase regulated both the *in vitro* and *in vivo* cell fate by promoting neuronal differentiation over astrocytes or oligodendrocytes. Lately,

the Hippo signaling pathway has garnered significant interest due to mounting evidence highlighting its pivotal role in mechanotransduction.[95,96] A key effector of this pathway is YAP, a transcriptional co-activator. The nuclear translocation and consequent transcriptional activity of YAP are intricately governed by biophysical cues, such as substrate rigidity,[97] cytoskeletal tension,[98] and alterations in cell morphology.[99,100]

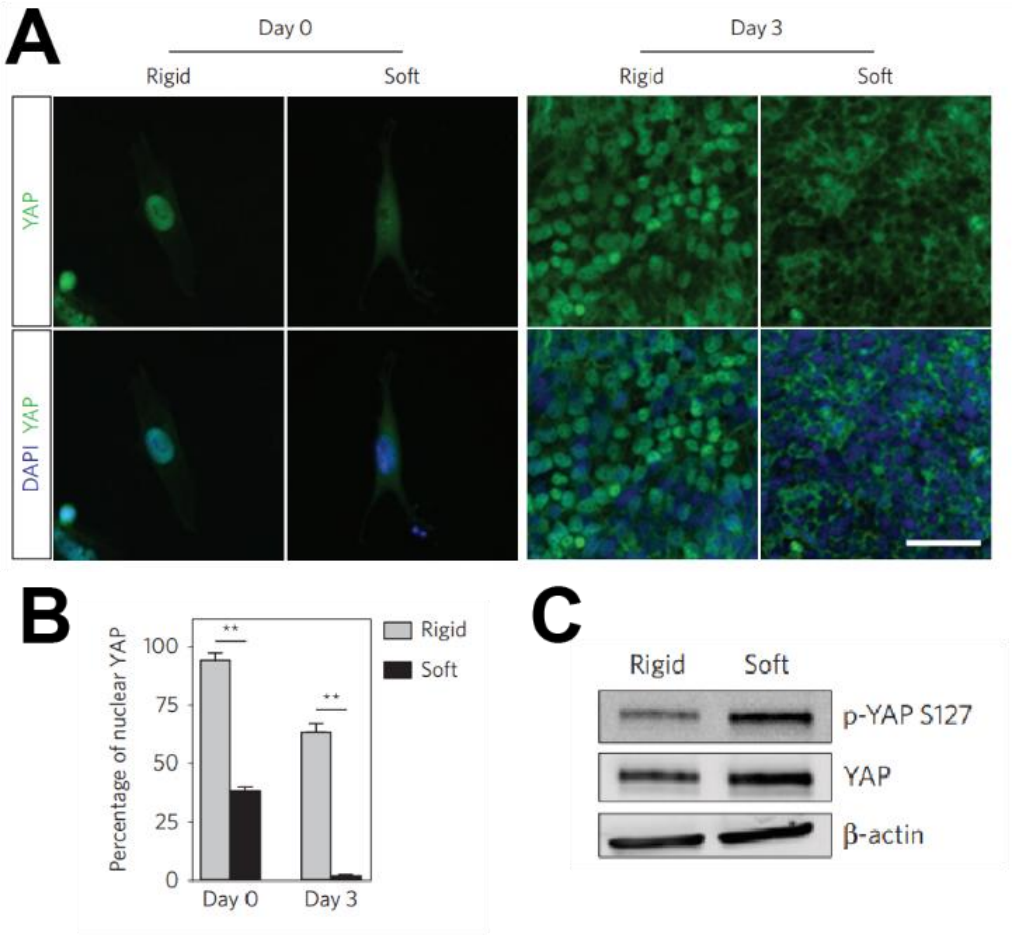

Figure 1.3: YAP and phosphorylated YAP expression on soft and rigid PMA substrates. (A) Representative immunofluorescence images of hESCs expression of YA when seeded onto rigid (left) and soft (right) PMA substrates at DIV0 and 3. (B) Percentage of nuclear YAP for rigid and soft substrates at DIV0 and 3. (C) Western blotting for phosphorylated YAP S127 (p-YAP S127) and YAP in whole cell lysates of hESCs after 3 days of culture on rigid and soft PMAs.[101] *Reproduced with permission from Springer Nature*.

In a recently published study, the influence of substrate's stiffness in influencing the activation of the Hippo pathway and the subsequent impact on the neurogenic differentiation of human embryonic stem cells (hESCs) was greatly investigated.[101] Specifically, it was shown that soft

poly(dimethylsiloxane) micropost array (PMAs) promoted YAP1 phosphorylation on Serine 127 that resulted in loss of hESCs pluripotency and neuroectoderm differentiation (**Figure 1.3**). Such findings were corroborated by the evidence arising from the silencing of LATS1, a downstream Hippo kinase that targets serine 127. Notably, LATS1 knockdown hESCs exhibited a spread morphology on both rigid and soft PMAs, indicating loss of mechanosensory properties and the enhanced neurogenic differentiation seen for soft PMA was lost, further supporting that LATS-mediated phosphorylation of YAP1 plays a pivotal role in sensing mechanical signals arising from substrate rigidity.

1.1.4 Chemical cues

The main requirement for the survival of cells is the presence of a material fostering their attachment. In fact, the lack of a permissive substrate for cell adhesion would lead to cell apoptosis.[9] Cell adhesion onto materials can naturally occur through either nonspecific adsorption or adhesion molecule. For instance, chitosan and poly-lysine are examples of, respectively, natural and synthetic materials that exhibit hydrophilic- and electrostatic-based neuronal cell adhesion, where the positive charges displayed by their surfaces attract the negatively charged cell membrane resulting in electrostatic bond formation. Such unspecific cell binding however greatly limits the possibility of controlling cell behavior and dictating cellular fate. For this reason, neural tissue engineering has been mainly encompassing the use of natural ECM-derived biomaterials such as Matrigel and collagen, that can provide cultured neurons with both adhesive peptide molecules and bioactive soluble proteins/peptides such as growth factors and chemokines. Alternatively, biomaterials can be decorated with purified or chemically synthesized components of specific extracellular matrices. Molecules such as laminin, fibronectin and neural adhesion molecule L1 are known to promote cell differentiation, adhesion and migration in the CNS.[102–104] As a matter of fact, materials pre-

coated with laminin showed significant improvement in neural cell affinity and functional recovery.[105] Moreover, biomaterials coated with L1, which is highly expressed in growing axons and Schwann cells during development and regeneration, have been proposed as promising scaffolds.[106] However, pathogen transfer, batch variability and cost related to the usage of full-length protein constitute important drawbacks that are limiting their usage. An innovative method is the functionalization of biomaterial surfaces with short peptides known to stimulate cell attachment. These short peptides can be synthesized and covalently attached to both natural and synthetic materials. Specific functions of several key extracellular proteins physiologically comprising the tissue microenvironments have been attributed to short peptide sequences. In the case of laminin, the best characterized and used sequences are YIGSR, IKVAV and RGD. [104] Specifically, it has been shown that RGD-functionalized PHPMA hydrogels and RGD-functionalized PEG polymers are capable of promoting neural tissue repair and enhancing cell adhesion, respectively.[105,107,108] Also, RGD-containing HA scaffolds as well as fibrin gels modified with laminin were shown to increase neuronal cells proliferation.[109] Peptide sequences that incorporate both YIGSR and IKVAV have been found to significantly increase neuronal adhesion. Moreover, various electrospun nanofibrous tubes made of either natural, synthetic or biosynthetic materials and functionalized with bioactive molecules, have demonstrated to be able to support the survival, proliferation and differentiation of neural cells. [110] For instance, the incorporation of the IKVAV sequence in PA nanofiber gels has been shown to enhance the differentiation of neural progenitor cells (NPCs). Finally, it is important to underline that cell attachment to materials is related not only to the choice of ligand for the functionalization but also to ligand density and exposure. Indeed, by using modular biomimetic interpenetrating network hydrogels, NSC differentiation on substrates with varied functional motif and mixed functional motif densities has been demonstrated to be sensitive to a minimum RGD density.[111,112] Many ongoing studies aim at optimizing the biomaterial choice,

discovering new cell-adhesive peptide sequences, identifying the best cell-adhesive functional motifs and selecting the proper functional motif concentrations.

1.2 Recent *in vitro* trends for neural tissue engineering applications

Advances in tissue engineering and cell biology greatly rely on cell-based *in vitro* assays and models that facilitate the investigation and understanding of specific biological events and processes under different conditions. The quality of such experimental models and particularly the level at which they represent cell behavior in the native tissue, is of critical importance for our understanding of cell interactions within tissues and organs.[113] Conventionally, *in vitro* models are based on experimental manipulation of mammalian cells, grown as monolayers on flat, two-dimensional (2D) substrates. Despite the amazing progress and discoveries achieved with flat biology models, our ability to translate biological insights has been limited, since the 2D environment does not reflect the physiological behavior of cells in real tissues.[114] TE has seen continuous evolution in the past two decades. It has also been assimilating of knowledge and technical advancements from related fields such as material science, rapid prototyping, nanotechnology, cell biology, and developmental biology. Specific advancements that have benefited TE as a field in recent years include novel technologies, integration of nanotechnology, stem cell technologies such as induced pluripotent stem cells (iPSCs), and gene editing technology such as Clustered Regularly Interspaced Short Palindromic Repeats (CRISPR). Specifically, advances in 3D cell biology and biomaterial science have led to the development of a new generation of cell culture formats that can better recapitulate the *in vivo* microenvironment, allowing us to examine cells and their interactions in a more biomimetic context.[115] Modern biomedical research can rely on novel technological approaches that promote the development of more sophisticated and robust tissue engineering *in vitro* models, including scaffold- or hydrogel-based formats, organotypic cultures, and organs-on-chips.

Even though such systems are necessarily simplified to capture a particular range of physiology, their ability to model specific processes of human biology is greatly valued for their potential to close the gap between conventional animal studies and human (patho-) physiology.

1.2.1 Limitations of traditional in vitro assays

Cell culture systems represent an indispensable tool for a wide range of biomedical studies. Over the years, cell culture has evolved into a useful and vital tool for a wide variety of applications including drug development, cancer research, and tissue engineering.[116,117] For all these applications, two-dimensional (2D) cell culture systems dominate, continuing to improve our perception and understanding of cell biology. These cell systems rely mainly on adherent cultures, where cells grow as a monolayer attached to a plastic or glass substrate. Although easy and convenient, 2D cultures exhibit numerous disadvantages. Firstly, they are simplistic imitations of the *in vivo* situation, where cells grow within a complex three-dimensional (3D) microenvironment **(Figure 1.4**).

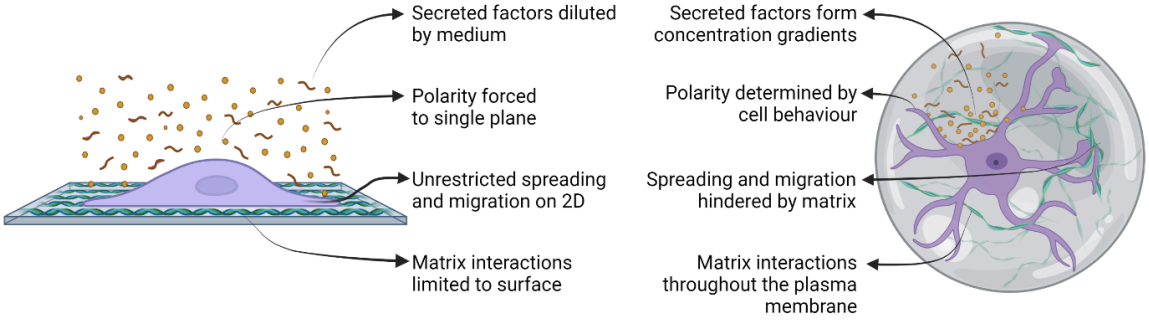

Figure 1.4: 2D vs. 3D cell culture. Comparison between cell cultures on a 2D substrate (left) and a 3D matrix/scaffold (right), outlining some of the important physiological features that cue cellular behavior.[27] *The illustration was created with BioRender.com*

This lack of environmental context and structural architecture limits the ability of cells to communicate with one another and with the surrounding matrix, which is critical for various cellular processes (e.g., mitosis, self-renewal, and differentiation).[117,118]

Such physical constraints also impede cells from organizing naturally and spreading vertically, forcing them to flatten out and grow as monolayers.[122] Gene expression, protein production, and cytoskeletal structure are also altered, leading to loss of cell phenotype and consequent physiological dysfunction.[119] Furthermore, in monolayer cultures with no oxygen or nutrient gradients, cells are unable to respond to physiological stimulation, inhibiting basic cellular processes.

Ultimately, these inherent limitations and flaws in 2D cell systems result in failures to understand healthy or diseased cell behavior.[120] The research community is now beginning to seek alternative technologies that could facilitate development of models able to more closely mimic the complexity of whole tissues *in vitro*. To this end, 3D cell cultures can provide a well-controlled *in vivo*-like microenvironment specifically tailored to each application.

1.2.2 Scaffold-based 3D cultures

Developing biomaterials for CNS modeling is complicated by the unusual mechanics of soft tissues; the brain is neither liquid nor a solid, but rather possesses viscoelastic properties similar to those of highly hydrated tissues containing heterogeneous polymer networks. Heterogeneity of structure and composition, together with hierarchical patterning, determine cellular processes and nonlinear dynamic mechanical behavior that cannot be captured by simplistic plastic 2D vessels. In this context, hydrogels seem to be ideal biomaterials for CNS modelling due to their high water content and porous structure enabling diffusion of metabolites, with the solid-phase polymer network providing relevant mechanical and spatial cues, tunable mechanics and versatile chemical modification.[121] Hydrogels are hydrated 3D networks of crosslinked hydrophilic polymer chains that can retain a large amount of water (over 90%) while maintaining solid form. They are the most common type of biomaterial used to support bioengineered 3D neural cultures as their physical and chemical properties can be tuned to

mimic the native neural ECM.[122] While designing hydrogels for neural tissue engineering is important to consider several properties and characteristics. For instance, polymerization, or gelation, is the transitioning process from a liquid to a solid state. The hydrogel polymerization mechanism strongly determines its suitability for the different biomedical applications. Similarly, the hydrogel rate of degradation can also quite determine how the hydrogel is used therapeutically. For example, a fast-degrading hydrogel could be used for the quick delivery of an immunosuppressive drug to brain tissue for immediate action against the inflammatory response, while a slowly degrading hydrogel could protect encapsulated cells from this same initial inflammatory insult and could provide a longer-lasting physical scaffold for rebuilding tissue. A major benefit of using hydrogels is the ability to incorporate many different types of molecules and to encapsulate in 3D a variety of different cell types. The performance of a hydrogel in brain tissue and the release of cells or therapeutics from the hydrogel depends on the mechanical and chemical properties of the hydrogel and how it is defined during polymerization and degradation. Finally, biocompatibility, specifically within the brain, is an especially important consideration, as the brain is a partially immune-privileged site reacting independently of the peripheral immune system. The structural component of a hydrogel is composed of a dense collection of hydrated intermeshed polymer chains that form a swollen matrix within an aqueous medium. The properties of this matrix are extensively customizable using chemical and physical crosslinking techniques. The simplest form of chemical crosslinking encompasses the use of crosslinking molecules such as genipin or N-(3-Dimethylaminopropyl)-N′-ethyl-carbodiimide hydrochloride (EDC) to conjugate the polymers chains. [123] Such a technique is often used to bind biofunctional molecules into the hydrogels to provide additional chemical cues to direct neuronal behavior. Another type of chemical crosslinking encompasses the introduction of photosensitive functional groups in the hydrogel and the use of a specific wavelength of light to start the polymerization.[124] A third alternative

is represented by enzymatic crosslinking and uses enzymes such as transglutaminase and peroxidase to develop fast-gelling, stable and non-toxic hydrogels.[125] In addition to chemical cross-linking, another class of hydrogels can be formed by the physical association of components, often by hydrogen bonding at the molecular level.[126,127] While there are various crosslinking methods for hydrogel synthesis, the choice of crosslinking strategy is often chosen based on the chemistry of the raw material and specific application. In general, physically crosslinked hydrogels preserve cell viability better. However, the mechanical properties of physically cross-linked hydrogels tend to be weak, increasing the likelihood of matrix degradation in longer term cultures. Hydrogels modified through chemical crosslinking can provide a more stable substrate, supporting longer culture periods.

Beyond the polymerization process, hydrogels are usually classified as either natural or synthetic. The use of synthetic polymers in neural tissue engineering is advantageous because of their mechanical strength and flexibility combined with ease of modification (i.e., blending and copolymerization).[128] Synthetic polymers are also compatible with numerous fabrication techniques, such as wet-spinning, freeze-drying, and electrospinning.[129,130] The most commonly used synthetic scaffolds in neural tissue engineering are methacrylate(pHEMA) and polyethylene glycol (PEG) hydrogels, which when functionalized with adhesive motifs have displayed great compatibility with neuronal cell lines.[130–133]For instance, a study has reported that a pHEMA hydrogels photo-crosslinked with nerve growth factor (NGF) has comparable outcomes in terms of PC12 viability and neurite outgrowth to collagen hydrogel.[131] However, there are inherent problems with the use of synthetic polymers. Despite synthetic polymers being mainly non-toxic, there are still concerns regarding toxic residual monomers from incomplete polymerization as well as degradation products.[134] For this reason, the clinical translation of synthetic polymers has been greatly hampered.

In the context of neural tissue engineering, the use of natural polymers is highly beneficial due to their high biocompatibility and natural biodegradation kinetics combined with chemically tunable properties.[121,122,128] Often, natural polymers are analogues, if not identical like in the case of collagen, to substances already present in the human body, minimizing the risks of cytotoxicity and immunogenic reaction upon implantation in the body. The main two categories of natural polymers are polysaccharides (chitosan, alginate, hyaluronic acid) and proteins (Matrigel, collagen type I and IV, gelatin). The intrinsic properties of natural polymers create a cell-friendly environment that promotes, either directly or after targeted physicochemical modifications, relevant cell responses such as adhesion and proliferation, making this class of materials the "gold standard" for applications in neural tissue engineering and regenerative medicine.

1.2.2.1 Collagen type I hydrogels in neural tissue engineering

Among the various natural polymer, collagen surely represents one of the most promising candidates for neural tissue engineering. Such consideration is also validated by the fact that collagen is the only biopolymer approved for clinical testing in neural tissue engineering and several collagen-based products are now commercially available.[6,135–137] Collagen is the most abundant protein found in the human body. The presence of collagen in all connective tissue makes it one of the most studied biomolecules of the ECM. This fibrous protein species is the major component of skin and bone and represents approximately 25% of the total dry weight of mammals.[6] Collagen can be extracted from various sources considering that it is one of the most abundant proteins on earth. Common sources of collagen for tissue engineering applications include bovine skin and tendons, porcine skin and rat tail among others.[135] Among this protein family, collagen type I has gained great attention in the context of tissue engineering because of its well-documented role in maintaining the biological and structural

integrity of ECM and providing physical support to tissues. In addition, collagen type I offers low immunogenicity, a porous structure, permeability, good biocompatibility and biodegradability and thanks to its bioactive peptide motifs it can regulate the morphology, adhesion, migration and differentiation of cells.[136] All these good performances make this natural polymer seem to be a promising biomaterial for scaffolds in tissue engineering. From a structural point of view, collagen type I is made up of three alpha chains (two α1 and one α2). Each collagen chain is made up of approximately 1000 amino acids following a Gly-X-Y repeating sequence, with X and Y being usually proline and hydroxyproline, respectively.[137] The free functional groups of collagens (amines and carboxyl) can be used to modify their structure and be used to create physical or chemical cross-links. The ability of collagen to form intra- and interfibrillar cross-links can be exploited to create hydrogels with a range of mechanical properties to match the ones showcased by the surrounding tissue when implanted. The unique fibrillar architecture of collagen I can be also used to create anisotropic hydrogels that are suitable for contact guidance applications and tissue engineering.[138,139] Collagen fibrils can be aligned using a variety of external stimuli. For instance, the application of uniaxial tensile force during fibrillogenesis has been shown to create highly anisotropic constructs.[138] In addition, the application of external magnetic fields in the presence of magnetic nanoparticles in the collagen solution has displays outstanding results in preferentially aligning the fibers.[139] Collagen type I is a highly versatile material and can be used as a coating material for existing implants, as a hydrogel or it can be freeze-dried to form 3D porous scaffolds or thin films. However, the collagen type I extracted and purified from natural sources is susceptible to low structural stability and, when uses alone, it lacks the desired mechanical strength.[6,135–137] To address such issues, collagen is usually crosslinked or used in combination with other biomaterials to increase the mechanical strength and preserve the scaffold ultrastructure for an extended period by reducing enzymatic degradation *in vivo*.[140] Physical

crosslinking of collagen includes ultraviolet (UV) irradiation and de-hydrothermal (DHT) treatment, while chemical crosslinking encompasses the use of crosslinker molecules such as glutaraldehyde (GTA), EDC and genipin.[6,135,137,140] As mentioned above, collagen type I has been the preferred material to create Nerve Guide Conduits that are suitable for peripheral nerve regeneration and sciatic nerve repair.[141] For the former, most of the FDA-approved commercially available NGCs are made up of collagen. The commercial collagen matrices are in the form of conduit or wrap and serve as a guide for axon regeneration across the nerve gap and help to align the regenerating axons. Also, they function as a barrier to prevent scar formation, while allowing nutrient exchange and neurotrophic factors across the matrix.

Beyond being used to engineer tissue substitutes for the regeneration and repair of damaged tissue, collagen has been incorporated in several biomaterials-based scaffolds that have found application in 3D *in vitro* modelling and drug screening systems. In a recent study, collagen was mechanically aligned through anisotropic strain during fibrillogenesis and used to reconstruct the hippocampal CA31-CA1 circuit.[142] The ordered structural organization of aligned collagen was shown to not only introduce a physical cue that optimally directs neurite growth and orientation but also to enhance the functional connectivity of the two neuronal populations. In addition to the several advantages mentioned before, the mechanical properties of collagen can be easily modulated varying its concentration or the amount of crosslinking agent. For instance, it has been shown that varying the relative concentration of collagen and N-hydroxysuccinimide (NHS) can produce a panoply of hydrogels characterized by stiffness that ranges from 0.15 to 1.5 KPa, which greatly matches the mechanical properties of native tissue.[143] Collagen has also demonstrated the ability to create a supportive scaffold with controllable porosity, which it is a fundamental requirement that must be met when developing 3D *in vitro* models. In a recent study, collagen-based hydrogels characterized by different porosity were employed to investigate the effect of β-amyloid (Aβ) deposits, which are

associated with Alzheimer's disease (AD), on differentiating neurons.[144] The aggregates did not influence cell viability on construct with small size pores (approximately 0.2 μm). On the other hand, when the Aβ aggregates diffusion was permitted by the larger pores (1-1.2 μm), massive neuronal death was observed. In another interesting study, collagen hydrogels were employed to model the blood-brain barrier (BBB) dysfunctions in AD. The model was able to successfully recapitulate key aspects of BBB in AD condition, such as increased BBB permeability, increased expression of oxygen reactive species and enhanced deposition of Aβ peptides at the vascular endothelium. As mentioned above, the most reported drawback of collagen is the high degradation rate in physiological condition that greatly depend on its pronounced swelling behavior. For this reason, when employed in long-term modelling platforms, collagen is usually chemically crosslinked or used in combination with other polymers. In a recent study, a collagen/silk-fibroin fibers platform was employed to characterize the long-term activity of AD patient-derived iPSCs.[145] Interestingly, after 10 weeks of culture both spontaneous and inducible activity were observed, indicating the presence of healthy and functioning neurons in the construct.

1.2.3 Nanoparticles in neural tissue engineering

Among the possible functionalization strategies inspected in neural tissue engineering, nanoparticle motifs certainly represent the most promising one. The emergent field of nanomedicine proposes the application of precisely engineered nanomaterials for the prevention, diagnosis, and therapy of certain diseases, including neurological pathologies.[146–148] Although still narrow, the application of nanotechnology and nanomaterials to neural tissue engineering has experienced an impressive growth over the past decades, with an increasing number of studies proposing scaffolds decorated with nanoparticles to modulate cell behavior.[149] Nanoparticles are materials with a basic structural unit that has at least one dimension

smaller than 100 nm in length. Due to their small size, nanoparticles can interact with and affect cells and tissues at the molecular level.[147] The use of nanomaterials in the design of tissue scaffolds in the nervous system is primarily due to their abilities to favor neuronal adhesion, to re-create an ECM-like microenvironment and to interact with neuronal membranes at the nanoscale.[146–149] In fact, a fundamental step, in any strategies aimed at improving the nervous system's regenerative ability, is the manufacturing of scaffolds which are able to control (and to selectively tune) cellular adhesion, to govern axonal regrowth, neuronal physiology and guide neural stem cells differentiation.[146–148] Additionally, nanoparticle-based approaches have the potential to overcome the blood-brain barrier (BBB), which prevents various therapeutic drugs from penetrating into the brain and therefore limiting the treatment of many neurodegenerative disorders.[146–148,150] Therefore, nanoengineered delivery systems potentially facilitate the targeted delivery of neuronal therapeutic drugs and genes to the central nervous system. Furthermore, newly developed nanocomposite biomaterials are considered therapeutic agents themselves since they exhibit important roles in promoting the protection of healthy neurons or the regeneration of neurons to repair damaged tissues.[151] Nanoparticles have different characteristics, i.e., the material they are made of, their size, shape, electric charge, magnetic and optical properties. Importantly, nanoparticles can be modified by conjugation of reactive functional groups and bioactive molecules. These characteristics determine the nature of the interactions between the nanoparticles and cells, such as the ability of nanoparticles to bind or penetrate cells, or to affect biochemical reactions.[146–148,152,153] Owing to the electro-active properties of the native nervous system, conductive nanoparticles have emerged as pivotal tools to study the influence of introducing electro-active motifs that can regulate neuronal cell functions.[154,155] Conductive nanoparticles, often composed of materials like gold, silver, or carbon-based derivatives, possess inherent electrical conductivity that can be exploited to create electroactive biomaterial platforms.[150,152,154,156–160] When integrated into

neural scaffolds or matrices, these nanoparticles can facilitate electrical stimulation, a critical cue for neuronal growth, synaptogenesis, and electrophysiological maturation. This ability to recapitulate the native electrical microenvironment not only augments cellular interactions at the nanoscale but also ensures the translation of external electrical cues to the cellular membrane, thus emulating endogenous bioelectrical signals. The incorporation of conductive nanoparticles into neural engineering constructs, therefore, stands as a promising strategy to enhance tissue regeneration and functionality by harnessing the indispensable role of electrical signaling in neuronal communication and function. Among the various metallic nanoparticles, gold and silver nanoparticles surely represent the most promising candidates for neural tissue engineering because of their versatility and outstanding anti-bacterial properties.[150,153,158–161] Their surface characteristics also enable the conjugation with biomolecules facilitating targeted delivery of several growth factors (i.e., nerve growth factor)[150] and genes (DNA and RNA).[146,152,159] In the context of neural tissue engineering, nano-constructs could be utilized in two different ways. They could be used as suspensions, or they could be immobilized on 2D or 3D substrates that can change the properties of nanomaterials. Regarding their use in suspension, there is a controversy regarding the possible toxicity associated with the sizes and shapes of the nanoparticles.[153] For this reason, neural tissue engineering approaches usually encompass the use of nanoparticles as decorative elements immobilized on a scaffold. In fact, immobilizing these nanoparticles on different substrates can significantly reduce their toxicity and provide subcellular chemical cues that could be beneficial for the manipulation of neuronal behavior and nerve regeneration.[158] For instance, a recent study investigated the effect of coating gold and silver nanoparticles on culture surfaces for PC12 and SHSY5Y viability, differentiation and neurite outgrowth.[160] Both nanoparticles coated substrate were found highly supported for both PC12 and SHSY5Y cells, and enhanced PC12 differentiation with improved morphological parameters of neurite network such as neurite length and branching number. In

another study, gold nanoparticles were incorporated into a gelatin fibrous scaffold to study the effects on neuronal differentiation and maturation.[156] Results clearly demonstrated that the nanocomposite scaffold encouraged longer outgrowth of the neurites from both primary and PC12 cells. Despite their several advantages, metallic NPs have been shown to elicit long-term neurotoxicity both *in vitro* and *in vivo*.[162,163] Induced oxidative stress and free radical generation are the primary mechanisms of neurotoxicity, which damage cells (proteins, lipids, nucleic acids). Oxidative damage to DNA is dangerous due to its nature and mediation of mutation in cancer formation. More and more studies are being conducted that support the claim that metallic NPs contribute to neurodegenerative diseases even though they have not yet been directly linked to the etiology of any of these diseases. Because of the growing awareness of toxicity elicited by metallic nanoparticles, other materials such as ceramic, polymeric and carbon-based have been used to synthesize nanostructures that could offer better biocompatibility. Specifically, carbon nanodots are a newly synthesized type of carbon-based nanoparticles that encompass the main advantages of metallic nanoparticles together with outstanding biocompatibility.[152,154,157]

1.2.3.1 Carbon nanodots

Carbon nanodots (CNDs) are a relatively new type of carbon-based nanomaterial typically composed of carbon, oxygen, nitrogen and hydrogen. They have caught the interest of researchers due to their diverse physicochemical properties and advantageous characteristics such as good biocompatibility, low cost, eco-friendliness, abundant functional groups (e.g., amino, hydroxyl, carboxyl), high stability, and electron mobility.[164] Owing to their unique properties, CNDs have evolved as adaptable carbon nanostructures with several potential uses in a wide variety of biomedical disciplines including bioimaging, sensors and drug delivery (**Figure 1.5**).[164–166] For instance, several fluorescent CNDs have been developed to replace

commonly used cell-tracking dyes with advantages in terms of non-toxicity, faster internalization in the cells and great bioconjugation with bacteria.[165] Following the intense interest in using nanoparticles as biochemical sensors, CNDs are being proven more and more to be helpful in sensing chemical substances or elements. Based on the features of CNDs, particularly fluorescence capabilities and surface-functionalized chemical groups, several sensors for biological and chemical applications have been created. For instance, the application of CNDs as sensory probes to detect metal ions, chemical compounds, microRNA, pH, hemoglobin, and other biomolecules has been intensively investigated with the progress of CNDs.[167–169]

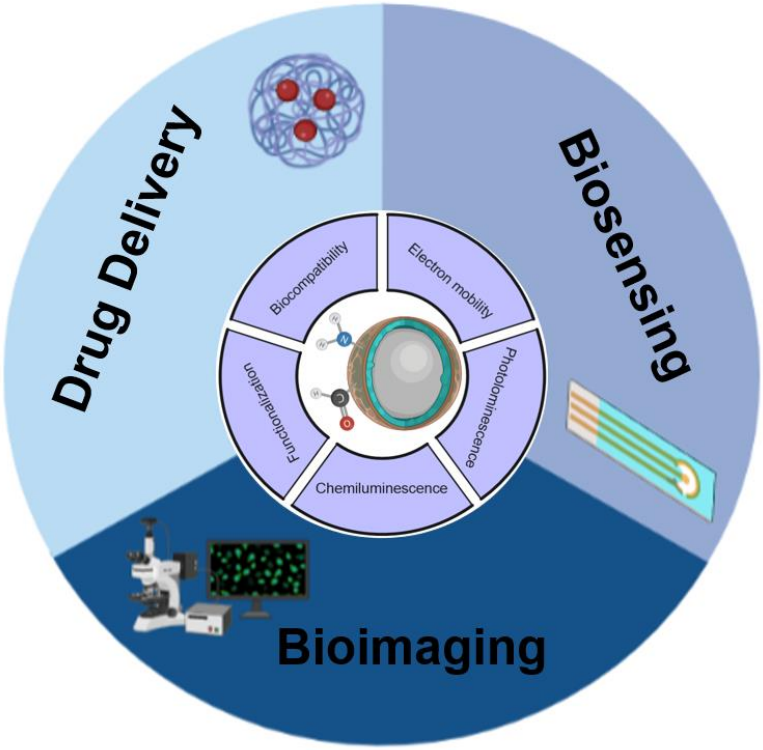

Figure 1.5: Biomedical applications of CNDs. *The illustration was created with BioRender.com*

Being a relatively new class of nanoparticles, the potentials of CNDs in the context of neural tissue engineering has not been fully explored. The few studies reported in the literature that explore the elicited effects of CNDs on different neuronal lines seem to suggest the necessity

of using CNDs as immobilized fillers in a hydrogel matrix.[170,171] In fact, pioneering studies have reported that treating cultured neurons or glial cells with CNDs in suspension caused apoptosis and the production of cytokines and reactive oxygen species. In addition, it has been shown that when directly exposed to neuronal cells, carbon-based nanoparticles can directly alter cellular functions and seed protein aggregation.[172] For instance, a recent study revealed that nanoparticle infiltration into the brain tissue can induce the accumulation of amyloid β (Aβ), an oligomer that is toxic for most nerve cells and that was shown to be implicated in several neuro-pathologies such as Alzheimer's disease. On the other hand, when carbon-based nanoparticles are anchored to a biocompatible hydrogel, they not only show low cytotoxicity but also elicit favorable responses in neurons and neural stem cells in terms of neurite outgrowth, synaptogenesis, electrophysiological activity and differentiation.[168,173]

1.3 Cell sources for *in vitro* studies

As the field of tissue engineering evolves, new obstacles appear in the way of the research and clinical translation of these artificial tissues and organs. The fundamentals of this interdisciplinary field not only involve identifying biomaterials and designing scaffolds that can guarantee better *in vitro* and *in vivo* performances but also require addressing reliable cell sources. Specifically in the context of neural tissue engineering, cell source represents a considerable concern that has hampered the advancement of our understanding of the functioning of the nervous system as well as the development of successful tissue engineering strategies. In fact, the hard isolation protocols for primary neurons together with the consideration that mature neurons do not undergo cell division have pushed the scientific community to seek alternative cell sources.

1.3.1 Primary and immortalized neuronal cell lines

Dissociated primary neuronal cultures represent an excellent *in vitro* tool to study CNS development, as well as neuronal maturation and functional activity, at the single-cell level and at the network scale. These cultures allow us to gain mechanistic insights in a simplified but more controlled context, compared to *in vivo* conditions.[174] The studies on primary neuronal cultures contributed to many fundamental discoveries regarding development such as neuronal polarization, neurite outgrowth, axon guidance (pathfinding), synaptogenesis and neuronal network formation, activity and maturation, recapitulating *in vitro* many aspects that occur *in vivo***.** [175] The most frequently used source for culturing primary neurons is the cortex or hippocampus of late embryonic or early postnatal rodents (i.e., rats and mice).[174–176] Primary neurons derived from other mammalian species have been less frequently used because of the scarce ability to maintain *in vitro* culture for more than 7 days. Primary tissue obtained from animals can improve biological relevance by containing many of the elements found *in vivo*; however, viability is short-term, and models lack adequate species specificity for robust testing. Studying the extremely specialized cells of the nervous system has always been particularly challenging, mainly due to the exceptionally specialized morphology of neurons and their inability to undergo mitosis after maturation. Despite the recent progress made in cell culture methods (i.e., use of advanced culture supplement formulations) that enable long-term *in vitro* survival of isolated mature neurons, the ethical concern of animal use still remains unaddressed. [176] In addition, most used primary neuron isolation protocols at best generate a neuron-enriched, mixed culture that also includes glia and stromal cells which may create undesired artefacts for certain applications.

Immortalized cell lines, such as human neuroblastoma SH-SY5Y, are cost-effective alternatives that provide preliminary insight into the responses of single cells. For purposes of modelling neuro-pathologies and simulating specific aspects of neuronal behavior driven by

the scaffold's physicochemical properties, the use of immortalized cell lines is likely the most easily accessible approach. These are isolated from neural tissue tumors or derived from cells transfected with oncogenes and provide readily proliferating cells that possess some neuronal characteristics.[177,178] For example, SH-SY5Y cells, one of the most used lines, are human neuroblastoma cells that are able to establish proliferative quiescence and differentiate into neuron-like cells. They can display dopaminergic phenotype and spontaneous/stimulated electrical activity and are often utilized in early compound testing for Parkinson's disease.[178] Other commonly reported cell lines include PC12 (rat pheochromocytoma cells), H4 (human glioma cells) and LUHMES (human mesencephalon cells), among others, all of which can be rapidly expanded simply using conventional cell culture media and FBS.[179] This practical utility is offset by significant limitations that make translation of *in vitro* results to humans challenging. For example, some of these lines have been employed for decades and have drifted phenotypically and genetically from their original cellular identity. This may lead to inter-laboratory and even inter-passage variability with inconsistent experimental results for a single cell line. [180,181] Furthermore, although the differentiated cells acquire several biochemical and electrophysiological neuronal characteristics, they fail to faithfully recapitulate the cellular phenotype of mature, fully differentiated neurons.[182,183]

1.3.2 Mesenchymal stem cells

Stem cells are a population of unspecialized cells with the ability to both self-renew and give rise to multiple cell types.[184] Such characteristics are the main reasons that have made stem cells garner significant attention from the scientific community. As most mature cells in the nervous system cannot replicate, stem cells represent an incredibly valuable source for both cell therapy and tissue engineering applications due to their immortal nature and ability to differentiate. There is an exciting potential for stem cells in tissue regeneration and repair that

may provide an alternative therapy to cell-based therapies in various diseases, particularly those affecting the nervous system. In this context, mesenchymal stem cells (MSCs), which are adult stem cells derived from the mesoderm and neuroectoderm, exhibit a high differentiation plasticity.[185] MSCs present some advantages compared to other stem cells namely accessibility, ease of *in vitro* expansion, reduced immunogenic properties and secretion of neuroprotective growth factors such as NGF.[186,187] In addition, recent studies have confirmed that MSCs have shown the capability to undergo neurogenic differentiation, expressing mature neuronal markers.[188] Taken together, such characteristics make MSCs an attractive cell source for several tissue engineering applications such as nerve repair, treatment/*in vitro* modelling of neural disorders and drug screening platforms. Several NGCs intended for peripheral nerve regeneration have been loaded with MSCs. A previous study showed that bone marrow MSCs in a polyglycolic acid nerve conduit could repair facial nerve defects in rats. [189] The results demonstrated that bone marrow MSCs can be successfully integrated into the conduits and survive up to 6 weeks in nerve tissue. In another study, researchers loaded bone marrow MSCs into a chitosan nerve duct and observed that the cells survived and proliferated within the construct for a period of 8–16 weeks, successfully promoting the repair of 8 mm nerve defects.[190] In a subsequent study, chitosan nerve conduits loaded with bone marrow MSCs not only accelerated the efficiency of nerve repair but also improved the quantity and quality of regenerated nerve fibers, obtaining a therapeutic effect comparable to autologous nerve transplantation.[191] The most promising application of mesenchymal stem cells in neurological disorders appears to be in the treatment of stroke and traumatic brain injury (TBI).[190] Regarding the former, the transplantation of MSCs in animal models, has been shown to reduce brain edemas while increasing axonal density and improving functional recovery.[192] The therapeutic effects of MSC transplantation were attributed to the secretion of factors such as NGF, and bFGF that promote axonal growth and neurogenesis and create a neuroprotective

environment.[193] Direct infusion of MSCs into injured brain attenuated TBI-induced motor and cognitive deficits in animals.[194] The experimental data showed that the treatment with MSCs stimulated the injured brain to induce trophic factors contributing to promoting neurogenesis, neuroprotection, and neural repair in TBI rats and mice. In a recent study, it was also demonstrated that MSC transplantation downregulated proinflammatory genes and upregulated anti-inflammatory genes in TBI rats' brains.[195]

1.3.3 Induced pluripotent stem cells (iPSCs)

Stem cells derived from embryonic tissues (ESCs) exhibit extensive self-renewal capabilities and can differentiate into cells belonging to the three germ layers. This makes them the most prominent stem cells for use in tissue engineering and regenerative medicine. However, the use of these cells is faced with practical and ethical problems. Isolation of stem cells from human or animal embryos is not only faced with legal and ethical obstacles but there is no general agreement on use.[196] Moreover, in practice, there are problems such as lack of histocompatibility, tumorigenicity, and infection during transplantation. As a result of introducing genetic modifications with four defined factors, Takahashi and Yamanaka obtained induced pluripotent stem cells (iPSCs), an inestimable source of autologous cells that present similar biological characteristic of ESCs but address their clinical and ethical that while preserving the biological characteristics of ESCs, can also address both their clinical and ethical shortcomings.[197] In fact, because of the large availability of sources (i.e., fibroblast, renal epithelial cells, peripheral blood cells) from which reprogrammable cells can be extracted, the need for invasive procedures is trumped. Since their discovery, iPSCs have become an invaluable source of differentiated cells and have paved the way to gain new insights on development, disease modelling and mechanisms, disease target identification, and therapeutic development.[200] Specifically, *in vitro* models of different neurodegenerative diseases such as

Parkinson's, Alzheimer's and Huntington's, have recently greatly advanced thanks to iPSCs as they can be derived from patients, providing a source of neurons carrying the same genetic variants associated with pathogenesis (**Figure 1.6B**). In the earliest study, iPSCs were cultured in undiversified 2D layers which were of limited value as disease models because they did not recreate authentic interactions between cells.[201]

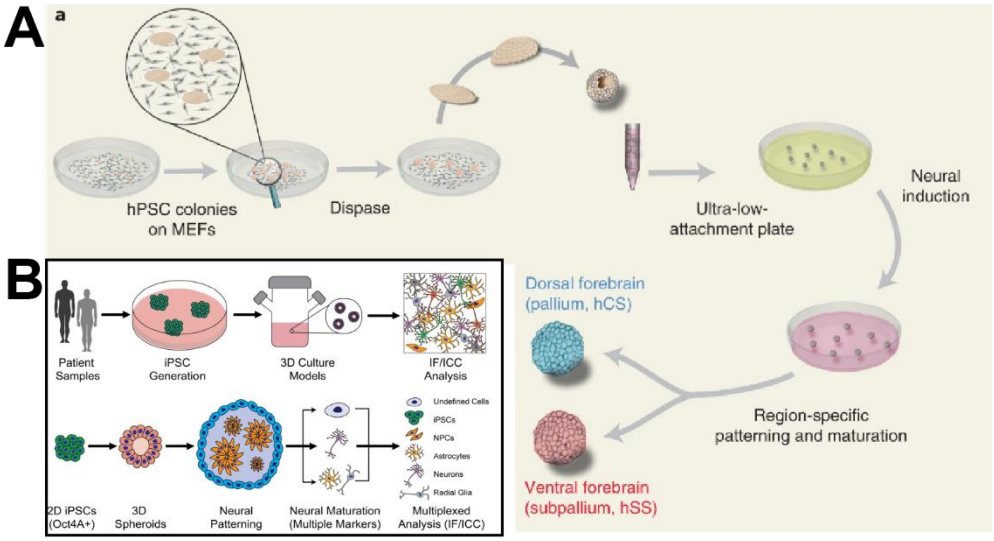

Figure 1.6: iPSCs-derived region-specific brain spheroids and dissociated neuronal population. (A) Schematic illustration of the main steps for the generation of brain region-specific spheroids from hiPSCs.[198] *Reproduced with permission from Springer Nature.* (B) Patient-specific reprogramming and neuronal differentiation of iPSCs cells.[199] *Copyright © 2021 http://creativecommons.org/licenses/by/4.0/.*

To overcome this drawback, more sophisticated 3D culture models were developed, including spheroids, hydrogels, scaffolds derived from the ECM, and organ-like cultures (**Figure 1.6A**). For instance, organoids/spheroids preserve the cellular interactions that capture key structural and functional aspects of real organs at the micrometre to millimetre scale. [202] Brain organoids/spheroids have recently emerged as invaluable tools to model the pathophysiology of diverse neurodegenerative diseases, facilitating a range of research applications including the analysis of disease mechanisms and progression, drug and testing, and cell therapy.

CHAPTER 2: Compounded topographical and physicochemical cueing by micro-engineered chitosan substrates on rat dorsal root ganglion neurons and human mesenchymal stem cells.

2.1 INTRODUCTION

A deeper and more sophisticated understanding of structure-function relationships governing cellular events at interfaces is a fundamental prerequisite not only to advance our knowledge of interfacial phenomena but also to develop better-performing biomaterials capable of directing key cellular processes for applications in neural tissue engineering and regenerative medicine.[203–205] In this context, increasing experimental evidence resulting from the employment of micro- and nano-engineered surfaces has unveiled the fundamental role of the substrate's topographical and physicochemical features in affecting the activity and ultimately determining the fate of neurons and stem cells, two of the most important cell types involved in nerve regeneration.[206–208] In particular, while on one hand the introduction of rationally designed topographical features (e.g., parallel microchannels, pillars) showed to direct neuronal and stem cell alignment and trigger morphological transitions,[209–213] on the other hand substrate's elasticity demonstrated to regulate activities such as adhesion, survival, proliferation, and differentiation.[214,215] In addition, signaling events that regulate cell-substrate interactions were shown to be sensitive to morphological parameters (porosity and roughness) as well as to the chemical make-up of the material.[216,217]

In this context, chitosan has been the material of choice for numerous neuronal tissue engineering applications, including hollow conduits for peripheral nerve regeneration and spinal cord repair.[218,219] To date, few studies have employed micro-patterned chitosan substrates to investigate the response of neuronal cells for advances of both fundamental and practical importance.[220,221] However, such previous work focused on the role of a dissociated variable (i.e. topography), overlooking the multifactorial nature of chitosan interfaces to which

cells are exposed *in vivo* during biomaterial-guided nerve regeneration.[222–224] It is in fact well known that, regardless of the type of interface, adhering cells are subjected to compounded physicochemical effects.[225,226] In order to obtain a more comprehensive understanding of how cells respond to chitosan substrates, it is thus critical to investigate cell behavior with *in vitro* platforms that allow modulating multiple properties in a systematic fashion.

To bridge this gap, we applied electrophoretic replica deposition (EPrD) to fabricate arrays of parallel microchannels with variable widths (20 and 60 μm) on chitosan, creating testing substrates consisting of variable micro-topographical features. Notably, this approach also allowed to introduce a surface roughness which better mimics the inner texture of implantable neuronal conduits.[227] In addition, since surface stiffness of both natural and synthetic biomaterials is a key variable at both the cellular and tissue levels,[228,229] we applied a chemical crosslinking process to (i) increase the long-term stability of chitosan in the cell-culture medium, (ii) replicate the mechanical requirements (i.e. bulk and surface stiffness) for hollow conduits employed in peripheral nerve regeneration and spinal cord repair[230–232] and successively (iii) to vary surface stiffness for the investigation of its role on cell behavior. This resulted in an experimental matrix which encompasses compounded topographical (i.e., surface roughness and microtopography), chemical (i.e., chitosan's surface chemistry and degradation products) and physical (surface stiffness) variables. Finally, we investigated the concerted effects of these topographical and physicochemical properties on dictating the response of neonatal rat dorsal root ganglia neurons (DRGs) and bone marrow-derived human mesenchymal stem cells (hMSCs). Our cellular results demonstrate that chitosan substrates exert geometry- and stiffness-dependent differential cueing on DRG neurons' alignment, network complexity, branch length, and number of neurites per soma, as well as on hMSC alignment, spreading and morphology. In addition, we investigated the direct role of micropatterns and substrate's elasticity in promoting the transition towards neurogenic

differentiation of human mesenchymal stem cells by ruling out any potential effect exerted by chitosan and/or citric acid molecules in solution. In conclusion, our study provides novel insights into the interplay between chitosan's physicochemical properties and the activity of relevant cells for neuronal tissue engineering applications. We discerned the individual role of topographical and physicochemical cues within a multifactorial platform which recapitulates key requirements for chitosan hollow conduits for nerve repair.

2.2 MATERIALS AND METHODS

2.2.1 Electrophoretic Replica Deposition (EPrD)

Medium molecular weight chitosan powder, with a degree of deacetylation of 83% (Sigma-Aldrich, USA, Cat. No. 448877, Lot # STBG1894V) was added to a concentration of 5 g L^{-1} in a solution of 1% (*v/v*) acetic acid (AcOH) and distilled water (dH_2O). The resulting solution was first stirred for 24 hours (h) at room temperature (*RT*) to ensure complete dissolution of the chitosan powder and successively used as the electrolyte in an electrochemical cell composed of a central double-faced 2 x 1 cm^2 titanium cathode and two graphite rod anodes.

A 2425 Sourcemeter potentiometer (Keithley Instruments, USA) was used in potentiostatic mode to generate a square waveform with 30 second (sec) periods consisting of V_{max} = 100 V for 10 sec and V_{min} = 0 V for 20 sec (**Figure 2.1A**, *Step I*). The deposition was carried out for a total of 30 minutes (min) at 23 °C at a pH of 3.6. The cathode was laser-engraved with parallel grooves of variable geometry to instruct the electrodeposition of chitosan into positive replicas consisting of aligned ridges with regular spacing and height. This ultimately allowed to engender chitosan substrates exhibiting arrays of parallel channels with a pitch distance of 20 µm (P20) and 60 µm (P60). A smooth cathode was used to generate un-patterned chitosan controls (NP) (**Figure 2.1A**, *Step II*). After the EPrD process, coated cathodes were immersed in a 0.1 M solution of NaOH for 5 min to permit the detachment of deposited chitosan. The

resulting substrates were rinsed with dH_2O and dried at 37 °C for 2 h between silicone sheets to avoid sample crumpling. Crosslinking of chitosan was achieved via a novel multistep protocol that combined the use of citric acid (CA) and high-temperature treatment. In particular, as-deposited (NC) un-patterned controls and patterned substrates were first coated with 200 µL of a crosslinking solution consisting of CA (5% *w*/*w* with respect to chitosan sample weight) and NaH_2PO_4 (2.5% *w/w*) in dH_2O. Samples were air-dried for 2.5 h at 37 °C (**Figure 2.1A**, *Step III*) and successively incubated at either 165 °C (C165) or 190 °C (C190) for 15 min (**Figure 2.1A** , *Step IV*) to promote the pyrolytic decomposition and decarboxylation of CA to cyclic anhydride.[233] These highly reactive molecules induce the formation of covalent bonds between their -COOH groups and the amine groups of the chitosan chains (**Figure 2.1A** , *Step V*).[234]

Notably, while for the physicochemical characterization and biological assays presented in this work we used planar substrates (**Figure 2.1B**), this method lends itself to the generation of hollow cylindrical structures (**Figure 2.1C**), a fundamental prerequisite for the clinical translation of EPrD towards the fabrication of micropatterned chitosan peripheral nerve conduits.

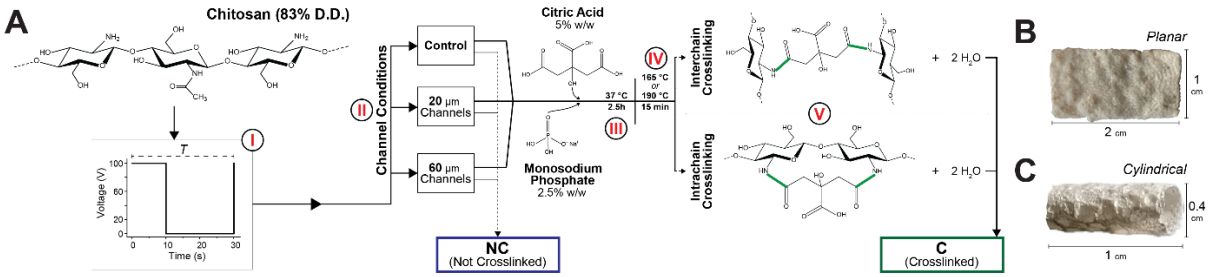

Figure 2.1: Schematic overview of chitosan sample preparation. (A) Visual representation of the experimental protocol for the creation of chitosan micropatterned/crosslinked substrates investigated in this study. Electrodeposited chitosan (B) film and (C) cylindrical structure.

2.2.2 Swelling and Degradation

Water and degradation were quantified over time on all experimental conditions of both as-deposited (NC) and crosslinked (i.e., C165, C190) chitosan. The dry weight was measured

before immersion in 4 ml of phosphate-buffered saline solution (PBS, pH 7.4) and incubation at 37 °C to simulate physiological conditions. At different time intervals, samples were removed from the solution, gently blotted and weighed in their swollen state on a high-sensitivity (10 µg) scale. Finally, samples were dried at 37 °C for 24 h before recording their final dry weight. The swelling ratio (*SWR*) was calculated as $\boldsymbol{SWR}\ (\boldsymbol{t}) = \left(\frac{\boldsymbol{W_t - W_0}}{\boldsymbol{W_0}}\right)$,[235] where w_0 is the initial dry weight and w_t is the weight in the swollen state at a specific time point. Percent degradation (%*DEG*), signified by mass loss, was calculated as $\%\boldsymbol{DEG}\ (\boldsymbol{t}) = \mathbf{100}\ (\mathbf{1} - \left(\frac{\boldsymbol{w_0 - w_t}}{\boldsymbol{w_t}}\right)$,[236,237] where w_0 is the initial dry weight and w_t is the final dry weight of samples at a given time point. The PBS solution was renewed every 3 days to mimic cell culturing conditions. The supernatant was collected for the subsequent FT-IR spectroscopy analysis to complement the degradation data with information on the chemical composition and concentration of the degradation products in solution.

2.2.3 Fourier Transform Infrared (FT-IR)

A Nexus 870 (ThermoFisher, USA) FT-IR system was used in transmission mode. Spectra were collected at a resolution of 2 cm-1 in the 700–1900 cm-1 region and consisted of 128 scans at 1 sec per scan. Five randomly selected samples per condition were analyzed, and one spectrum per condition was recorded (n = 5). Baseline subtraction, data normalization and Voigt (Lorentzian/Gaussian) deconvolution for identification of vibrational components were performed in OriginPro (OriginLabs, USA). The 1151–1156 cm-1 band, representing the β-1,4 glycosidic bond between chitosan monomers, was used as the reference peak for the normalization and comparison of spectra.[238–240] The degree of crosslinking was assessed by tracking changes in the 1581–1587 cm-1 and 1306–1322 cm-1 bands associated with N-H stretching of amide II and the C-N stretching relative to the amide III, respectively.[241,242] Peak

assignment of the additional bands considered in this study was carried out according to previous literature (**Table 2.2**).[206,233,242–245,234–241]

To gain additional insights on the possible effects of degradation on neurogenic differentiation, ATR-FTIR (SMART ARK module, ThermoFisher) was used to analyze the degradation products released by as-deposited (NC) and crosslinked (C190) chitosan immersed in PBS 1X for 3 weeks. To this end, the supernatant was collected every 3-4 days during the 3-week interval in order to imitate the medium change during culturing. While the C-C stretching / O-H deformation (1032 cm^{-1}) and the C-H_2 deformation (1467 cm^{-1}) bands were employed to detect the presence of citric acid and highlight chemical differences in the degradation products between the two conditions, the C-N stretching band (1311 cm^{-1}) provided relevant insight on the chemical configuration of citric acid molecules within the sample byproducts. The three bands were normalized with respect to a common reference peak centered at 1142 cm^{-1} (C-O-C glycosidic bond) to neutralize potential errors due to inter-sample variability. To account for potential variations of acidity/alkalinity, the pH of the supernatants was also measured.

2.2.4 Atomic Force Microscopy (AFM).

Topographical and nanomechanical characterizations of substrates were achieved with the AFM module of the alpha300 RSA system (WITec) in contact mode. Topography was imaged by using the rectangular Si_3N_4 Cantilevers of the CONTV-A chip (Bruker, USA), characterized by a nominal spring constant (k) of 0.2 N m^{-1}, a resonant frequency (λ_{res}) of 13 kHz and nominal tip radius (R) of 8 nm. 3D micrographs were processed in Gwyddion to quantify depth profiles for both the cathodes and chitosan patterns.[246] Root mean square roughness (RMS) was extracted from 5 x 5 μm^2 regions randomly selected along the microchannels. Nanomechanical data were recorded using the FMV-A chip (Bruker), characterized by k = 2.8 N m^{-1}, λ_{res} = 75

kHz and R = 8 nm. A time course of nanoindentations was performed on samples immersed in PBS at 37 °C, with timepoints ranging from 1 h to 14 days (d). Raw data were converted to force–indentation curves in OriginPro according to a previously published protocol,[247,248] and the determination of stiffness values were obtained by linear regression of the first 250 nm of indentation from the contact point.

2.2.5 Uniaxial Tensile Test.

All samples were preconditioned in PBS 1X to achieve their swollen equilibrium state. The tensile tests, performed on a Biotester machine (CellScale, Canada), consisted of an initial deformation ramp at a constant loading rate of 1.8 cm min^{-1} up to 40%, followed by a 30 sec hold phase and the final recovery. The axial test was performed in the longitudinal direction with respect to the channels' principal axis. The bulk stiffness was calculated by fitting the linear portion of the force-displacement curve. Stress and strain were calculated from the raw data as the change in length divided by the initial length and the force divided by the nominal sectional area of the specimen, respectively. The Young's modulus was calculated from the initial slope of the stress-strain curve.

2.2.6 Culturing and Imaging of Dorsal Root Ganglia Neurons (DRGs).

Rat neonatal DRGs from QBM Cell Science (Ottawa, Canada) were suspended in Neurobasal™ medium (ThermoFisher) complemented with 10% fetal bovine serum (FBS, Gibco, USA), B27 (2%), L- glutamine (1%), penicillin (1%) and streptomycin (1%), all purchased from Fisher Scientific (USA). Successively, cell suspension aliquots, with a cell density of 40,000 cells ml^{-1}, were seeded onto the chitosan samples, previously coated with a 50 µg ml^{-1} poly-D-lysine (Sigma-Aldrich, Cat. No. P6407) solution overnight at RT and subsequently with a 2 µg ml^{-1} laminin (Sigma-Aldrich) solution for 2h at 37 °C. After 4 h of

incubation, the medium was replaced with Neurobasal™ complemented with 0.5% uridine (Sigma-Aldrich) and 0.5% 5-Fluoro-2-deoxyuridine (Sigma-Aldrich) for mitotic inhibition.After 14 days, DRGs were fixed in 4% paraformaldehyde (PFA) for 10 min at room temperature and then washed three times in PBS. The fixed cells were permeabilized with 0.25% Triton-X100 (Sigma-Aldrich) and blocked in 3% bovine serum albumin (BSA, VWR, USA) PBS solution for 4 h at room temperature. The DRGs were successively labelled with a primary anti-beta III tubulin, mouse monoclonal antibody (ab78078, Abcam, UK) at a dilution of 1:1000 overnight at 4° C, followed by a secondary Goat anti-Rabbit IgG antibody, conjugated to Alexa Fluor 488 (ThermoFisher) at a dilution of 1:500 for 35 min at 37 °C. Neurons were imaged on an LSM880 AxioObserverZ1 confocal microscope (Zeiss) with a 10X EC Plan-Neofluar (Ph1) objective (NA = 0.3, Zeiss). An automated Strahler analysis (ImageJ Neurite Tracer plugin) was applied to defined 500 µm square ROIs, enabling the quantification of the branching complexity of the neural architecture and the average branch length. Specifically, by employing the Skeleton analysis, we calculated the percentage of triple and quadruple points, defined as junctions with three and four branches, respectively. This also allowed us to calculate double points as the total number of junctions minus the sum of triple and quadruple points. Furthermore, the number of neurites per soma as well as the confinement index, defined as the percentage of neurites confined within the channel walls, were manually quantified.

2.2.7 Culturing and Imaging of Bone Marrow-Derived Human Mesenchymal Stem Cells (hMSCs).

To mitigate inter-donor variability, different sources of hMSCs from two different distributors (Lonza and RoosterBio, USA) were used in this study. hMSCs from Lonza (Lot. 603525) were expanded in their MSCGM Bulletkit (Lonza). hMSCs from RoosterBio (Lot.

00082) were expanded in their Rooster-Nourish-MSC media kit (RoosterBio). Culturing was performed in Dulbecco's Modified Eagle Medium (DMEM, Corning, USA) with 4.5 g L^{-1} glucose and L-glutamine (Corning), supplemented with 8% fetal bovine serum (FBS, Gibco), 100 U ml^{-1} penicillin and 100 U ml^{-1} streptomycin (Gibco). Passaging was performed with 1X TrypLE (Gibco), inactivated by dilution with serum-containing media and centrifuged at 170 g for 10 min. The cell-laden pellet was resuspended in fresh media to attain the desired experimental concentration of 15,000 cells ml^{-1}. Cells were cultured in a humidified 37 °C water-jacketed incubator with 5% CO_2.

After 1 and 4 d, cells were fixed in fresh 4% PFA at RT for 10 min and subsequently washed in PBS. Cells were permeabilized with 0.25% Triton-X100 (Sigma-Aldrich) for 10 min and blocked with 3% BSA at RT for 4 hours. Nuclei were stained with NucBlue ReadyProbes reagent (ThermoFisher) and the actin cytoskeleton was stained via Rhodamine conjugated Phalloidin (ThermoFisher) using manufacturer guidelines. Multi-channel images, to assess morphology, were captured on an AxioObserver.Z1 inverted epifluorescence microscope (Zeiss) through a 20X Plan-Apo (Ph2) objective (NA = 0.8, Zeiss). The extraction of relevant parameters associated with cell morphology was carried out on ZEN 2.6 software (Zeiss). The spreading area was manually calculated from randomly selected individual cells. The aspect ratio, a morphological index describing the body elongation in a specific direction, was determined by calculating the ratio between the major and minor axes. The degree of orientation of the cell body with respect to the channel's longitudinal axis was evaluated by quantifying the offset angle formed by the closest channel wall and the cellular body's major axis. To visually display the relative frequency distribution of alignment angles, we divided the 90° angle range into six 15°-wide bins.

2.2.8 Neurogenic Differentiation of hMSCs.

To evaluate the capacity of the chitosan surfaces to induce neurogenic differentiation, two different culture media were used for comparison. Unadulterated culture media, composed of DMEM (Corning) with 4.5 g L^{-1} glucose and L-glutamine (Corning), supplemented with 8% FBS (Gibco), 100 U ml^{-1} penicillin and 100 U ml^{-1} streptomycin (Gibco), was selected as the control condition. In the second experimental culturing condition, control media with the addition of 25 ng ml^{-1} human basic fibroblast growth factor (bFGF, PeproTech, USA, #100-18B) was employed to stimulate the neurogenic differentiation.[249,250] At 1 (control) and 21 days, cells were fixed in fresh 4% PFA, permeabilized with 0.25% Triton-X100 (Sigma-Aldrich) and blocked with 3% BSA at RT for 4 hours. The microtubule element βIII-tubulin, encoded by the neurogenic TUBB3 gene, was labelled with a primary Tuj-1 rabbit pAb (ab18207, Abcam) at a dilution of 1:1000 overnight at 4 °C, followed by a secondary goat anti-rabbit IgG, conjugated to Alexa Fluor 488 (ThermoFisher) at a dilution of 1:500 for 35 min at 37 °C. The actin cytoskeleton was stained via rhodamine-phalloidin (ThermoFisher) following the manufacturer guidelines. Cells were imaged with a Leica BMI16000B inverted microscope (Leica Microsystems, Germany) configured with a Quorum Spinning-disk Confocal (Quorum Technologies, Canada) through a 20X HC Plan APO objective (NA = 0.7, Zeiss). Multi-channel z-stack images were acquired with constant exposure time. Image sets were successively processed in FIJI for background subtraction and the generation of a maximum projection. Each channel of the corresponding sets was made binary according to a fixed threshold. Neurogenic differentiation was quantified via the activity of the TUBB3 gene, indicated by the expression and distribution of βIII-tubulin in the cell. For the quantification of neuronal differentiation, we calculated the ratio βIII-tubulin signal (GFP) over actin (Rhodamine). In addition, we quantified the aspect ratio of the cell body to track the

morphological transition towards a neuron-like cellular shape, as previously reported in literature.

2.2.9 Statistical Analysis.

All biological experiments in this work were performed in triplicates (three samples per condition) and repeated for at least three independent experiments (n = 9). The Shapiro- Wilk test was used to test the normal distribution of the data sets. One-way analysis of variance (ANOVA) was used to compare the values among multiple groups supplemented with Tukey's post-hoc test for mean comparisons. Differences were considered statistically significant at $p < 0.05$.

2.3 RESULTS AND DISCUSSION

2.3.1 Morphological Characterization

Smooth and laser-engraved titanium electrodes were employed individually as cathodes in the EPrD process to create, respectively, un-patterned controls (NP) and micropatterned chitosan substrates characterized by parallel microchannels with variable widths (i.e., 20 µm and 60 µm) and constant spacing and depth (i.e., 20 µm and 10 µm, respectively), hereafter referred to as P20 and P60. To validate the dimensional accuracy of the transfer process, a 3D morphological investigation was carried out by AFM. Micrographs of the engraved cathodes and the resulting micropatterns are shown in **Figure 2.2A** and **2.2B**, respectively. Profile analysis (**Figure 2.2C**) allowed us to quantitatively compare the channels' geometry, i.e., width (w), spacing (s), and depth (d) to that of the cathodes (**Table 2.1**). For both P20 and P60, no significant differences were measured between the chitosan substrate and the engraved cathode. Moreover, this fabrication technique intrinsically yielded a variable surface

roughness. As shown in Figure 2.2D, the highest RMS values were displayed by the un-patterned samples.

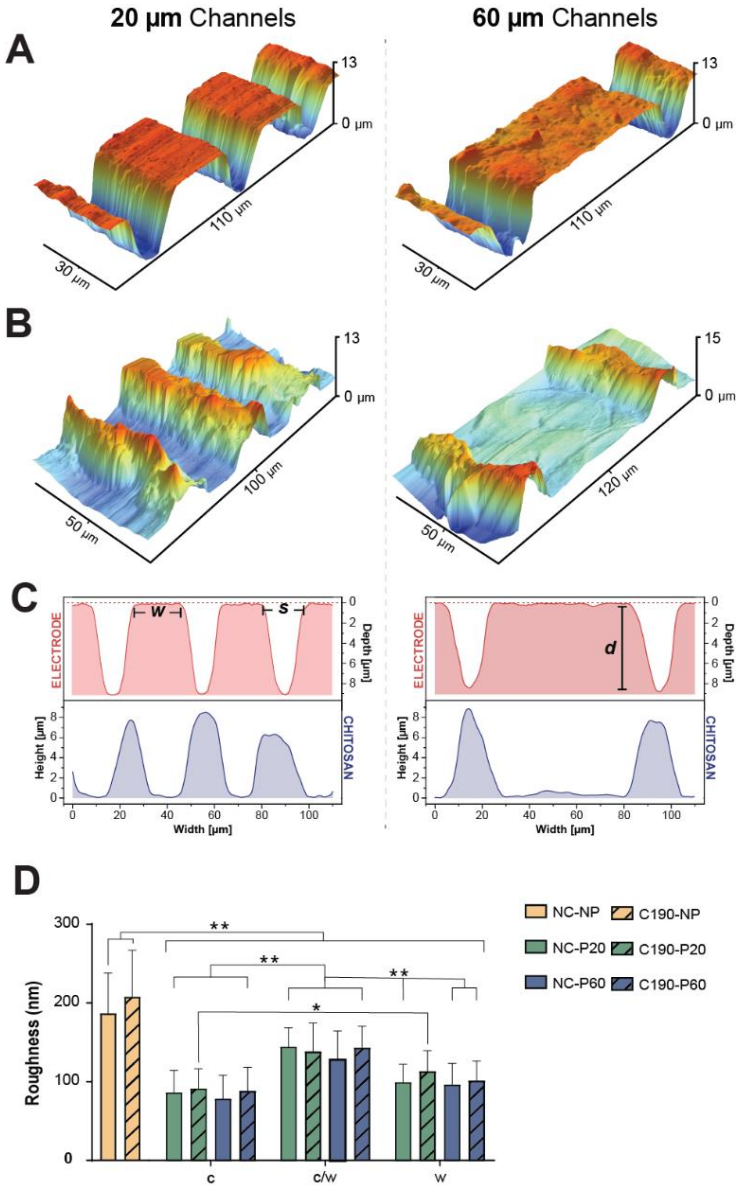

Figure 2.2: Topographical characterization of the employed titanium cathodes and of the electrodeposited chitosan substrates. AFM micrographs of (A) micromachined titanium electrodes and (B) the resulting electrodeposited chitosan substrates. (C) Representative AFM line profiles of both titanium cathodes and deposited chitosan films. (D) RMS roughness values. For patterned samples, RMS roughness measurements were carried out in the central region of the channels (*c*), at the channel/wall interface (*c/w*) and on the wall (*w*).

NC-NP and C190-NP displayed respectively an average RMS roughness of 187 nm and 208 nm with no statistically significant differences. Interestingly, both the patterned samples

displayed a roughness gradient along the surface profile in which the highest values were detected at the channel/wall interface (144 ± 24 nm for NC-P20 and 128 ± 36 nm for NC-P60) while the channel's central region was characterized by the lowest values (86 ± 29 nm for NC-P20 and 78 ± 30 nm for NC-P60). The same trends were also found for the crosslinked conditions. In this case, the average RMS roughness found at the channel/walls interface was 138 ± 36 nm for C190-P20 and 143 ± 27 nm for C190-P60, while in the central region of the channel, the values decreased to 91 ± 25 nm and 88 ± 31 nm, respectively. This constitutes an important aspect in the *in vitro* recapitulation of clinically relevant properties since roughness is known to positively influence cell adhesion,[251,252] a parameter which was overlooked in previous work with micro-engineered chitosan channels.

Table 2.1: Topographical analysis of patterned titanium electrodes and their corresponding chitosan films. Data are expressed as average ± SD.

Channel/Engraving	**20 µm Channels**		**60 µm Channels**	
Parameter	**Electrode**	**Chitosan**	**Electrode**	**Chitosan**
Width (*w*)	23 ± 3	22 ± 3	60 ± 3	61 ± 3
Spacing (*s*)	17 ± 3	18 ± 2	18 ± 2	19 ± 3
Depth (*d*)	9 ± 2	9 ± 1	10 ± 2	9 ± 2

2.3.2 FTIR Results

We complemented the morphological characterization with FTIR analysis to close in on the chemical make-up of chitosan substrates. **Figure 2.3A** displays a representative FTIR spectrum of the as-deposited chitosan (NC, black) as well as of the material crosslinked at 165 °C (C165, blue) and 190 °C (C190, red). The main bands related to the vibrational modes of specific functional groups were assigned according to literature and are reported in **Table 2.2**. Evident

differences can be observed between the NC and the crosslinked conditions. In particular, the presence of CA molecules in the crosslinked samples was revealed by the statistically significant increase of the absorption band centred at ~ 1034 cm^{-1} (F2), which corresponds to the C-C stretching and O-H deformations in citric acid. As shown in **Figure 2.3B** (*left*), the area relative to this band doubled in the crosslinked samples and increased from an average of 0.8 for the NC samples to 1.6 and 1.9 for the C165 and C190 conditions, respectively.

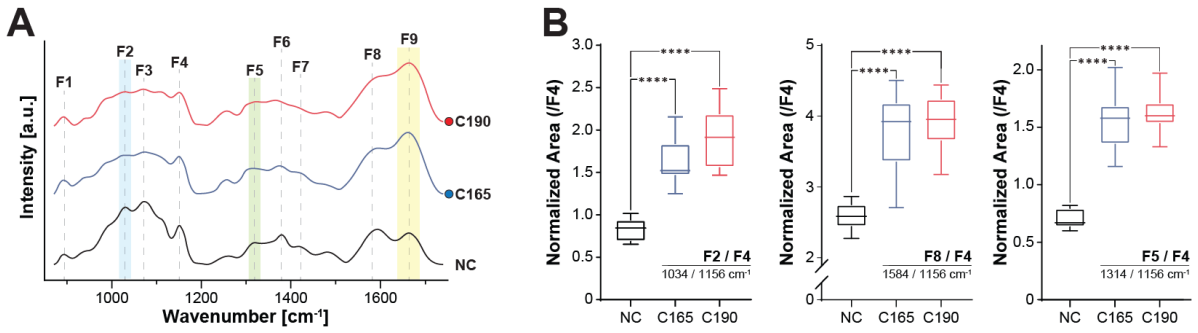

Figure 2.3: FTIR analysis of the pristine and crosslinked chitosan substrates. **(**A) Representative FTIR spectra for as-deposited (NC) and CA crosslinked chitosan treated at 165 °C (C165) and 190 °C (C190). For clarity, each band was labeled with a code ranging from F1 to F9, reported in Table 2. (B) Quantification of F2/F4, F8/F4 and F5/F4 band area ratios obtained from FTIR spectra.

Table 2.2: FTIR vibrational modes.

FTIR Assignment		
Ref.	**Position (cm^{-1})**	**Description**
F1	897 ± 1	C-H (def. out plane)
F2	1034 ± 4	C-O (stretch.), O-H (def.)
F3	1075 ± 2	C-O (stretch.)
F4	1156 ± 2	C-O-C (stretch.)
F5	1314 ± 8	C-N (stretch.); [*Amide III*]
F6	1375 ± 3	$C\text{-}H_3$ (def. sym)
F7	1416 ± 2	$C\text{-}H_2$ (def. sym.)
F8	1584 ± 3	N-H; [*Amide II*]
F9	1660 ± 3	C=O; [*Amide I*]

The formation of covalent bonds between the NH_2 group of chitosan and the COOH group of CA driven by the thermal treatment was demonstrated by considering the bands at 1584 cm^{-}

^{1} (F8) and 1314 cm^{-1} (F5), which represent the amide II associated with N-H vibrations and the amide III related to C-N stretching, respectively. The evident increase of both these peaks in the treated samples with respect to as-deposited controls indicates the transition from a primary to a secondary amine group resulting from the formation of a new amide. The average normalized area relative to N-H vibrations (**Figure 2.3B**, *middle*) was found to be 2.6 for NC, and it increased to 3.8 and 3.9 for C165 and C190, respectively.[233,236,238,242–244] Finally, the normalized area of C-N vibrations increased from 0.7 for NC to 1.5 and 1.6 for the treated samples (**Figure 2.3B**, *right*).

FTIR spectroscopy provided consistent information regarding the chemical arrangement resulting from a successful CA-based crosslinking, reflecting the presence of CA molecules as well as the formation of new C-N covalent bonding in the crosslinked conditions when compared to as-deposited chitosan. These findings were further supported by Raman spectroscopy analysis (**Figure S2.1**, **Table S2.1**, **Appendix**).

2.3.3 Swelling and Degradation Studies

To mirror the dynamic changes which occur in chitosan substrates due to medium absorption during cell cultures, which may change the surface stiffness while releasing degradation products in solution, we characterized the swelling and degradation behaviors. After validating that the surface micropatterns do not affect the physical stability of chitosan in the culture medium (**Figure S2.2A, B**, **Appendix**), we focused our analysis on the NP conditions to specifically single out the effects of crosslinking. As expected, treating chitosan with CA played a key role not only in decreasing the early water uptake but also in slowing down the overall swelling process. As shown in **Figure 2.4A**, while the NC samples reached their maximum swelling (8.6) after 1 h, both C165 and C190 reached their swelling plateau (i.e., 5.8 and 2.7, respectively) after a much longer time (24 h). These findings can be attributed

to the reduced availability of the highly hydrophilic free amines and intermolecular covalent bonds within the polymeric chain network of cross-linked samples. After this initial phase, all three conditions achieved the equilibrium state. After 4 days, however, NC samples began to experience a decrease in water content due to a likely mass loss, peaking at a 33% reduction after two weeks. On the other hand, C165 and C190 maintained a constant water content over the entire length of the experiment. The same trend was observed by accounting for the mass loss in the calculation of the swelling ratio (**Figure S2.2C**, **Appendix**). Because of the high variability in published results due to several variables that have a significant impact on the resulting swelling behavior (e.g., degree of deacetylation, molecular weight, fabrication technique), how our swelling data compare with the existing literature is not univocal. [253–255] We can nonetheless explain the slightly higher swelling ratios obtained in this study by considering that EPrD is known to introduce a significant porosity in the deposited substrates, thereby facilitating water absorption.

Mass loss resulting from PBS immersion is shown in **Figure 2.4B**. This is a particularly important factor since the release of chitosan degradation products and/or the presence of citric acid in solution could potentially affect cellular response, in particular stem cell differentiation.[256] As expected, the surface topographies did not affect the degradation rate of the samples (**Figure S2.2D**, **Appendix**). While the NC samples exhibited a mass loss of 9% within the first 6 h, C165 and C190 only lost 4% and 3%, respectively. The total mass loss after 2 weeks was 21% for NC, 9% for C165 and 8% for C190. Notably, the values obtained for the NC condition as well as the lower degradation rates showed by the CA-treated samples are supported by previous studies.[257,258]

To gain additional insights on chitosan degradation, we carried out ATR-FTIR analysis of the supernatant to rule out potential effects of chitosan monomers and/or free citric acid molecules on the subsequent cellular assays. Because the degradation between the two

crosslinked conditions was similar (**Figure 2.4B**), we only considered the C190 samples for this analysis. **Figure 2.4C** displays representative ATR-FTIR spectra of the supernatant collected from NC-NP (*top*) and C190-NP (*bottom*) in the 3-week interval. The presence of citric acid in the degradation products of the treated C190 samples was revealed by the increased normalized area of two characteristic bands, namely the C-C stretching / O-H deformation (1032 cm^{-1}) and the C-H_2 vibrations (1467 cm^{-1}).

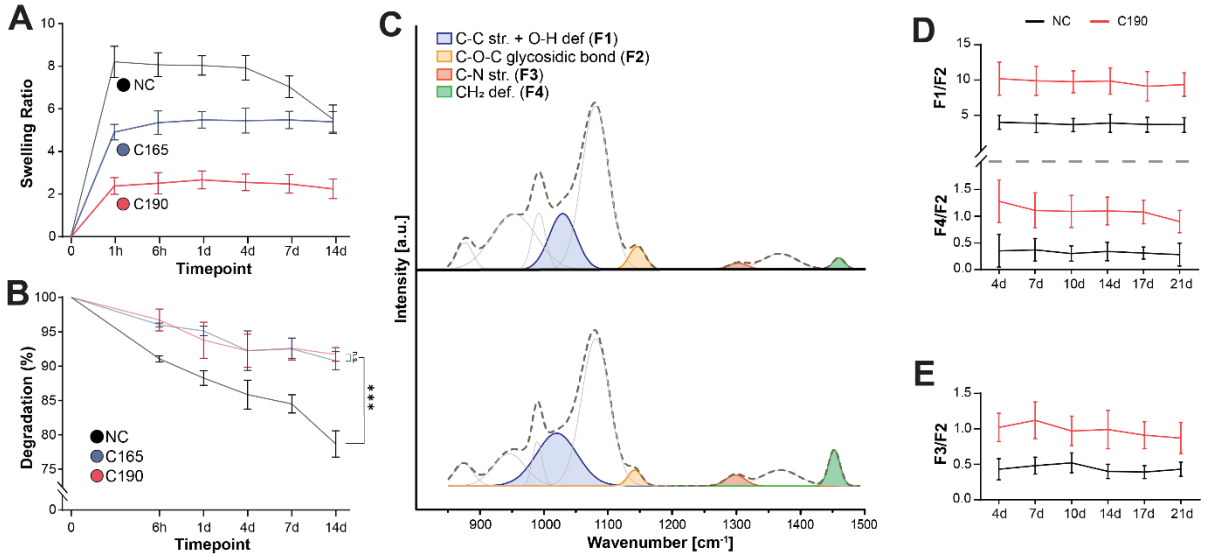

Figure 2.4: Swelling and degradation study of pristine and crosslinked chitosan substrates and ATR-FTIR analysis of degradation supernatant. Percentage variations of (A) swelling and (B) degradation as a function of time for as-deposited (NC) and CA crosslinked chitosan treated at 165 °C (C165) and 190 °C (C190). (C) Representative ATR-FTIR spectra of the supernatant collected from a PBS solution in which NC-NP (*top*) and C190-NP (*bottom*) samples were immersed. (D) Normalized area of the C-C stretching / O-H deformation (F1/F2) and CH_2 deformation bands at different timepoints. (E) Normalized area of the C-N stretching band at different timepoints.

As shown in **Figure 2.4D**, the normalized area of the former (F1/F2) was significantly higher for C190 samples (~ 10.2-9.1) when compared to untreated (~ 4.0-3.6) for all the time points tested. Such consideration was also valid for the normalized area of the C-H_2 deformation band (F4/F2) that was significantly higher in the treated group (~ 1.3-0.9) with respect to the untreated (~ 0.5-0.3) throughout the entire experiment. Taken together, these trends unveil the presence of citric acid molecules within the degradation products of the

treated samples. We successively analyzed changes in the C-N stretching band. This band is related to vibrations of the covalent bond which forms during the crosslinking process between the citric acid -COOH groups and the amine groups of the chitosan chains. As shown in **Figure 2.4E**, C190 samples displayed a normalized area ranging from 1.1 to 0.9 which was significantly higher than the values found for the NC condition (~ 0.5-0.4) throughout all the recorded timepoints. This finding suggests that rather than being liquid-dispersed standalone byproducts, the citric acid molecules detected in the C190 supernatant are covalently bound to amine groups of the chitosan chains.

Furthermore, the analysis of the pH fluctuations provided supplementary evidence supporting this conclusion. While the presence of citric acid molecules in solution is expected to give rise to a more acidic environment, the supernatants collected from both conditions (NC and C190) were indeed characterized by the same pH values of ~ 7 after 4 days, indicating that no free citric acid was dissociated in solution.

2.3.4 Mechanical Characterization

The nano- and micro-scale mechanical properties of chitosan samples were investigated by quantifying the surface and bulk stiffness, critical parameters that, respectively, dictate the *in vivo* interfacial biological events (e.g., adhesion, proliferation, and matrix deposition) and determine the overall biomechanical performance of tissue engineering constructs. [259,260] With this analysis we aimed at confirming that the surface stiffness and variations thereof remained within the viable range for implantable neuronal conduits.

To this end, we first carried out AFM indentation curves over 2 weeks on samples immersed in PBS 1X at 37 °C to simulate the physiological environment cells are exposed to during cultures. Notably, we carried out comprehensive AFM characterization of NP samples for each of the three crosslinking conditions, after having ensured that the surface micropatterns do not

affect the nanomechanical properties (**Figure S2.3A**, **Appendix**). **Figure 2.5A** highlights the significant enhancement of the surface stiffness in C165 and C190 samples when compared to the NC condition. NC samples exhibited stiffness of ~ 0.2 N m^{-1} at 1 h, which experienced a 40% reduction after 14 days. On the other hand, C165 and C190 showed a less pronounced decrease of their nanoscale stiffness of ~ 30%, with a maximum in the 0.6-0.7 N m^{-1} range at 1 h and a minimum in the 0.4-0.5 N m^{-1} range after 14 days. On top of an overall mechanical enhancement, statistical analysis demonstrates the beneficial impact of the crosslinking process in preserving the mechanical properties for a prolonged period. While in the NC samples the mechanical properties deteriorated within the first 4 days, the treated samples did not undergo significant changes during the first week of the experiment.

Successively, we conducted uniaxial tensile tests on samples in their swollen equilibrium state to ensure that the values obtained for both NC and crosslinked conditions matched the clinical requirement, i.e. proximity to the Young's modulus of human nerves.[222,225] Because of the similarities between the C165 and C190 conditions unveiled by degradation (**Figure 2.4B**) and AFM analysis (**Figure 2.5A**), we opted for only considering the latter, which encompassed both un-patterned and patterned substrates. **Figure 2.5B** shows the loading cycle to which the samples were subjected, together with the images of the macroscopic samples before and after uniaxial deformation. **Figures 2.5C-D** display the stiffness and Young's modulus, respectively, measured when NC and C190 un-patterned controls and patterned samples were stretched longitudinally with respect to the channel's direction. Our measurements indicate that the crosslinking also enhances the bulk stiffness, thereby demonstrating that the treatment affected the entire thickness of the samples and not only the surface exposed to CA. As shown in **Figure 2.5C**, the stiffness values increased from 0.3-0.4 N m^{-1} for the NC condition to 0.5-0.6 N m^{-1} in C190 samples. As expected, the patterned samples of both un-treated and crosslinked conditions, revealed a decrease in the longitudinal stiffness compared to the flat samples.

ANOVA analysis depicted a significant difference between NC-NP and NC-P20 and C190-NP and C190-P20. These findings are associated with a significant reduction in the thickness of patterned samples (**Figure S2.3D**, **Appendix**) due to a higher deposition area on the cathode surface (2.0 cm^2 NP, 2.9 cm^2 P60 and 3.5 cm^2 P20). Finally, to investigate the potential presence of mechanical anisotropy introduced by the preferential alignment of the channels, all patterned samples were also submitted to axial tensile tests with the load applied transversally to the channels' orientation. The results obtained in this configuration did not show any significant differences with the ones obtained with the load applied longitudinally (**Figure S2.3B, C**, **Appendix**).

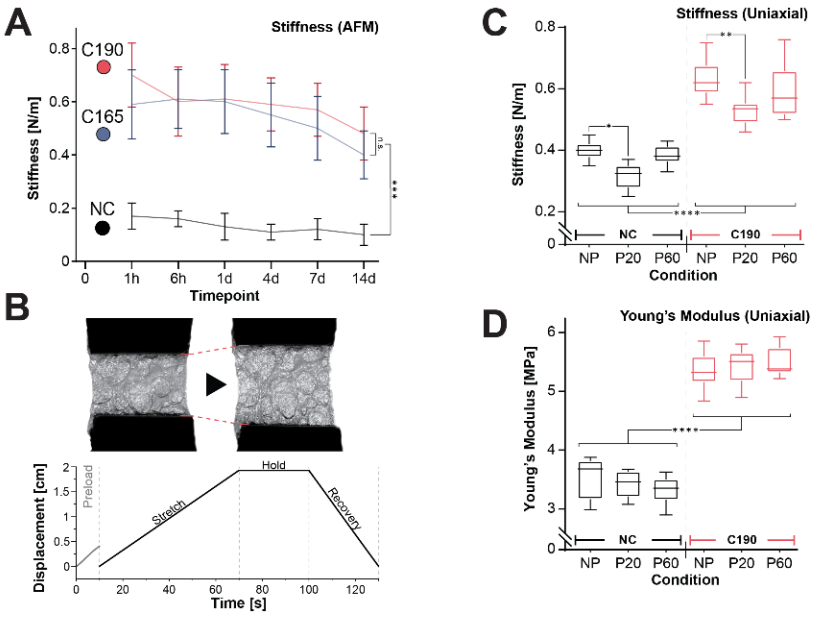

Figure 2.5: Macro- and micro-mechanical characterization of chitosan substrates. (A) Surface stiffness obtained by AFM nano-indentation of as-deposited (NC) and CA crosslinked chitosan treated at 165 °C (C165) and 190 °C (C190). (B) Experimental loading condition (*bottom*) used for uniaxial testing and optical images (*top*) of samples before and after loading. (C) Bulk stiffness and (D) Young's modulus obtained by uniaxial testing of un-patterned (NP) and patterned (P20/P60) chitosan, both as-deposited (NC) and CA crosslinked at 190 °C (C190).

The mechanical reinforcement provided by the crosslinking process was confirmed by the average longitudinal Young's modulus, which increased from 3.2-3.4 MPa for NC to 5.2-5.4 MPa for C190 substrates (**Figure 2.5D**). The observed mechanical strengthening of C190 samples can be attributed to the additional inter-/intra-molecular chain bonds formed during

the crosslinking process, which results in reduced freedom of movement within the 3D chain network.

2.3.5 Evaluation of the cellular response.

To elucidate the cellular response to micropatterned/crosslinked chitosan substrates and to extract the role of individual parameters from the compounded cueing on cell behavior, we employed mouse DRGs and hMSCs. Based on our physicochemical characterization, we decided to only consider the C190 condition for our biological assays.

DRGs. **Figure 2.6A** shows representative fluorescence images for un-patterned controls (NP) and the two patterned conditions tested, in their un-crosslinked (NC) state. It is evident that aligned channels (i.e., P20 and P60) guided cell orientation in a preferential direction when compared to un-patterned controls (i.e., NP), resulting in much more aligned neuronal networks. We subsequently assessed the branching complexity by quantifying the percentages of single, double, triple and quadruple points within the network (**Figure 2.6B**). The percentage of single branches strongly increased in the patterned conditions, particularly in the NC-P20 (~ 20%), when compared to the un-patterned control (~ 6%). In addition, the combined amount of triple and quadruple points accounted for ~ 57% of the total junctions in NC-NP. The respective values decreased to ~43% for NC-P60 and to ~ 29% for NC-P20. While it is evident how the micro-topographies strongly affect the neuronal network complexity, statistical analysis revealed a marginal role of the stiffness as no significant differences between NC and C190 conditions were detected.

In terms of the average branch length (**Figure 2.6C**), NC-P20 showed the highest average value of 230 µm. The average branch length decreased to 114 µm for the NC-P60 and to 42 µm for the NC-NP Each set of values (i.e., NC and C190) associated with the same topography was significantly different from the other patterning conditions. Conversely, no significant

differences were detected between crosslinked and non-crosslinked samples within the same type of surface topography.

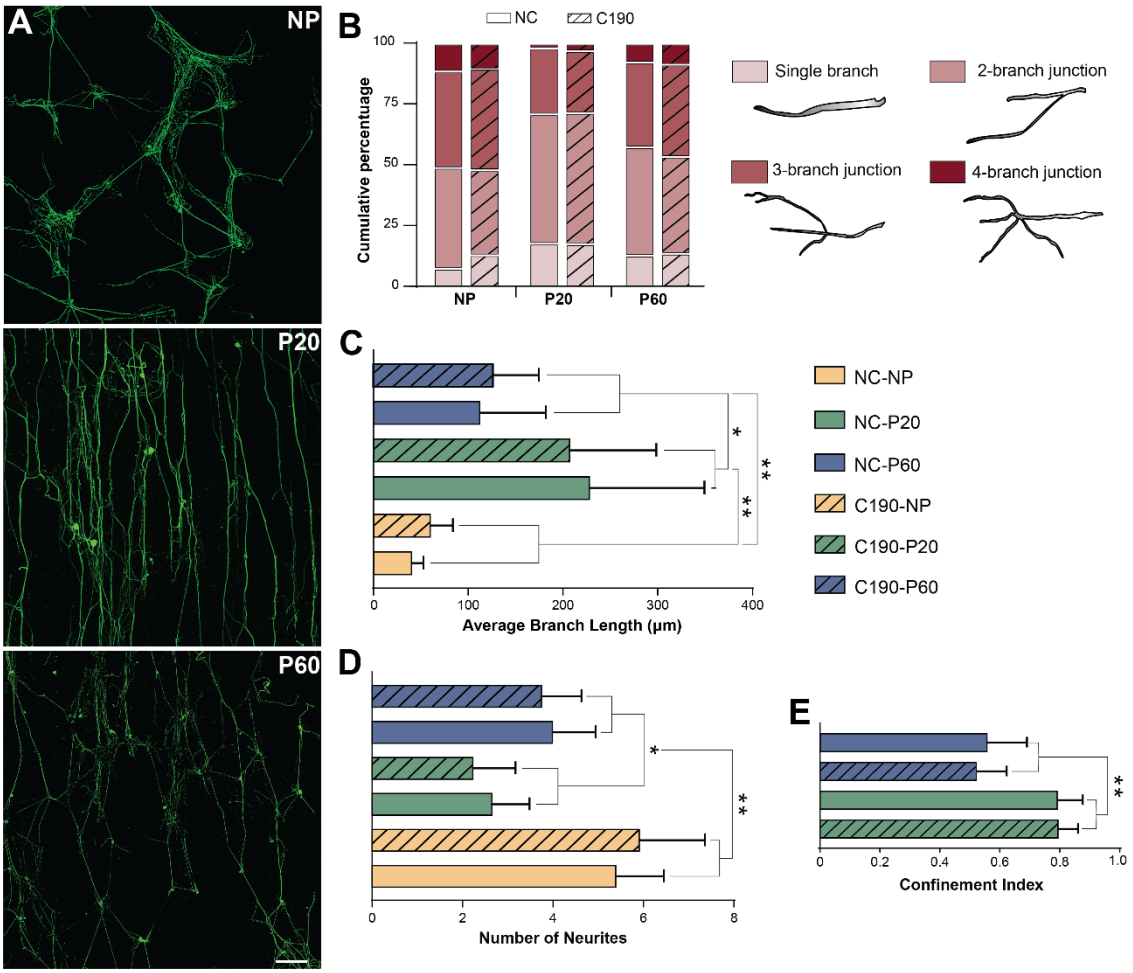

Figure 2.6: DRGs cultured onto chitosan substrates. (A) DRGs adhering onto chitosan substrates with different surface topographies: un-patterned (NP, *top*), arrays of parallel 20 µm-wide channels (P20, *middle*), arrays of parallel 60 µm-wide channels (P60, *bottom*). Scale bar: 200 µm. (B) DRGs network complexity expressed in terms of branching order. Figure legend shows examples of the four types of junctions extracted from fluorescence images. (C) Average branch length. (D) Average number of neurites per soma. (E) Confinement index expressed as the number of channel embedded DRGs over the total number of DRGs.

From a single-cell analysis, we also quantified the number of neurites per soma. As shown in **Figure 2.6D**, neurites per soma were significantly higher in NC conditions when compared to both P60 and P20 samples. These results followed the trend observed for the branching

complexity, as a higher number of neurites per soma is expected to lead to a more complex neuronal network.

Finally, we evaluated the efficiency of the microchannels in restraining neurite outgrowth within their walls. P20 substrates showed an overall confinement ability significantly superior to that found for the P60 conditions (**Figure 2.6E**). The neurite's tendency to cross a wall is influenced not only by the channel depth but also by the ratio wall/channel width. It was reported that a ratio equals to 1 constitutes the most effective configuration at enhancing neurite alignment,[261,262] as confirmed by our results.

Micro-topography: the introduction of topographical cues was shown to strongly affect DRGs behavior. In particular, the narrower geometry (i.e., P20) elicited a reinforced alignment of neurites along the channel's direction and promoted the formation of longer branches from the neuronal soma when compared to the P60 and un-patterned samples. On the other hand, the higher compartmentalization determined a reduction of the number of neurites spreading from the soma and a lower network complexity with rare inter-channel junctions.

Stiffness: despite substrate elasticity's fundamental role in regulating neural processes response,[263–265] DRGs adhering onto treated and un-treated chitosan samples showed similar behaviors within the same topographical condition. We hypothesize that the difference in stiffness between the untreated and crosslinked conditions was not sufficient to elicit a differential DRGs response.

Surface roughness: the key role played by surface roughness in influencing cell-substrate interactions has been widely investigated. Notably, the cell's propensity to adhere on rougher surfaces is well-known.[266] The higher surface roughness detected at the channel/wall interfaces provided preferential sites of adhesion that ultimately determined a higher concentration of neurons in proximity to the wall. Moreover, several studies have demonstrated that the distance between the adhering site and the physical cue strongly determines the alignment degree of the

neurons. In particular, neurons adhering in proximity of the physical cue exhibited a high tendency to spread their neurites following a preferential direction.[267] For this reason, the roughness gradient detected on patterned samples (higher values at the channel/wall interface and lowest at the channel's center) may encourage an optimal alignment of the neurons.

Taken together, our findings demonstrate that the introduction of a highly constraining pattern geometry (i.e., P20) together with a higher surface roughness at the channel/wall interface resulted in highly aligned neurons and more uniform networks characterized by fewer ramifications, lower neurites per soma, and, in most cases, a bipolar neurite outgrowth in which single branches extended from opposite sides of the cell body. These effects likely derive from the limited surrounding space in which neurites can sprout from the soma, as well as from the outgrowth inhibition in directions different from those of the physical cueing.[267,268] Conversely, the DRGs cultured on the control samples showed multipolar neurite outgrowth, resulting in a more complex neuronal network.

In agreement with several studies reported in the literature,[267,269,270] our results demonstrate the ability of the microchannels to increase the overall length of neuronal branches. The P20 condition exhibited the highest branching length and well-comparted networks characterized by poor inter-channel junctions. On the other hand, the P60 condition constituted a valid compromise, exhibiting a higher growth rate than the controls while guaranteeing higher neurites per soma and better inter-channel connections, when compared to P20 substrates.

***hMSC*s**. We evaluated the short-term ability of hMSCs to adhere and proliferate on electrodeposited chitosan samples, with a particular emphasis on the influence of the microchannels in dictating the morphology and orientation of cell bodies and filopodia. **Figure 2.7A** displays hMSCs adhering onto un-patterned controls and patterned samples after 4 days of culturing. It can be readily observed that microchannels play a fundamental role in preferentially orientating cells. While the orientation on the NP surfaces is random, patterned

samples, and namely the condition with the narrowest channel width (P20), guided cell orientation towards a preferential direction. To quantify variations in cell orientation, we measured the offset angle between the cell's principal axis and the channels' longitudinal axis (**Figure 2.7B**) which was then plotted as a relative frequency distributed across 15°-wide angular bins. Rose plots in **Figure 2.7C** illustrate the angular relative frequency at 1 (*top*) and 4 (*bottom*) days relative to both the bodies (*left*) and filopodial protrusions (*right*). On day 1, the P20 conditions showed a relative frequency in either of the first two bins of ~ 0.7. This value decreased to ~ 0.4 for theP60 and P60 conditions. Similar differences were also found in the orientation of the filopodial protrusions. Most protrusions sprouting from the body of cells seeded on NC-P20 and C190-P20 revealed a marked preference to follow the channel's orientation. The cumulative frequency of filopodia characterized by an offset angle lower than 30° was similar for the NC-P20 and C190-P20 conditions (~ 0.7). Conversely, the respective cumulative frequency associated with NC-P60 and C190-P60 samples was ~ 0.3. The results obtained after 4 days confirmed the more efficient alignment determined by the narrower microchannels. Nonetheless, we also detected an overall improvement in the bodies and protrusion orientation toward the channels' direction. In the case of P20 substrates, the relative frequency of bodies aligned within a 15° angle was found to be ~ 0.5, showing a significant 20% increase when compared to 1 day. A similar consideration can also be applied to the P60 conditions. The cumulative frequency of bodies aligned within 30° was ~ 0.6. Regarding the filopodial protrusions, both patterns showed a slight increase in the cumulative frequency in the 30° range compared to day 1. ANOVA analyses revealed the marginal role played by the surface stiffness in dictating the body and filopodia alignment as no significant differences were found between untreated and the respective crosslinked conditions.

As previously demonstrated, cellular morphology constitutes a useful and reliable predictor of hMSCs differentiation that can be greatly altered by surface topography.[271–276] **Figure 2.7D**

shows a transition in the cell morphology, from rounded on NP substrates to more elongated in both the patterned conditions. In particular, the aspect ratios calculated at 1 day for NC-P20 and C190-P20 were respectively ~ 3.2 and ~ 3.1. The aspect ratios for NC-P60 and C190-P60 extracted at the same timepoint significantly dropped to ~ 2.5 and ~ 2.6. All the tested conditions revealed a significant increase in the index within the two timepoints, while keeping a significant difference between the two patterns. For both timepoints, we did not detect any significant differences introduced by the crosslinking process.

Finally, the analysis of the hMSCs spreading area revealed the influence of both pattern's geometry and substrate's stiffness (**Figure 2.7E**). At day 1 our results showed a significant increase of MSCs spreading area seeded on the P60 samples when compared to P20, regardless of the crosslinking condition. Despite lower values found for the crosslinked conditions in both topographies, ANOVA analysis revealed no statistically significant differences *($p>0.05$)*. After 4 days, on top of an overall increase in the MSCs spreading area for all the conditions tested, the trends found for the first timepoint were confirmed. Regarding the P20 topography, despite higher values found in untreated samples, no statistically significant differences were detected. On the other hand, the values found for P60 samples revealed a significant increase in the spreading area in the untreated samples. The reduced cellular area associated with P20 samples likely depends on more marked physical constraints, which induce cells to acquire an elongated shape, as demonstrated by the aspect ratios obtained for this topography. In a less constrained geometry (i.e., P60), our results confirmed the well-known impact of the substrate's stiffness on cell spreading,[274,275] by showing a reduced cellular area in the treated samples.

Micro-topography: as per DRGs, the microchannels strongly affected hMSCs behavior. The P20 conditions (NC-P20 and C190-P20) displayed the highest degree of orientation toward the preferential direction provided by the physical cues. On the other hand, hMSCs adhering to un-patterned samples were randomly oriented. Moreover, our results suggest the primary role

played by the microchannels in directing a morphological transition of hMSCs from a rounded toward a neuronal phenotype characterized by an elongated shape and several filopodia sprouting from the cellular body.

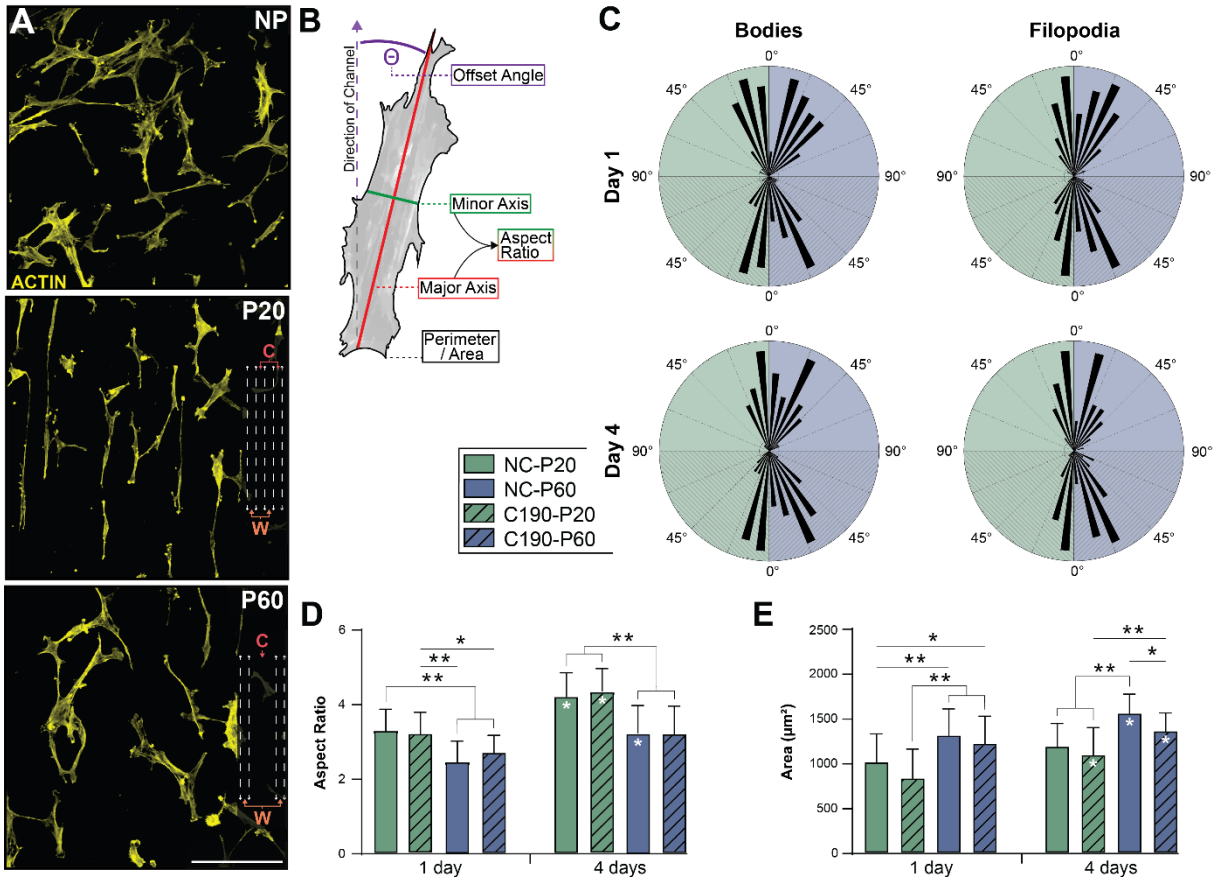

Figure 2.7: hMSCs cultured onto chitosan substrates. (A) hMSCs adhering onto chitosan substrates with different surface topographies: un-patterned (NP, *top*), arrays of parallel 20 µm-wide channels (P20, *middle*), arrays of parallel 60 µm-wide channels (P60, *bottom*). Scale bar: 200 µm. (B) Schematic representation of the parameters calculated. (C) Relative frequency distribution of the angular orientation of cell bodies (*left*) and filopodia (*right*) with respect to the channels' principal direction at 1 (*top*) and 4 days (*bottom*) (D) Average aspect ratio at 1 (*left*) and 4 days (*right*). E) hMSCs average spreading area at 1 (*left*) and 4 days (*right*).

Stiffness: while no significant differences were found in the degree of alignment and in the morphology of hMSCs between the untreated and the respective treated samples, the average spreading area was modulated by the substrate's stiffness. Notably, our results showed a significant increase in the average spreading area on the C190-P60 when compared to the NC-

P60 conditions. Therefore, unlike the case of the DRGs, stiffness differences within the range considered in this study can induce a differential response by hMSCs.

Surface roughness: surface roughness plays a fundamental role in determining hMSCs behavior in terms of adhesion and morphological changes.[277] The channel/wall interface displayed an RMS roughness which favored hMSCs adhesion, ultimately determining an efficient alignment on both the patterned samples. Furthermore, surface roughness also regulates important morphological parameters such as filopodia formation. From **Figure 2.7A**, it is evident that the longest and densest filopodia were observed at the channel/wall interface of patterned substrates and on un-patterned samples, while, at the center of the channels, the length and the amount of filopodia sprouting from the body were significantly reduced.

Our results suggest synergistic effects exerted by the surface topography and roughness in determining a preferential orientation and triggering a gradual morphological transition. hMSCs alignment was determined by the direct guidance provided by the microchannels as well as by surface roughness that offered a preferred adhesion site in proximity to the channel/wall interface. Concerning the morphology, hMSCs seeded onto patterned samples (namely P20) displayed an elongated shape, suggesting a potential early stage of neuronal differentiation. Furthermore, in agreement with different studies reported in the literature, we found a marked influence exerted by the surface roughness in determining the density and the length of filopodia. Finally, while no differential response in terms of alignment and morphology was observed, surface stiffness impacted the spreading area at day 4.

2.3.6 hMSC neurogenic differentiation.

In recent years, the combination of stem cell therapy together with the optimization of biomaterial-based constructs has led to significant advances in neuronal tissue engineering.[278,279] In particular, mesenchymal stem cells undergo neurogenic

transdifferentiation, secrete important neuroregulatory molecules that ultimately promote the regeneration process.[280,281] For this reason, we evaluated the neurogenic potential of chitosan substrates by focusing on the role of topographical and mechanical cueing. We considered both a morphological characterization to track the transition toward a neuron-like phenotype and the expression of βIII-tubulin, the major component of neuronal microtubules which is often used as a neuron-specific marker for positive neuronal identification.[282,283] To offset potential interference in the fluorescence signal, we normalized the intensity of the βIII-tubulin against that of the F-actin cytoskeleton.

As shown in **Figure 2.8A**, hMSCs on micropatterned substrates expressed a significantly higher amount of tubulin (green fluorescence) when compared to un-patterned controls. The tubulin/actin ratio relative to NC-NP was 0.4, and it increased to 1.5 and 1.4 for NC-P20 and NC-P60, respectively, under normal culturing conditions (**Figure 2.8B**). As revealed by the one-way ANOVA analysis, hMSCs seeded onto NC-P20 were characterized by a significantly higher intensity of tubulin when compared to both NC-NP and NC-P60. Interestingly, we noticed a significant increase in tubulin expressed in the un-patterned crosslinked condition (NP-C190), with a ratio of 0.8, which nearly doubled the un-crosslinked condition (NC-NP). Conversely, C190-P20 and C190-P60 showed similar tubulin content with respect to the untreated conditions (i.e., 1.6 and 1.3, respectively). As a comparison, we also carried out cell cultures in DMEM supplemented with bFGF, a growth factor that has been used to induce neurogenic differentiation of stem cells.[284,285] The tubulin content of hMSCs seeded onto NC-NP samples in the presence of bFGF increased by 93% when compared to standard culturing conditions, reaching a tubulin/actin ratio of 0.8. In all the other conditions, the bFGF's presence led to minimal variations, comprised within a 13% range. Despite some studies in literature having reported the hMSCs' spontaneous expression of neural markers,[286] the discrepancies

resulting from different harvesting protocols, isolation methods, cell commercial sources, batch-to-batch variability and culturing conditions, make these findings unspecific.

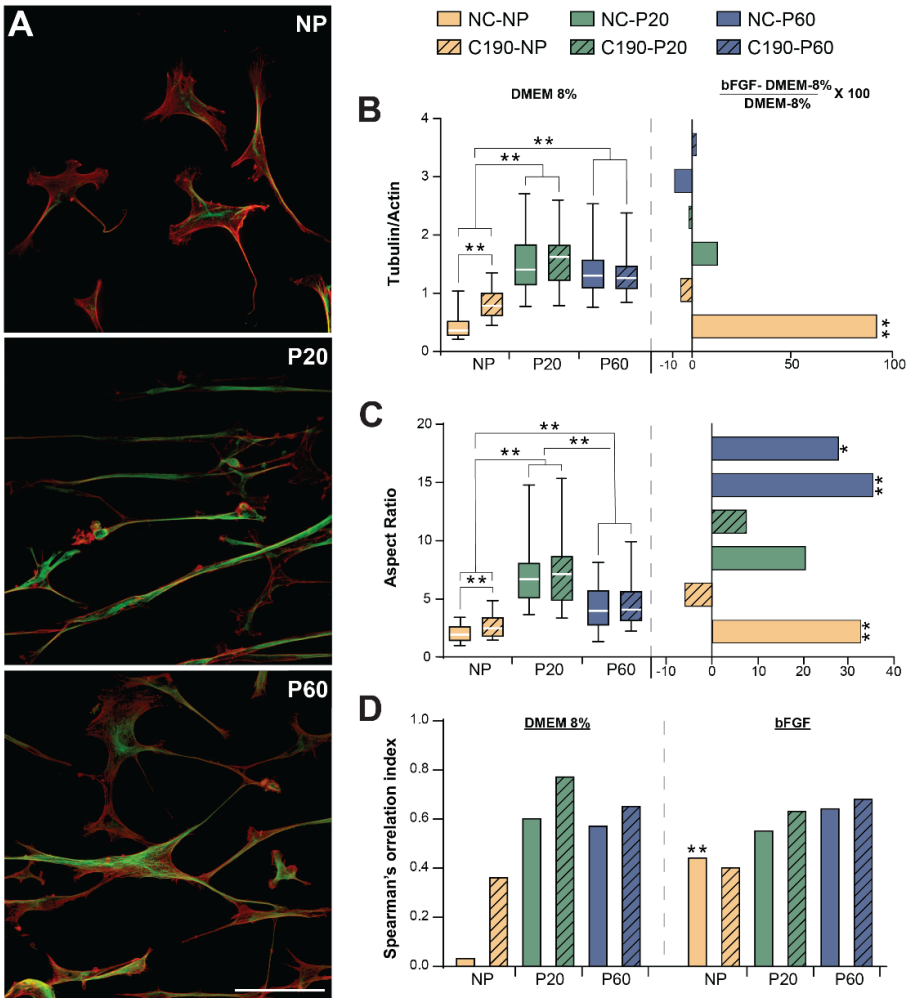

Figure 2.8: hMSCs neurogenic differentiation onto chitosan substrates. (A) βIII-tubulin (green) and f-actin (red) expressed after 3 weeks by hMSCs seeded onto chitosan with different surface topographies: un-patterned (NP), arrays of parallel 20 µm-wide channels (P20), arrays of parallel 60 µm-wide channels (P60). Scale bar: 100 µm (B) tubulin fluorescence intensity normalized against the f-actin content in hMSCs cultured in DMEM 8% (left) and percentage variation of the tubulin/actin ratio between cell cultures with standard (DMEM 8%) and bFGF-supplemented media (right). (C) Aspect ratios of hMSCs cultured in standard condition (DMEM 8%, left) and percentage variations of the aspect ratio between cell cultures with standard (DMEM 8%) and bFGF-supplemented media (*right*). (D) Spearman index for the correlation between βIII-tubulin content and aspect ratio relative to hMSCs cultured in DMEM 8%.

For this reason, we carried out an early evaluation at 24 h as a benchmark to quantify the presence of tubulin in undifferentiated hMSCs at a short-time interval to offset any signal from the native neuronal marker. Our results revealed that less than 1% of hMSCs expressed the

neuronal marker βIII-tubulin (**Figure S2.3E**, **Appendix**), thereby proving the initial undifferentiated state of hMSCs.[287] In addition, to further offset the contribution of βIII-tubulin in undifferentiated hMSCs, we expressed our results in relative terms by comparing changes observed across the different conditions tested. It can thus be postulated that, even if, at later intervals, undifferentiated hMSCs naturally expressed neuronal markers, the physicochemical properties of chitosan substrates induced changes in βIII-tubulin levels.

Moreover, as anticipated by the proven correlation between cell morphology and neurogenic differentiation,[262,265] the quantification of the aspect ratio displayed a trend similar to the one found for the tubulin/actin ratio. Indeed, as shown in **Figure 2.8C**, hMSCs seeded onto NC-NP substrates exhibited the least elongated shape, with an average aspect ratio of 2. In compliance with our previous results found at 1 and 4 days, hMSCs seed onto NC-P20 and NC-P60 presented higher aspect ratio values of 7.1 and 4.2, respectively. On top of an elongated neuron-like phenotype resulting from cytoplasmatic retraction toward the nucleus, the large amount of cytoplasmatic extensions found on hMSCs seed onto patterned samples constitutes further evidence of neuronal transdifferentiation.[288] The active role played by the crosslinking process in promoting neurogenic differentiation was well exhibited by the significant increase in the aspect ratio found for the C190-NP. Conversely, despite slightly higher average aspect ratio values found for both C190-P20 (7.4) and C190-P60 (4.8), no significant differences were detected with their respective untreated conditions. Finally, the comparison with the positive bFGF culturing revealed a marked effect of the soluble factor on the hMSCs morphology. hMSCs cultured onto NC-NP in the supplemented media showed a 37% increase in the average aspect ratio when compared to the corresponding condition in DMEM. Similar considerations were also valid for both the treated and untreated P60 conditions. Finally, we did not notice any significant variations in the hMSCs morphology determined by the bFGF for both NC-P20 (+ 20%) and C190-P20 (+ 7%).

Notably, an interesting relationship emerged whereby more elongated hMSCs expressed relatively higher amounts of tubulin. For this reason, we quantified the correlation between tubulin expression and aspect ratio of cells, by determining the non-parametric Spearman index (**Figure 2.8D**). NC-P20 and NC-P60 samples showed a moderate positive correlation (i.e., Spearman index of ~ 0.60). Among all conditions tested, the Spearman index was close to 0 only for cells adhering to the NC-NP substrates, thereby revealing the independence between the two parameters. Our findings suggest that crosslinked substrates enhanced the positive correlation between tubulin expression and morphology. Indeed, C190-NP displayed a weak correlation between the two parameters with a Spearman index of 0.40. The effect of the crosslinking process was also appreciable in both the patterned conditions. C190-P60 exhibited a Spearman index of 0.66 which delineates a moderate-strong positive correlation. Finally, we found a Spearman index of 0.78 for C190-P20, revealing the strongest correlation between the two parameters. **Figure 2.8D** also reports the Spearman indexes found for all the conditions when the culturing was carried out in bFGF-supplemented media. It is evident the significant increase found for the NC-NP condition that displayed a weak correlation characterized by a Spearman index of 0.45. For all the other conditions, the corresponding conditions cultured in the two different media gave rise to the same magnitude of the correlation between tubulin amount and aspect ratio.

Our results demonstrate the ability of engineered chitosan guides to not only align and direct morphological transformations in hMSCs as previously shown, but also to support their neurogenic differentiation by (*i*) constraining effects exerted by the channels and direct (*ii*) physical cueing exerted by the substrate's stiffness and chitosan or, more likely, by the synergistic combination of these factors.

Micro-topography: the surface patterns are expected to direct a marked morphological transition from a spindle-like to a more elongated neuron-like shape, with a higher amount of

cytoplasmatic processes emerging from the cellular body. This was observed in hMSCs adhering to both P20 and P60 substrates, which expressed a higher content of βIII-tubulin when compared to un-patterned controls. Within the non-crosslinked conditions, hMSCs seeded onto NC-P20 displayed the highest aspect ratio and tubulin expression in normal culturing conditions, with no statistically significant differences when compared to bFGF positive controls. Conversely, for the NC-P60 condition, while the culturing conditions did not affect the expression of tubulin as for the NC-P20, bFGF determined a significant increase in the aspect ratio, leading to a more accentuated neuronal phenotype. We demonstrate that the introduction of topographical cues, as well as channel width, greatly impacts the cytoskeletal composition of hMSCs. Both patterned conditions displayed stem cells expressing higher tubulin amounts when compared to the un-patterned condition. Nonetheless, our results suggest that narrower geometries could fasten the neurogenic differentiation, as the highest amount of tubulin was expressed by hMSCs seed onto P20 samples.

Surface stiffness. Previous works have shown that neurogenic differentiation is privileged on softer materials.[289,290] However, most studies have been comparing the responses elicited by hydrogels that are considerably softer than the chitosan samples employed in this study. Our findings revealed the more marked effects exerted by stiffer substrates in promoting the neuronal differentiation of hMSCs. In fact, C190-NP expressed a significantly higher value of β-tubulin when compared to the untreated condition. This confirms the role of physical cueing in directing the differentiation of mesenchymal stem cells towards a specific lineage by matching the substrate's stiffness to that of the target tissue.[291]

Surface roughness: different roughness values have been employed to direct hMSCs differentiation toward specific lineages.[292–294] In this work, both un-patterned conditions, which displayed the lowest amount of tubulin expression, were characterized by highly heterogeneous surfaces (i.e., roughness standard deviations of 52 nm for NC-NP and 59 nm for

C190-NP). On the other hand, all the patterned samples, despite the heterogeneous morphological characteristic found in the different (i.e., highest roughness values at the channel/wall interfaces and lowest at the channel centers), displayed an intra-region uniformity with roughness standard deviation within 35 nm. We thus believe that the improved morphological uniformity on the patterned samples is likely a key factor to favor the neuronal differentiation of hMSCs.

Surface chemistry and degradation products: previous work showed the key role exerted on cell morphology and proliferation using citric acid as a supplement in the culturing media. Also, it has been reported that environmental acidity greatly mediates enzyme activity and cellular biochemical reactions thus potentially directing cellular differentiation. [295] However, the results obtained from our ATR-FTIR analysis of the degradation products of C190 samples revealed that the citric acid molecules released during degradation are covalently bound to the chitosan chains, which indicates the absence of free acid molecules in solution. In addition, the similar acidity found in the solutions containing NC and C190 degradation products, aside from confirming the absence of ionized citric acid molecules, also rules out the pH as a key contributing factor in guiding the neurogenic differentiation of hMSCs. We can thus conclude that potential environmental effects on stem cell differentiation can be excluded, thereby proving that direct cueing from the substrate is what controls the differentiation.

Taken together, our results suggest the primary role of the surface topography in determining a neuronal phenotype as well as a high expression of β-tubulin. In fact, regardless of the geometry (P20/P60) and the crosslinking degree (NC/C190), hMSCs seeded onto the patterned samples showed significantly higher amounts of tubulin and higher aspect ratios when compared to both the un-patterned conditions. The differential output elicited by the substrate's stiffness was appreciable solely on the un-patterned samples with hMSCs, displaying a significantly higher expression of the neuronal marker when seeded onto the

treated and stiffer samples. However, such a beneficial effect provided by the CA-based crosslinking was trumped by the introduction of microchannels. In fact, within the same pattern condition, treated and untreated samples elicit a similar output in terms of tubulin expression and morphology thus reaffirming the pivotal role of surface topography. Finally, we hypothesize that the intra-region roughness uniformity found on the patterned samples (i.e., channel/wall interface and channel's center) was a key factor that ultimately determines an enforced neuronal differentiation of hMSCs.

2.4 CONCLUSIONS

In this study, we fabricated chitosan substrates with parallel microchannels and successively crosslinked with a CA-based method to investigate the compounded effects of physiochemical parameters on the response of DRGs and hMSCs. Our cellular studies reaffirmed the role of surface microtopography, roughness and stiffness in directing cellular functions, and how these variables can be modulated to exert differential cueing on adhering cells. While the substrate's stiffness predominantly affected hMSC spreading, the modulation of the channels' design directed the neuronal architecture's complexity, the branching length, as well as the orientation efficiency of the neurites, while guiding the morphological transition of hMSCs from a spindle to an elongated neuron-like shape. Finally, the combined analysis of tubulin expression and cell morphology allowed us to cast new light on the synergy between microchannels and CA-crosslinking in the process of hMSCs neurogenic differentiation. In conclusion, our study hence provides new evidence regarding the interfacial interactions of DRGs and hMSCs with micro-engineered chitosan surfaces, highlighting the role of selected physicochemical parameters. These are important aspects in the development of better-performing material-based approaches for *in vitro* studies as well as for more effective solutions for clinical neuronal tissue engineering applications.

CHAPTER 3: Electroconductive Collagen-Carbon Nanodots nanocomposite elicits robust neurite outgrow, supports neurogenic differentiation and accelerates electrophysiological maturation of iPSCs in neural progenitor spheroids

3.1 INTRODUCTION

Neuronal disorders, including neurodegenerative conditions such as Alzheimer's and Parkinson's disease, as well as traumatic injuries and stroke, are associated with neuronal loss and/or the deterioration of neuroanatomical connectivity, severely affecting the quality of life of patients. The first attempts to regenerate lost neuronal functions date back to the 1970s and explored the transplantation of primary dopaminergic (DA) neurons sourced from human embryos.[296–298] However, inconsistent protocols, excessive dopamine transmission, low availability of fetal tissues and ethical concerns hindered their clinical success,[299] inspiring researchers to turn to emerging alternatives for scalable and traceable sources, such as embryonic stem cells (ESCs) and induced pluripotent stem cells (iPSCs). The well-established protocols and the efficacy in preclinical models have made stem cells an excellent candidate for cell-based therapies,[297] but low (5-10%) survival rates, inadequate differentiation into the desired phenotype and adverse host immune responses, have negatively affected the therapeutic outcome.[296–299] To address these limitations, researchers have turned to original approaches that synergistically integrate concepts of stem cell regenerative medicine with biomaterial-based neural tissue engineering.[300,301] One of the fundamental design criteria for effective clinical translation emphasizes the use of biomaterials that recapitulate key physicochemical features of the intended target tissue to recreate a biomimetic microenvironment that ultimately enhances cell survival, guides differentiation and promotes functional integration within the host tissue. Among the material properties deemed fundamental to achieve neuro-regenerative abilities (e.g. biocompatibility, native tissue-like mechanical properties, and proper degradation rate),[6,300,301] recent findings have highlighted

the pivotal role of electroconductivity in guiding several developmental processes associated with cell proliferation and synaptic plasticity.[302,303] Based on this evidence, the use of electroconductive hydrogels has emerged as an effective approach to recapitulate the physicochemical and electrical microenvironment of neural tissues.[304,305] In fact, while widely used hydrogels (e.g. collagen, alginate, and gelatin) offer a cell-instructive microenvironment that mimics the physicochemical properties of native extracellular matrix (ECM) to enhance the adhesion, growth and differentiation of neuronal cell populations, they are characterized by a low electrical conductivity.[306,307] One of the most investigated strategies to integrate this additional functionality is the incorporation of metal- or carbon-based nanomaterials.[307–311] In this context, nanocomposites consisting of nanomaterials such as carbon nanotubes (CNTs) and graphene nanoparticles dispersed within a hydrogel matrix have been shown to promote highly desirable cellular effects, such as neuronal differentiation, axonal elongation and network formation. In particular, the exceptional electrical conductivity of CNTs and their capacity to integrate with the extracellular matrix led to enhanced electrical signaling among neurons, which is vital for the formation of functional neural networks.[312,313] Likewise, nanomaterials including graphene oxide and reduced graphene oxide offer a conducive environment for cell adhesion and neurite expansion, in addition to modulating the expression of neuronal markers.[314,315] Notably, the extensive body of literature which investigated the potential of these candidate electroconductive nanocomposites for neuro-regeneration, mostly employed simplified experimental conditions (e.g., conventional monolayer) that do not recapitulate the native ECM and/or adopted primary immortalized cells (i.e., PC12 and SH-SY5Y) that do not replicate the cellular phenotype of mature differentiated neurons, ultimately widening the gap between *in vitro* research and the *in vivo* reality.[316–318] In fact, it is well known that for central nervous system neurons, the two-dimensional cellular microenvironment associated with conventional cell monolayer cultures leads to aberrant cell–cell contacts and

network formation, unrealistically flattens soma and growth cones and limits axon-dendrite outgrowth.[319,320] Similarly, culture systems that employ dissociated immortalized cells do not fully capture the physiological complexity (i.e., cell-cell and cell-extracellular matrix interactions) and the cellular architecture of the native nervous tissue.[321,322] Taken together, these observations reaffirm the importance of the selection of a physiologically accurate *in vitro* testing platform and relevant cell models, as an important early step for the development of novel neuro-regenerative biomaterials and the investigation of their therapeutic potential.

In this context, we have developed a novel electroconductive nanocomposite consisting of a collagen type I matrix functionalized with carbon nanodots fabricated from glycine precursors (GlyCNDs). The rationale behind this novel strategy is that collagen has already shown great promise as a therapeutic solution for central nervous system injuries and degeneration.[6,135,141,143,144] When used in its hydrogel form, collagen provides unique physicochemical and biological cues that support cellular adhesion, growth and proliferation. It is also a biopolymer approved by the FDA for clinical testing in neural tissue engineering and several collagen-based products are already commercially available[6] However, collagen's fast degradation rate in physiological conditions represents a factor that cannot be overlooked. In addition, native collagen cannot recapitulate the electroactive environment of native nervous tissue. In parallel, the choice of CNDs, a relatively new type of carbon-based nanoparticles (1-10 nm in diameter), is supported by the fact that they offer diverse physicochemical properties and advantageous characteristics such as biocompatibility, low cytotoxicity, ease of synthesis, abundant functional groups (e.g., amino, hydroxyl, carboxyl) and high physicochemical stability.[323,324] CNDs can be synthesized from a wide variety of carbon-containing precursors all of which dictate the resultant surface functional groups. Because they are a relatively new class of nanoparticles, the potential of CNDs in the context of neural tissue engineering is only beginning to be explored.

In this work, we synthesize and carry out a comprehensive physicochemical characterization of the collagen-GlyCND nanocomposite and evaluate its biological impact by employing both mouse-induced pluripotent stem cells (iPSCs) -derived neural progenitor (NP) spheroids (and 3D cultures of primary cortical neurons as a confirmatory cell model), specifically selected to recreate a more realistic cellular microenvironment that recapitulates that of native tissues. Spheroids (hereafter also referred to as neurospheres) offer several advantages over conventional *in vitro* systems, making them a more physiologically relevant model for studying neural tissue engineering. Firstly, spheroids mimic the three-dimensional (3D) architecture of the ECM, thereby enabling more accurate cell-cell and cell-ECM interactions, which are essential to investigate cellular behavior and functions.[325] Secondly, spheroid cultures better recapitulate the spatial organization and cellular heterogeneity of native tissues, providing a more realistic environment for studying neuronal differentiation and network formation. [325,326] Additionally, spheroids exhibit improved nutrient and oxygen gradients, closely resembling *in vivo* conditions.[327]

From a morphological point of view, significantly more neurite sprouting occurs in both spheroids and primary neurons when compared to collagen and collagen with suspended GlyCNDs, showing a significantly higher branching tendency. In addition, the GlyCNDs positively enhance additional functions, such as neuronal differentiation and electrophysiological maturation. In particular, the significantly lower number of cells positive for Ki-67, a nuclear proliferation marker, and the lower expression of nestin (proliferating neural precursor marker) coupled with higher expression of both β-III-tubulin and MAP2 (early and mature neuronal marker), suggests that the nanocomposite accelerates neurodifferentiation of NP spheroids without exogenous factors. Moreover, the electrical activity displayed by the neural spheroids, as determined by multi-electrode arrays (MEA) measurements, was significantly higher when they were embedded in the nanocomposite (vs in collagen and in

collagen with suspended GlyCNDs) in terms of both single electrode and network activity. Interestingly, only the electrophysiological activity of spheroids in the nanocomposite was significantly more sensitive to NMDAR compared to AMPAR blockers, thereby indicating an interplay between the NMDA-dependent network and the immobilized GlyCNDs.

3.2 MATERIALS AND METHODS

3.2.1 Nanocomposite hydrogels preparation

Collagen hydrogels were prepared by dilution of rat tail type I stock (Corning, USA, 9.38 mg/ml, #354249) in differentiation medium (DM) and PBS 10X to reach a final concentration of 2 mg/ml. The medium recipe is outlined in "*Derivation and culture of iPSCs-derived NP spheroids*" section. GlyCNDs were introduced in the collagen solution either in their pristine or activated state. For the latter, GlyCNDs were immersed in MES buffer (pH=6.0) containing (1-Ethyl-3-[3-dimethylaminopropyl]carbodiimide hydrochloride) (EDC) and N-hydroxysuccinimide (NHS) (ratio 2:1) for 1 h at 4 °C. The mass ratio between the GlyCNDs and EDC was fixed at 1:1. Upon the introduction of the GlyCNDs, the pH of the collagen solution was neutralized through the addition of 1N NaOH. The collagen hydrogels were then incubated at 37 °C to allow complete polymerization. Three GlyCNDs concentrations were tested (for both pristine and activated GlyCNDs states) based on cytotoxic data available for other carbon-based nanoparticles in the literature (**Table 1**).[328–330]

Table 3.1: GlyCND concentrations tested in this study.

Pristine GlyCNDs		
Abbreviation	EDC/NHS [mM]	GlyCNDs [mg/mL]
C_CND05	/	0.5
C_CND1	/	1.0
C_CND4	/	4.0
Activated GlyCNDs		
CE_CND05	2.5	0.5
CE_CND1	5.0	1.0
CE_CND4	20.0	4.0

3.2.2 Atomic force microscopy (AFM)

The spatial distribution of the GlyCNDs within the collagen matrix was revealed by using non-contact AFM on am Alpha300 RSA system (WITec, Germany). Surfaces (1 x 1 μm^2) were scanned using the triangular Si_3N_4 Cantilevers of the DNP-S10 chip (Bruker, USA), characterized by a nominal spring constant of 0.2 N m^{-1}, a resonant frequency of 13 kHz and nominal tip radius of 10 nm. 3D micrographs were then processed in Gwyddion[246] to extract depth profile and GlyCNDs's diameter.

3.2.3 XPS characterization

GlyCNDs were analyzed using XPS with a K-Alpha X-ray photoelectron spectrometer (Thermo Scientific, USA). Three randomly selected regions of the sample were analyzed in triplicate, with each scan consisting of 10 runs. The results were averaged and plotted for both the survey and the high-resolution scans.

3.2.4 Raman spectroscopy

Single spectra for each experimental condition were acquired with the Raman module of the Alpha300 RSA system. Spectra were collected through a 50X objective (EC Epiplan NEOFLUAR, N.A.=0.9, Zeiss) with an excitation wavelength of 524 nm provided by a doubled Nd:YAG laser (12.5 mW, acquisition time of 2 s). Baseline subtraction, data normalization and Voigt (Lorentzian/Gaussian) deconvolution for the identification of vibrational components were performed in OriginPro (OriginLabs, USA). The bands related to C-N stretching of both the Amide III (1271 cm^{-1}) and Amide II (1558 cm^{-1}) groups were used to confirm the immobilization of the GlyCNDs into the collagen matrix.[331–333] The 1098 cm^{-1} band, associated to the N-C-H deformation of the collagen proline ring, [334] was used as the reference peak for the normalization and comparison of spectra across conditions.

3.2.5 Conductivity measurements

A conductivity meter (CON 110 Conductivity/TDS Meters, Oakton® Instruments, USA) was used to assess the electrical conductivity of the collagen matrices used in this work, with a variable GlyCND concentration, namely 0.5, 1.0 and 4.0 mg/ml. The matrices were incubated at 37 °C for 2 h to allow for complete polymerization prior to the conductivity measurements. Three samples per concentration were analyzed and compared to the control condition represented by EDC-crosslinked collagen.

3.2.6 Degradation studies

The structural stability of the collagen matrices with variable GlyCND concentration was evaluated by carrying out both hydrolytic and enzymatic degradation studies. For the latter, the degradation solution consisted of collagenase type IV from *Clostridium histolyticum* (305 U/mg, # LS004188, Worthington Biochemical Corporation, USA) dissolved in phosphate-buffered saline solution (PBS 1X) containing 2 mM $CaCl_2$ at a concentration of 10 U/ml. In both studies, 400 µl of degradation solution (PBS 1X for hydrolytic) was added to 250 µl of the matrix. At specific timepoints, the supernatant was collected, and the collagen concentration was estimated following the microplate procedure of the colorimetric BCA assay (Pierce™ BCA Protein Assay Kit, # 23225, Thermo Fisher Scientific, USA) and calibration curves, obtained collagen standards (0-500 µg range) diluted in both degradation solutions. The percentage of the nanocomposites' mass loss was calculated at any selected timepoint by subtracting the collagen mass in the supernatant from the initial one (i.e., 500 µg).

3.2.7 Derivation and culture of iPSCs-derived NP spheroids

Commercially available mouse iPSCs (Alstem, iPS02m) were propagated in feeder-free conditions on gelatin-coated culture surfaces. Cultures were periodically tested for

mycoplasma with Lookout mycoplasma PCR detection kit (Sigma Aldrich, MP0035). iPSC maintenance medium was composed of KnockOut DMEM (Gibco, 10829018) supplemented with 15% knockout serum replacement (Gibco, N10828028), 1% MEM non-essential amino acid solution (Stemcell, 07600), 200 µM L-glutamine (Gibco, 25030), 1% penicillin-streptomycin (Gibco, 15070063), 100 µM 2-mercaptoethanol (Gibco, 31350) and 1000 U/ml leukemia inhibitory factor (LIF). Embryoid body (EB) formation was initiated by detaching iPSCs from culture surfaces using TryplE (Gibco, 12604013) and re-suspending in fresh iPSC maintenance medium without LIF. Cell suspensions were transferred to Aggrewell 800 plates (Stemcell, 34811) treated with anti-adherence rinsing solution (Stemcell, 07010) and embryoid bodies were allowed to form overnight. Finally, EBs were transferred to anti-adherence treated 6 well plate. After 72 h, the media was switched to neuronal expansion (EM) consisting of 1:1 mixture of DMEM/F12 and Neurobasal medium (Gibco, #21103049) supplemented with 1% GlutaMAX, 1% pen/strep, 1% B-27™ Plus Supplement (Gibco, #A3582801), 0.5% N-2 Supplement (Gibco, #17502001), 200 µM ascorbic acid (Sigma Aldrich, #AX1775) and the following inhibitors: 5 µM SB-525334 (Tocris, 3211), 250 nM dorsomorphin (Tocris, 3093), 3µM Wnt agonist CHIR99021 (Millipore, SML1046). After 10 days, the neurospheres expanded and formed spheroids. Prior to usage, the spheroids were passages 3X with TrypLE (ThermoFisher, #12604013).

The resulting spheroids were embedded in the collagen matrices and culture for 4 days in differentiation medium (DM), consisting of EM without the inhibitors. The media was successively switched to maturation media (MM) consisting of DM supplemented with 100 µM brain-derived neurotrophic factor (BDNF, Stemcell Technologies, #78005), 100 µM glial-derived neurotrophic factor (GDNF, Stemcell Technologies, #78058) and dybutyryl-cAMP (db-cAMP, Stemcell Technologies, #73882). During the spheroids culture, the maturation medium was refreshed every 3 days.

3.2.8 Cytotoxicity assays

To evaluate potential cytotoxic effects associated to both immobilized and medium-suspended GlyCNDs, the level of lactate dehydrogenase (LDH) was measured using CytoTox 96® Non-Radioactive (Promega, USA, G1780) assay. Briefly, 50 µl aliquots were collected from the culture media at 6 and 72 h and then transfer to a 96 well plate. Subsequently, 50 µl of the Citotox96 reagent were added to each sample aliquot. The plate was then covered with tin foil and incubated for 30 min at room temperature. Finally, 50 µl of the stop solution were added to each well and the absorbance band at 492 nm was collected using a Sinergy H1 plate reader (BioTech® Instruments, USA). The percent of cytotoxicity was calculated as:

$$Percent\ cytotoxicity = \frac{Experimental\ LDH\ release\ (OD_{490})}{Maximum\ LDH\ release\ (OD_{490})} \times 100$$

where the Maximum LDH release was obtained by adding 10 uL of 10X Lysis solution to a negative control sample, 1 h before adding the Cytotox96a Reagent.

In addition, at 3 DIV, the samples were stained with PI (ThermoFisher, #BMS500PI) and Hoechst 33342 (ThermoFisher, R37605) and visualized under an LSM880 AxioObserverZ1 confocal microscope (Zeiss, Germany) with a Plan-Apochromat 20X objective (NA = 0.8, Zeiss). The resulting images were processed on ImageJ to quantify the number of PI-positive (PI+) nuclei that was used as a measure of cell death.

According to the results obtained from the cytotoxicity assays, the 1mg/ml concentration of GlyCNDs was selected (labelled CE_CND1) for all the subsequent cellular studies. This condition was compared with the control condition consisting of pristine collagen crosslinked with EDC/NHS (CE). Notably, we added an additional condition (labelled CE_CND1_s) in which the spheroids were embedded in a CE matrix, supplemented with GlyCNDs dispersed in the medium to simulate the release profile previously quantified for the CE_CND1 condition. In this way, we were able to isolate the effect provided by both immobilized (CE_CND1) and dispersed unbound GlyCNDs released by the matrix (CE_CND1_s).

3.2.9 Immunohistochemistry (IHC) staining

At 14 DIV, the spheroids were fixed in fresh 4% paraformaldehyde (PFA) at room temperature for 2 h. Fixed samples were permeabilized with 0.25% Triton-X100 (Sigma-Aldrich, #11332481001) and blocked with 5% horse serum (ThermoFisher, #31874) overnight at 4 °C. Samples were successively incubated with primary antibodies for 24 h at 4 °C, rinsed for a minimum of 10 times with blocking buffer, and lastly incubated overnight at 4 °C with donkey secondary antibodies. The details and working dilutions of primary and secondary antibodies are listed in **Table 3.2**. After 5 rinses, the nuclei were stained with 4-6-diamidino-2-phenylindole-dihydrochloride (DAPI) for 4 h at room temperature.

Protein visualization

Spheroids were imaged on LSM880 AxioObserverZ1 confocal microscope through a Plan-Apochromat 20X objective (NA = 0.8, Zeiss). The multi-channel z-stack images were successively processed in FIJI for background subtraction and the generation of a maximum projection.[76]

Table 3.2: List of primary and secondary antibodies, with their working dilution, used in this study.

Primary antibody	Dilution	Secondary antibody	Dilution
β III-tubulin (Abcam, ab78078)	1:1000	anti-goat Alexa 488	1:500
MAP2 (ThermoFisher, PA5-17646)	1:500	anti-rat Alexa 555	1:500
Ki-67 (ThermoFisher, 14-569)	1:250	anti-mouse Alexa 594	1:500
Synapsin (Phosphosolution, 1927-SYNP)	1:500	anti-rabbit Alexa 647	1:500
NMDAR2D extracellular (ThermoFisher, PA577425)	1:200		
Nestin (Abcam, ab105389)	1:500		
Calretinin (Abcam, ab92341)	1:500		

Morphological analysis

Spheroids were imaged on an LSM880 AxioObserverZ1 confocal microscope (Zeiss, Germany) with a 10X EC Plan-Neofluar (Ph1) objective (NA = 0.3, Zeiss). To evaluate neurite branching complexity and ramification, a semi-automated Sholl analysis centered around the spheroid body with a 20 µm-step between consecutive hemispheres was performed on ImageJ

(Neurite Tracer plugin).[335] The coefficient (Sholl's decay index) of the linear regression model was used as a measure of the rate of decay of the number of branches with distance from the center of analysis. As a measure of branch ramification, Schoenen index (i.e., maximum number of intersections divided by the number of primary branches) was used. In addition, a semi-automated Strahler analysis was performed to extract the mean branch length.

3.2.10 Western blotting

Spheroids cultured in CE, CE_rCND1 and CE_CND1 were harvested into cold RIPA buffer by scraping and sonication of the collagen matrix. The total protein concentration of the cell lysates was determined by BCA assay (Pierce™ BCA Protein Assay Kit, # 23225, ThermoFisher). The lysates were successively boiled for 10 min at 95 °C in the sample loading buffer. The proteins were electrophoretically resolved on a 10% SDS-PAGE gel at 100 V. Resolved proteins were transferred to PVDF membranes for 30 min at 20 V using Transblot Turbo (BioRad, USA). After washing, the membranes were blocked in 5% BSA for 1 h at room temperature. Subsequently, the PVDF membrane were blotted with primary antibodies overnight at 4 °C, washed 5 times with TBST buffer and incubated 2h at room temperature with peroxidase-conjugated secondary antibodies. After washing, the membranes were imaged by a ChemiDoc XRS+ (BioRad) system and the bands were analyzed with the ImageJ software. Primary antibodies targeting the following proteins were used: β III-tubulin (ab78078), MAP2 (PA5-17646), synapsin (1927-SYNP), GAP43 (ab16053), NMDAR2D (PA577425).

3.2.11 Multi-electrode arrays (MEA) readings

The spheroids were cultured on Cytoview MEA 48-well plates (Axion BioSystem, USA, M768-tMEA-48B-5), after pre-coating with poly-L-lysine and laminin. Baseline recording of spontaneous activity were performed in a Maestro MEA system and AxIS software (Axion

Biosystems) by using a bandwidth with a filter for 10 Hz to 2.5 kHz cut-off frequencies. Spikes were detected by using an adaptive threshold set to 6 times the standard deviation of the estimated noise on each electrode. Each plate rested for 1 min for acclimatization in the Maestro instrument and was then recorded for an additional 2 min. The electrophysiological data analysis was performed using the Axion Biosystems Neural Metrics Tool. Bursts were identified in the data recorded from each individual electrode using an adaptive Poisson surprise algorithm. Network bursts were identified for each well using a non-adaptive algorithm requiring a minimum of 40 spikes and of 25% of active electrodes with a maximum inter-spike interval of 100 ms.

Based on baseline recording at 14 DIV, the most active wells electrodes ($>$0.1 spikes/sec) were selected for treatment with either dizocilpine (MK-801 maleate) or 2,3-dihydroxy-6-nitro-7-sulfamoyl-benzo(f)quinoxaline (NBQX). Briefly, the medium of the selected wells was complemented with either 0.1 M MQ-801 or 0.1 M NBQX. After 30 minutes of incubation, spontaneous neuronal activity was measured for 2 min to identify the effect of the specific blocker. After recordings, the samples were washed 5X with PBS 1X and fresh medium was added. The same procedure was followed for the

treatment at 28 DIV. For each experimental condition, a total of 3 independent experiments were performed using a minimum of 9 wells per plate.

3.2.12 Culture and imaging of mouse primary cortical neurons

Primary cortical neurons from QBM Cell Science (Canada, #171003) were suspended in Neurobasal medium complemented with 1% GlutaMAX, 1% pen/strep, 1% B-27™ Plus Supplement, and 0.5% N-2 Supplement. To incorporate the cells into the hydrogels, the cell suspension and hydrogel solution were mixed in a 1:1 ratio, achieving a final cell density of 5.0 x 10^6 cells/ml and a final collagen concentration of 2 mg/ml. The cell-hydrogel mixture

was then pipetted into glass bottom 96-well plates (Greiner Bio-One, #655892, USA) and incubated at 37 °C for 30 minutes to allow gelation. Successively, 200 µl of complete culture medium was added to each well. The hydrogels were maintained in culture for up to 7 days with media changes performed every 2 days. At 7 DIV, the samples were fixed in fresh 4% PFA at room temperature for 2 h. Fixed samples were permeabilized with 0.25% Triton-X100 and blocked with 5% horse serum (ThermoFisher, #31874) overnight at 4 °C. Finally, the samples were stained for β III- tubulin and MAP2 and imaged on LSM880 AxioObserverZ1 confocal microscope through a Plan-Apochromat 20X objective (NA = 0.8, Zeiss). The multi-channel z-stack images were successively processed in FIJI for background subtraction and the generation of a maximum projection.

3.2.13 Data analysis

Data are reported as mean ± standard deviation (SD) or standard error of the mean (SEM) from at least 3 separate experiments. Data were plotted with GraphPad software, version 8.0. The normality of the distribution was assayed by different tests, such as Pearson normality test and Shapiro-Wilk normality test. For normally distributed data, one-way, two-way analysis of variance (ANOVA) test followed by Tukey's Honestly Significant Difference (HSD) post hoc test was used. For non-normally distributed data, Kolmogorov–Smirnov test analyses was carried out. Significance was set at $p \leq 0.05$.

3.3 RESULTS AND DISCUSSION

3.3.1 Characterization of the nanocomposite

The detailed fabrication process and physicochemical characterization of the GlyCNDs have been previously reported by Naccache and co-authors.[336] Here, we carried out a complementary high-resolution X-ray photoelectron spectroscopy (XPS) analysis (**Figure S3.1A, Appendix**)

to confirm the nature of the surface functional sites on the GlyCNDs. Upon deconvolution of the O1s peak (**Figure 3.1A**), we observed a substantial presence of COOH functional groups (531.87 eV), expected to create amide bonds as a result of their interactions with the free amines (NH_2) along the collagen chain.[337] To test the resulting binding affinity, we incorporated the GlyCNDs in a collagen suspension at a concentration of 1 mg/ml both in their pristine state (hereafter referred to as C_CND1) and upon EDC/NHS activation (hereafter referred to as CE_CND1) and compared them to collagen crosslinked with EDC/NHS. The degree of immobilization was evaluated by Raman spectroscopy. **Figure 3.1B** displays the representative Raman spectra for CE, C_CND1 and CE_CND1. A greater presence of GlyCNDs in CE_CND1 is attested by the appearance of a wide fluorescence band spanning from ~1800 to 3600 cm^{-1} that is characteristic of the nanoparticles (see Raman spectra of GlyCNDs in **Figure 3.1B-insert**). Furthermore, the formation of new C-N bonds between the COOH groups of GlyCNDs and NH_2 groups of collagen is demonstrated by quantifying the area of the bands associated with the C-N stretching of both Amide III (1286 cm^{-1}) and II (1589 cm^{-1}).[331,333,334] Specifically, the average normalized area relative to C-N stretching of Amide III (**Figure 3.1C**) is 0.04 for CE, and it increases to 0.12 and 0.17 for C_CND1 and CE_CND1, respectively. Finally, the normalized area of the C-N stretching of Amide II (**Figure 1C**) increases from 0.12 for CE to 0.24 and 0.38 for C_CND1 and CE_CND1, respectively. By exploiting the native fluorescence of GlyCNDs at an excitation wavelength of 380 nm (**Figure S3.1B, Appendix**), we carried out release studies to further confirm the role of EDC/NHS coupling in achieving a stable immobilization of the GlyCNDs within the collagen matrix. As shown in **Figure 3.1D**, the release of GlyCNDs displayed by CE_CND1 is significantly lower compared to that of C_CND1 condition throughout the full experiment timeframe (30 days). Notably, the release percentage from CE_CND1 at day 4 (~20%) is used to include one additional control for the cellular experiments (referred to as CE+rCND1, and further described in Section 2.3), where

we supplemented the culture medium with the same amount of GlyCNDs released from the CE_CND1 condition at this time point. This enabled us to isolate the cellular effects solely due to the immobilized GlyCNDs from those associated with suspended nanoparticles.

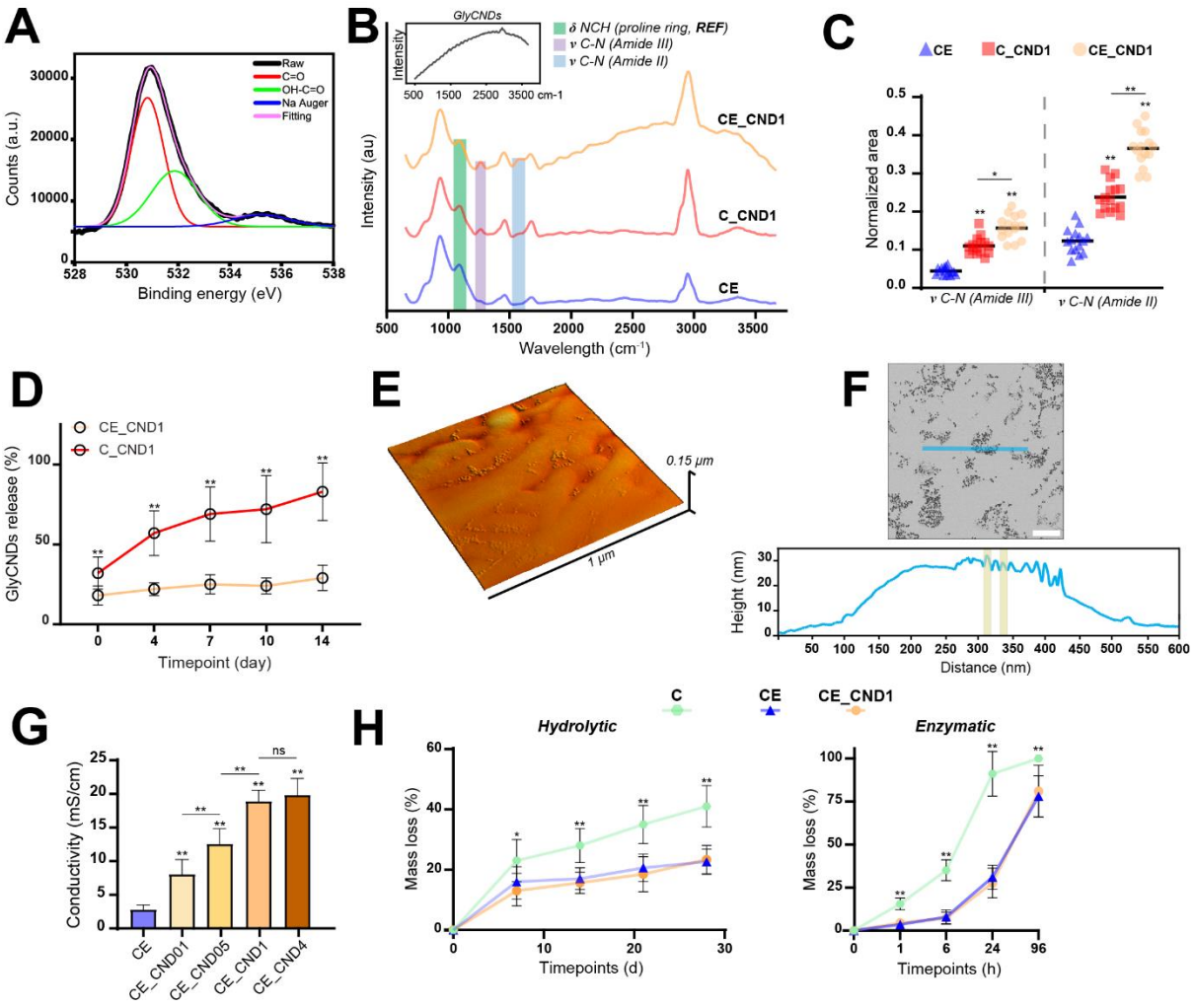

Figure 3.1: Physicochemical, electrical and structural stability characterization of the nanocomposite and relevant control conditions for comparison. (A) Representative high resolution XPS spectrum showing the deconvolution of the O1s region of GlyCNDs. (B) Representative Raman spectra of GlyCNDs (insert), CE, C_CND1 and CE_CND1. (C) Quantification of C-N stretching associated with the Amide III and Amide II groups, normalized against the N-C-H deformation of collagen proline ring. (D) Release profile from collagen hydrogel of both pristine and EDC/NHS-activated GlyCNDs. (E) AFM micrograph of CE_CND1 showing the spatial distribution of GlyCNDs within the collagen fibrous matrix. (F) Representative depth profile extracted from AFM micrograph. Scale bar: 150 µm. (G) Quantification of hydrogel conductivity with variable concentrations of GlyCNDs spanning from 0 (CE) to 4 mg/ml. (H) Hydrolytic and enzymatic degradation of pristine Collagen (C), CE and CE_CND1. All numerical data are presented as mean ± s.d. Statistical significance was determined using one-way analysis of variance (ANOVA) and Tukey's Honestly Significant Difference (HSD) post hoc test: ** $p < 0.01$, * $p < 0.05$, non-significant (ns) $p > 0.05$)

Successively, non-contact Atomic Force Microscopy (AFM) was employed to visualize the GlyCND spatial arrangement within the collagen matrix (**Figure 3.1E**), characterized by randomly distributed clusters of the carbon nanodots. The AFM linear depth profiles (**Figure 3.1F**) confirm a size distribution of the GlyCNDs ranging from ~6 to 16 nm, as previously reported by Naccache and co-authors.[336] Conductivity measurements assessed how the incorporation of GlyCNDs into the collagen matrix modulates the overall electrical properties of the nanocomposite. To this end, different GlyCND concentrations, ranging from 0.1 to 4.0 mg/ml, were tested and the resulting conductivity was compared to the one displayed by CE. As shown in **Figure 3.1G**, the relatively poor conductivity of CE (2.8 mS/cm) significantly increases from the addition of the GlyCNDs up to 1 mg/ml. Interestingly, a higher concentration (i.e., 4 mg/ml) does not result in additional changes. We hypothesize that concentrations higher than 1 mg/ml saturate the availability of free NH_2 groups, thereby resulting in unreacted GlyCNDs that ultimately become suspended and thus do not contribute to the overall conductivity. Finally, we evaluated the chemical stability of the nanocomposite. In accordance with results already reported in the literature,[338,339] we found that the presence of EDC/NHS greatly improves the resistance to both hydrolytic (**Figure 3.1H**) and enzymatic (**Figure 3.1H**) degradation of pristine collagen (hereafter referred to as C). Both CE and CE_CND1 conditions display a significantly lower mass loss due to hydrolytic degradation when compared to C. The same consideration is also valid for enzymatic degradation in the presence of collagenase IV. This increased stability of the CE_CND1 condition highlights the potential of our novel nanocomposite to overcome one of the major limitations of collagen hydrogels for tissue engineering and neural applications.

Finally, we performed a comprehensive mechanical characterization of the novel nanocomposite against the relevant control conditions via AFM nanoindentations (see **Chapter 6.2.1** in the appendix for the detailed description of the experimental set up and data post

processing). The analysis of the AFM force-indentation curves enabled the extraction of sample's stiffness and Young's modulus. As shown in **Figure S3.1D**, pristine collagen displayes the lowest stiffness (1.92 × 10−3 N m−1) and Young's modulus (609 Pa). As expected, EDC/NHS cross-linking in the CE condition results in a higher stiffness (2.28 × 10−3 N m−1) and Young's modulus (735 Pa). In agreement with the rheological measurements, the mechanical properties are not altered by the incorporation of GlyCNDs. The nanocomposite CE_CDN1 displays stiffness and Young's modulus values of 2.37 × 10−3 N m−1 and 744 Pa, respectively, with no statistically significant differences with the CE condition. The results found for CE and CE_CND1 enabled us to conclude that the rheological and mechanical properties, namely viscosity and stiffness, are not expected to be a major contributing factor for the cellular results reported in the following sections.

3.3.2 Cytotoxicity assays

Despite the considerable efforts to characterize the potential neurotoxicity of carbon-based nanomaterials,[340–342] the results reported in the literature remain controversial, likely due to inter-study variations in size, physicochemical properties and concentration. Here, to evaluate the cytocompatibility of both collagen-immobilized and suspended GlyCNDs with iPSCs-derived NP spheroids, we carried out a colorimetric LDH assay complemented with propidium iodide (PI) live staining of dead cells. Three different concentrations (i.e., 0.5 mg/ml, 1 mg/ml and 4 mg/ml) of GlyCNDs were both immobilized within the collagen matrix by EDC/NHS coupling (hereafter referred to as CE_CND05, CE_CND1, CE_CND4) and suspended in the culture medium (hereafter referred to as CE+CND05, CE+CND1, CE+CND4). Pristine collagen (C) and EDC/NHS crosslinked collagen (CE) were used as controls. **Figure 3.2A** displays the percentage values of released LDH found for the different conditions at 6 and 72h.

The results indicate that the viability of NC spheroids is not impacted by GlyCNDs immobilized within the collagen matrix at concentrations of 1 mg/ml or lower. In fact, the percentage values of released LDH of CE_CND05 and CE_CND1 are not statistically different from the ones displayed by the control groups at both time intervals. Conversely, we observed that CE_CND4 significantly increases cell mortality at both time points, with LDH percentage values that doubled in comparison to those displayed by the controls. When GlyCNDs are suspended in the culture medium, significantly higher levels of LDH are observed for both time points. In particular, the cytotoxicity increases proportionally with the GlyCNDs concentration, with CE+CND4 displaying the highest LDH release values. These results were further complemented by PI staining of the NP spheroids at 72 h. **Figure 3.2B** displays representative images of controls, immobilized and suspended GlyCNDs conditions. It is evident that NP spheroids cultured in the GlyCNDs-supplemented medium display significantly higher

amounts of dead cells compared to both controls and collagen with immobilized GlyCNDs.

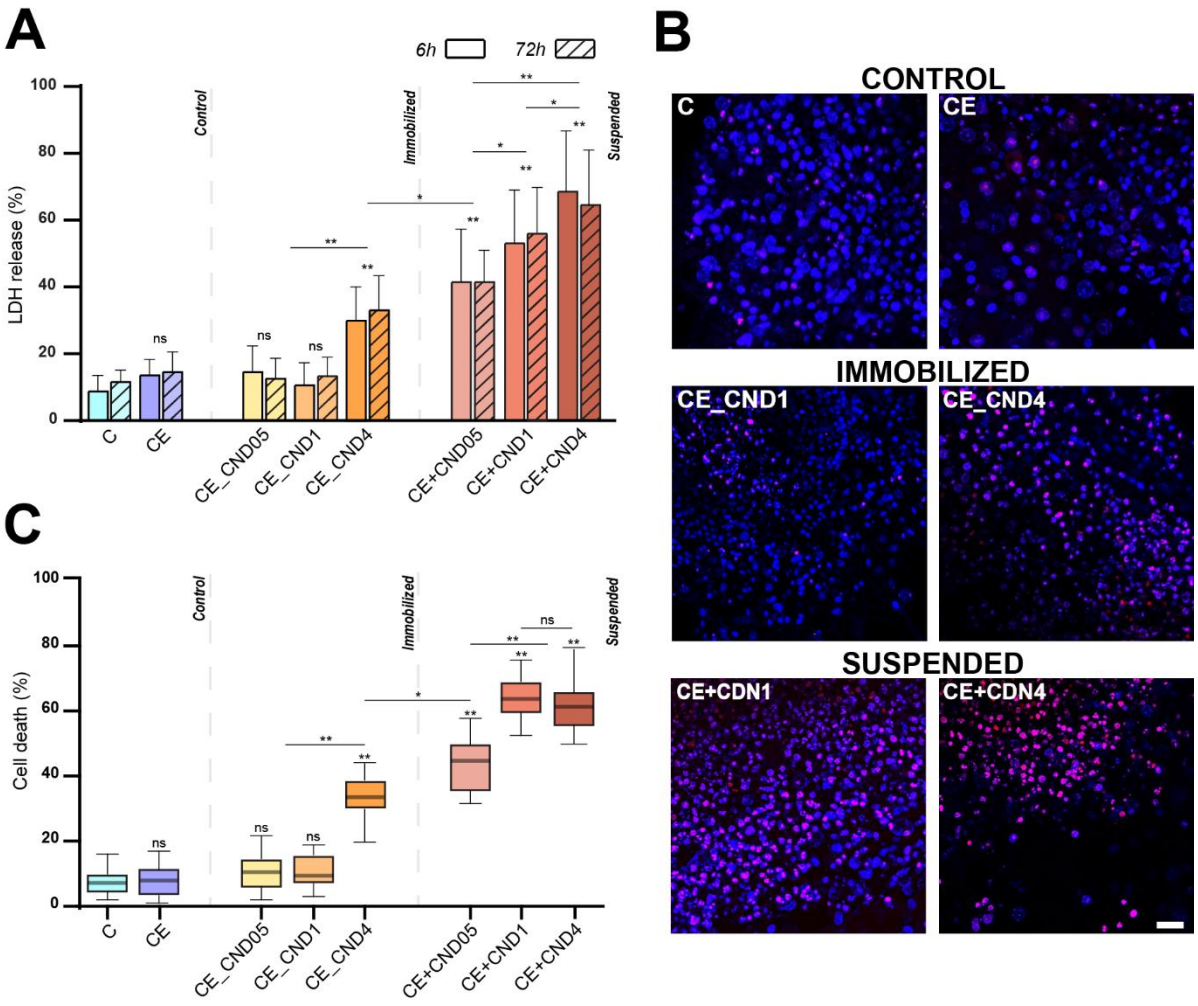

Figure 3.2: Cytotoxicity study of both suspended and immobilized GlyCNDs. The immobilization of GlyCNDs within the collagen matrix hinders potential cytotoxic effects arising from the presence of suspended nanoparticles, yielding a cell viability similar to that of pristine collagen. Different concentrations of GlyCND were both immobilized within the collagen matrix (_) and suspended in culture medium (+). Pristine collagen (C) and EDC/NHS crosslinked collagen (CE) were employed as controls. (A) LDH percentage release for the different conditions tested. (B) Representative PI/DAPI staining images for control conditions C and CE, suspended GlyCNDs at a concentration of 1 mg/ml and 4 mg/ml and immobilized GlyCNDs at a concentration of 1 mg/ml and 4 mg/ml. Scale bar: 25 µm. (C) Cell death for the different conditions. All numerical data are presented as mean ± s.d. Statistical significance was determined using one-way analysis of variance (ANOVA) and Tukey's Honestly Significant Difference (HSD) post hoc test: ** $p < 0.01$, * $p < 0.05$, non-significant (ns) $p > 0.05$).

Cell death percentage (**Figure 3.2C**) was calculated as the PI-positive (PI^+) cells over the total amount of nuclei. Not surprisingly, PI staining mirrors the results obtained with the LDH assay. Immobilized GlyCNDs display similar cell death percentages to control groups, while

suspended GlyCNDs yield higher cytotoxicity. Overall, our results provide additional evidence to support recent arguments that emphasize the need for immobilization of carbon-based nanomaterials within scaffolds to mitigate undesirable outcomes that are associated with their use as suspended particles, such as bioaccumulation (**Figure S3.1C**, **Appendix**).[330,342,343]

Furthermore, the consistent LDH values found at 6 and 72 h across all conditions with suspended GlyCNDs indicate cell death onset within the first 6 h of exposure. Most importantly, the cytotoxicity assays played a crucial role in determining that immobilized GlyCNDs at a concentration of 1 mg/ml displayed viability results that were comparable to those of the control groups, while greatly improving the poor electrical conductivity of pristine collagen. For this reason, we selected CE_CND1 as the experimental condition for the cell studies presented in the following sections.

3.3.3 Neurite growth and formation of a complex neuronal network

One of the primary goals of neural tissue engineering is to develop functional scaffolds that favor neurite spreading and extension while supporting the establishment of complex neural networks. After only 5 days in culture, several neurites spreading from spheroids embedded in the CE_CND1 nanocomposite are visible, while none/few are observed in control conditions (i.e., CE and CE+rCND1) (**Figure S3.2A**, **Appendix**). To quantitatively characterize morphological differences, the spheroids were stained for β III-tubulin and imaged via confocal microscopy at 14 days. The CE_CND1 promotes a significantly more extensive neurite outgrowth when compared to CE and CE+rCND1 (**Figure 3.3A**). The overall branching complexity was evaluated using a semi-automated Sholl analysis centred on the spheroid's body. In particular, the total number of neurite intersections was calculated using 20 μm-spaced concentrical hemispheres (**Figure 3.3B**). As shown in **Figure 3.3C**, spheroids within the CE_CND1 condition exhibit an average number of neurite intersections of 95 ± 28, which is

significantly higher than when they are placed within CE (58 ± 21) and CE+rCND1 (47 ± 18) matrices. To evaluate the neurite ramification tendency, we utilized the Schoenen index, defined as the maximum number of intersections divided by the number of primary branches exiting from the spheroid's soma.

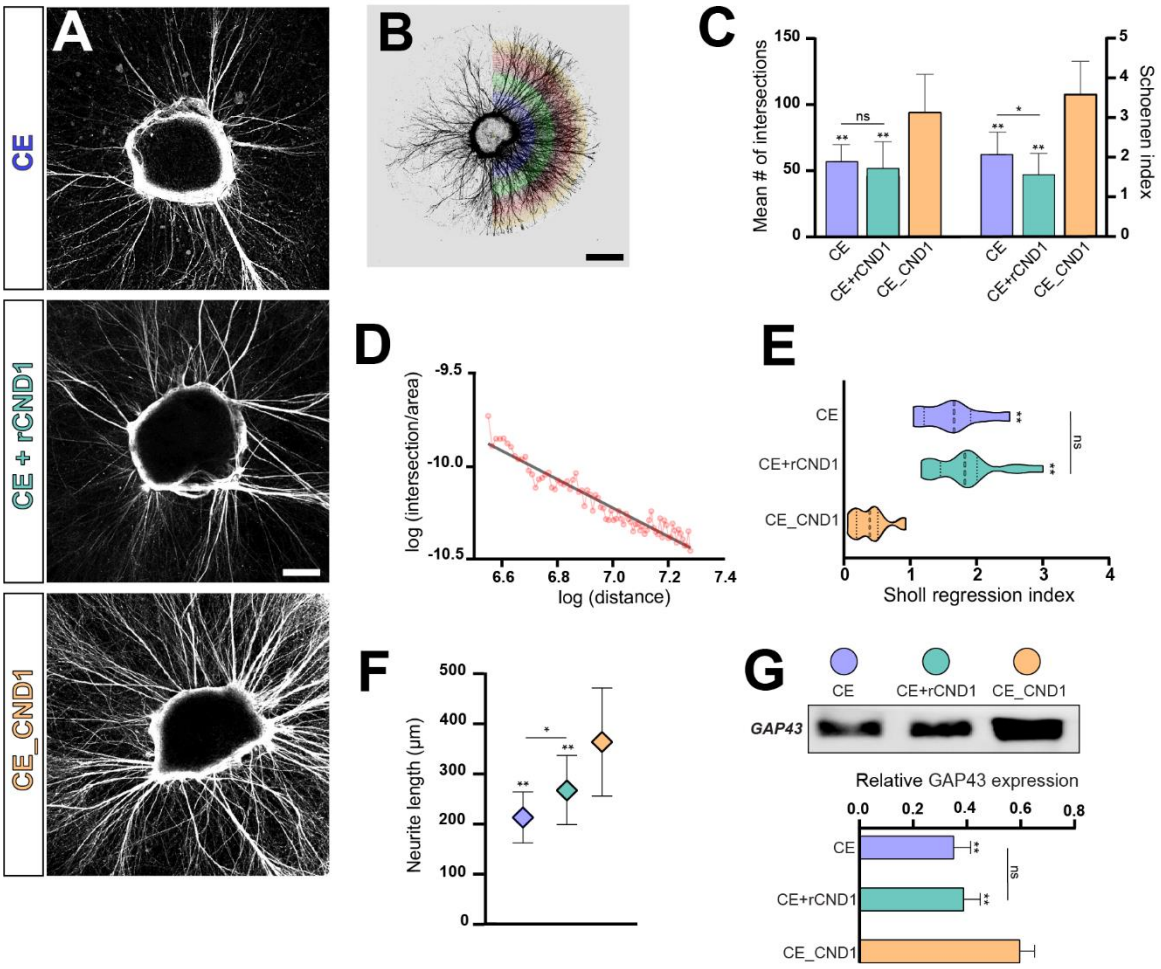

Figure 3.3: Morphological analysis of NPs spheroids cultured into the novel nanocomposite. CE_CND1 matrix promotes neuritogenesis and the formation of complex neural networks (A) β-III tubulin expression of NP spheroids embedded in CE, CE_rCND1 and CE_CND1. Scale bar: 250 µm (B) Semi-automated Sholl analysis performed on NP spheroids encompassing the use of 20 µm-spaced concentric hemispheres (centered around the spheroid's soma). Scale bar: 600 mm. (C) Number of neurite-hemisphere intersections and Schoenen ramification index. (D) Representative linear regression applied to the area-normalized intersections as a function of the distance from the spheroid's soma. (E) Sholl's regression index. (F) Quantification of neurites' length. (G) Relative expression of GAP43. All numerical data are presented as mean ± s.d. Statistical significance was determined using one-way analysis of variance (ANOVA) and Tukey's Honestly Significant Difference (HSD) post hoc test: ** $p < 0.01$, * $p < 0.05$, non-significant (ns) $p > 0.05$).

As shown in **Figure 3.3C**, the CE_CND1 condition displays the highest average index of 3.6 ± 0.8. Interestingly, the significantly lower average value found for spheroids in the CE+rCND1 condition when compared to CE (i.e., 1.7 vs 2.1), indicates that the released GlyCNDs have detrimental effects on the formation of a complex neuronal network, thereby confirming previous similar observations with carbon nanomaterials.[309,312,313,318] The overall increased branching complexity of spheroids in CE_CND1 is also validated by Sholl's regression index, a parameter that quantifies the rate of decay of the number of branches with distance from the center of analysis (**Figure 3.3D**). As shown in **Figure 3.3E**, the CE_CND1 condition is characterized by the lowest index (0.3) when compared to that of the CE (1.6) and CE+rCND1 (1.8) matrices.

In addition to the increased neural network complexity, spheroids embedded in the CE_CND1 also display the highest neurite length (**Figure 3.3F**) of 369 ± 113 µm. Interestingly, in the CE+rCND1 matrix, neurites are significantly longer when compared to the CE condition (i.e., 273 ± 78 µm vs 207 ± 53 µm). To unveil the underlying mechanisms that drive such divergent morphology, we investigated via Western blotting the expression of growth-associated protein 43 (GAP43), a crucial protein for *neuritogenesis*.[344–346] As shown in **Figure 3.3G**, spheroids in CE_CND1 express a significantly higher amount of GAP43 at 14 days compared to those within the control conditions. Taken together, our findings reveal that immobilized GlyCNDs upregulated NP spheroid expression of GAP43, which is decisive in neurite outgrowth and complex neural network formation. In contrast, although GlyCNDs released in solution facilitate the development of longer neurites, they exhibited significantly lower ramifications than NP spheroids embedded in CE.

To investigate whether the ability of the nanocomposite to support *neuritogenesis* extends to mature neurons, we used the CE_CND1 nanocomposite as a matrix for a scaffold-based 3D culture of mouse primary cortical neurons, confirming that the establishment of a complex

neural network is observed within 7 days (**Figure S3.2B, Appendix**). Compared to CE, cortical neurons grown in the CE_CND1 matrix show a significant increase in neurite outgrowth that enabled the formation of intricate networks. Notably, the morphology elicited by CE_CND1 was comparable to the one observed in Matrigel, the gold standard matrix in neurobiology.[347] The use of a different cell type offers a compelling validation of the nanocomposite's distinctive ability to support key processes associated with neuro-regeneration. The consistency of results between NP spheroids and primary cortical neurons supports in fact the evidence that the nanocomposite's beneficial effects transcend specific cell types and *in vitro* testing platforms. Both spheroids and the 3D culture of primary neurons emulate more closely than conventional 2D monolayer systems the *in vivo* cellular environment, thereby providing a physiologically relevant representation of neuron-biomaterial interactions. Taken together, our findings highlight the potential wide-ranging applicability of the CE_CND1 nanocomposite for the reconstruction of lost neuroanatomical connectivity.

3.3.4 Neuronal differentiation

To expand the breadth of the investigation of the beneficial effects of the nanocomposite, we evaluated the expression levels of key neuronal maturation markers by immunofluorescence (IF) imaging and Western blotting. **Figure 3.4A** displays representative IF images of NP spheroids embedded in CE, CE+rCND1 and CE_CND1 after 2 weeks of culture. Samples were stained for Ki-67, a nuclear proliferation marker,[348] as well as for β III-tubulin and MAP2, an early and a mature neuronal marker, respectively.[349,350] The overall expression of these proteins indicates that the differentiation of the neurospheres embedded in the CE_CND1 matrix is promoted, showing significantly lower amounts of Ki-67-positive cells and higher levels of β III-tubulin and MAP2 (**Figure 3.4B**). These findings are also corroborated by the relative expression of calretinin (an early neuronal marker) and nestin (a neural progenitor

marker).[351,352] In particular, spheroids cultured in CE and CE+rCND1 matrices display a higher amount of nestin when compared to the ones embedded in CE_CND1, which instead express higher levels of calretinin (**Figure S3.3, Appendix**).

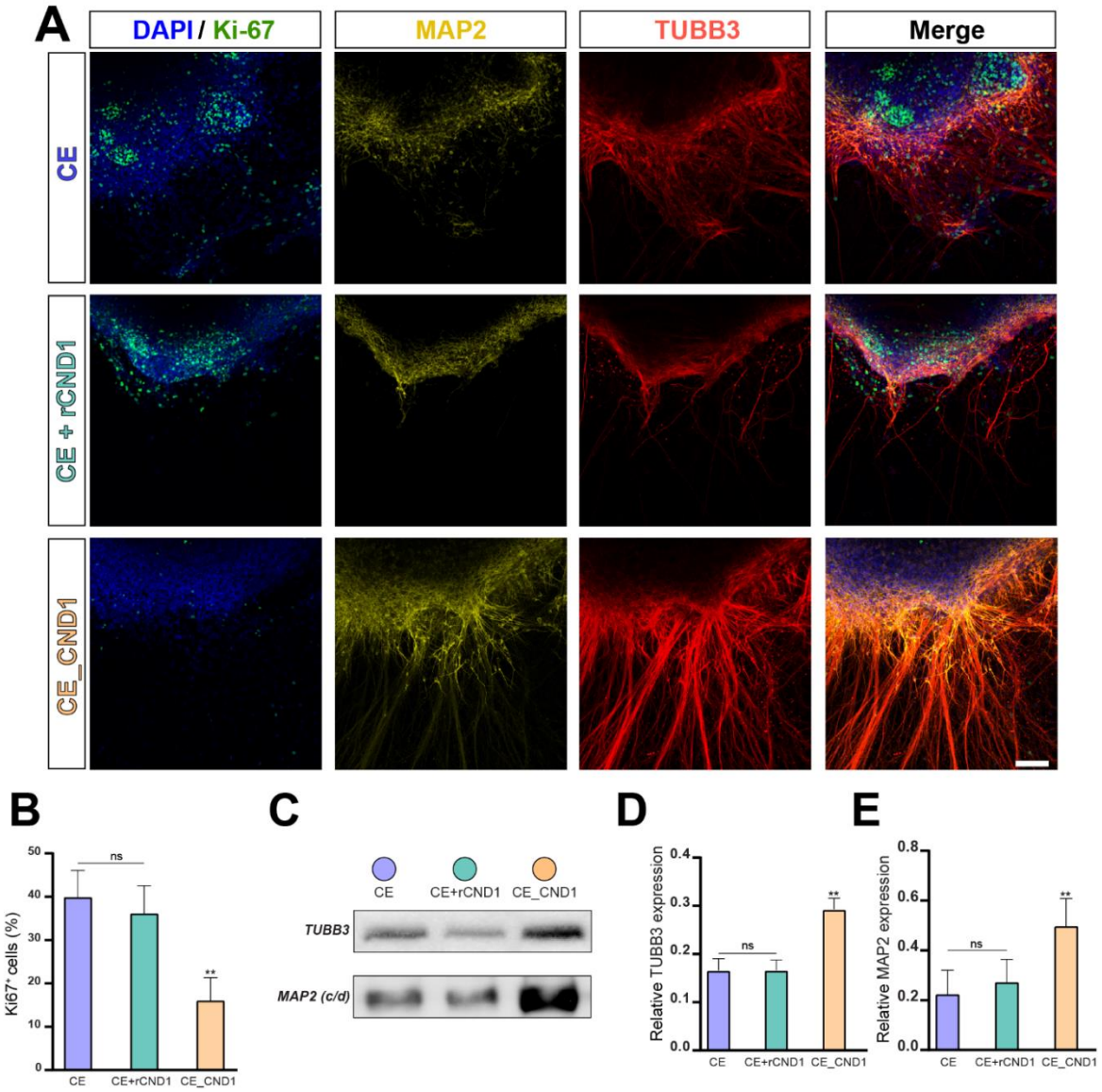

Figure 3.4: Evaluation of neuronal differentiation of NPs spheroids cultured into the novel nanocomposite. CE_CND1 supported the early differentiation of NP spheroids into mature neurons (A) Representative immunofluorescence images showing the expression of Ki-67, MAP2 and β III-tubulin in spheroids cultured in CE, CE_rCND1 and CE_CND1 for 14 days. Nuclei were stained with DAPI. Scale bar: 100 µm. (B) Quantification of the percentage of Ki-67 positive cells (Ki-67^{+}). (C) Western blot analysis of β III-tubulin and MAP2 c/d expression. (D) Quantification of β III-tubulin expression level. (E) Quantification of MAP2 c/d expression level. All numerical data are presented as mean ± s.d. Statistical significance was determined using one-way analysis of variance (ANOVA) and Tukey's Honestly Significant Difference (HSD) post hoc test: ** $p < 0.01$, * $p < 0.05$, non-significant (ns) $p > 0.05$).

Quantitative Western blot analysis (**Figure 3.4C**) confirms IF imaging results by showing a higher relative expression of β III-tubulin for neurospheres in CE_CND1 (0.29) when compared to CE and CE+rCND1 (0.17 each) (**Figure 3.4D**). As shown in **Figure 3.4E**, similar considerations are also valid for MAP2, with higher expression (0.48) in the CE_CND1 nanocomposite.

Taken together, our findings indicate that the immobilized GlyCNDs induce a rapid neuronal differentiation and maturation of NP spheroids. This evidence is supported by the fact that the nanoparticles released from the matrix (CE_rCND1) do not elicit any effect on differentiation, similar to the condition where they are absent (CE). The positive effects of immobilized GlyCNDs strengthen the potential and impact of carbon-based nanomaterials in neural tissue engineering. Specifically, the accelerated *neuritogenesis* and the elevated expression of the mature neuronal marker MAP2 highlight the remarkable capacity of our nanocomposite to accelerate neuronal differentiation of NPs (compared to previous literature on miPSCs)[353,354] and ensure their complete electrophysiological maturation, two crucial aspects for biomaterial-driven neural development and regeneration.

3.3.5 Electrophysiological maturation and neuronal network communication

Lastly, we evaluated the spontaneous electrical activity of NP spheroids, both at the single-electrode and network level, by capitalizing on commercially available multi-electrode arrays (MEAs) (**Figure 3.5A**). Starting at day 5 and consistently throughout the entire experimental duration (28 DIV), NP spheroids in the CE_CND1 matrix exhibit a remarkable enhancement in single-electrode activity. Specifically, the firing rate, which reflects the frequency of action potentials, is significantly higher than the other experimental groups (**Figure 3.5C**). Furthermore, an increased number of active electrodes (**Figure 3.5D**) and an enhanced burst

frequency can be observed (**Figure 3.5E**), indicating an increased synchronized activity among the cells in the spheroids.

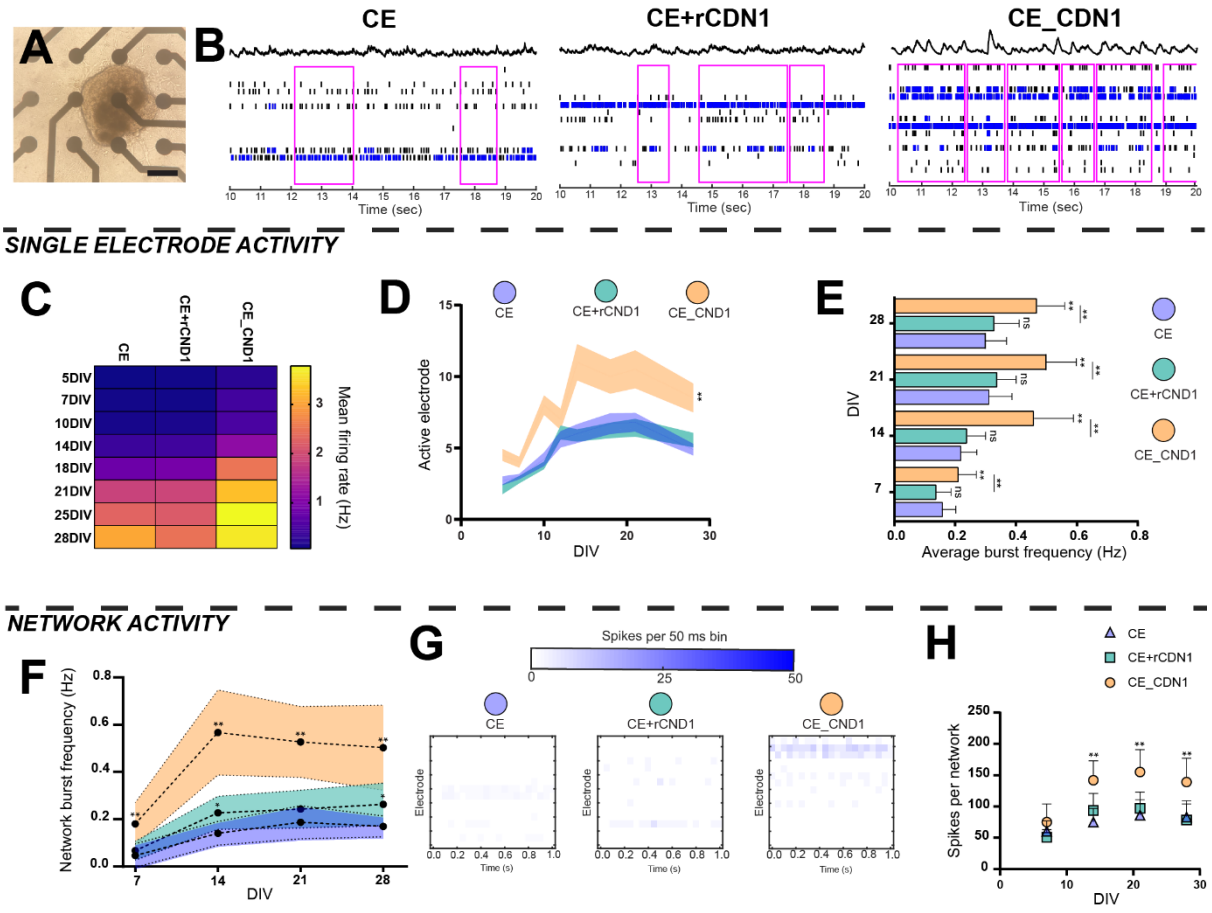

Figure 3.5: Evaluation of the electrophysiological maturation and neural network formation of NPs spheroids cultured into the novel nanocomposite. Spheroids cultured in the CE_CND1 nanocomposite show faster and more integrated electrophysiological maturation. (A) Representative image of NP spheroids cultured in MEAs well plates. Scale bar: 300 µm. (B) Representative activity traces at 14 days *in vitro* (DIV) for CE, CE_rCND1 and CE_CND1. Single detected spikes are represented by the black lines in the raster plots, while blue lines indicate single electrode burst. Neural networks are shown as pink rectangles. (C) Heating map showing the weighted mean firing rate during 28 DIV. (D) Number of detected active electrodes during 28 DIV. Shadowed areas represent mean ± s.d (E) Single electrode burst frequency. (F) Network burst frequency. (G) Representative 1s- binning raster plots showing singular spikes detected within network activity at 14 DIV for CE, CE_rCND1 and CE_CND1. (H) Spikes per network activity during 28 DIV. All numerical data are presented as mean ± s.d, except for (G) where mean ± SEM are presented. Statistical significance was determined using one-way analysis of variance (ANOVA) and Tukey's Honestly Significant Difference (HSD) post hoc test: ** $p < 0.01$, * $p < 0.05$, non-significant (ns) $p > 0.05$).

In addition to the single-electrode level, the CE_CND1 nanocomposite also positively influenced the network burst frequency, a measure of large-scale synchronized activity among

different electrodes, which is consistently and significantly higher for the spheroids embedded in CE_CND1 (**Figure 3.5F**). This result indicates that the CE_CND1 nanocomposite facilitates the formation of functional connections among cells, yielding a more integrated neuronal network. In addition, the average number of spikes per network burst is notably higher (**Figure 3.5 G,H**), suggesting that the spheroids cultured in the nanocomposite established more complex and intensified network communications. By day 14, neurospheres show remarkable single-electrode activity and the generation of intricate neuronal network connections (**Figure 3.5B**). The importance of immobilizing the GlyCNDs within the collagen matrix is further demonstrated by the electrophysiological recordings relative to the CE_rCND experimental group. In fact, released GlyCNDs did not elicit noticeable or consistent alterations from the electrical signature that was displayed by CE, neither at the single electrode nor at the network level. These findings demonstrate that collagen-immobilized GlyCNDs provide a favorable microenvironment that accelerates the electrophysiological maturation and the establishment of effective neural network formation. Together with the neuronal differentiation and the morphogenesis data reported in the previous sections, these results demonstrate that the electroconductive nanocomposite enhances the maturation of functionally active neuronal cells and promotes their communication through an intensified neural network. To gain a deeper understanding of the underlying mechanisms that contribute to such enhanced electrophysiological activity, we investigated by immunofluorescence and Western blotting the expression of synapsin (i.e., a crucial phosphoprotein known to promote the establishment and maintenance of synaptic connections by actively regulating the release of neurotransmitters) and that of NMDA receptors (NMDAr), which are primarily involved in the transmission of excitatory information.[355–357] **Figure 3.6A** shows that NP spheroids embedded in CE_CND1 exhibit higher levels of synapsin, namely 0.27 versus 0.16 and 0.18 for the CE and CE_rCND1

groups, respectively (**Figure 3.6C**, **D**). On the other hand, NMDA receptor levels are comparable for the conditions tested (**Figure 3.6B, C, E**).

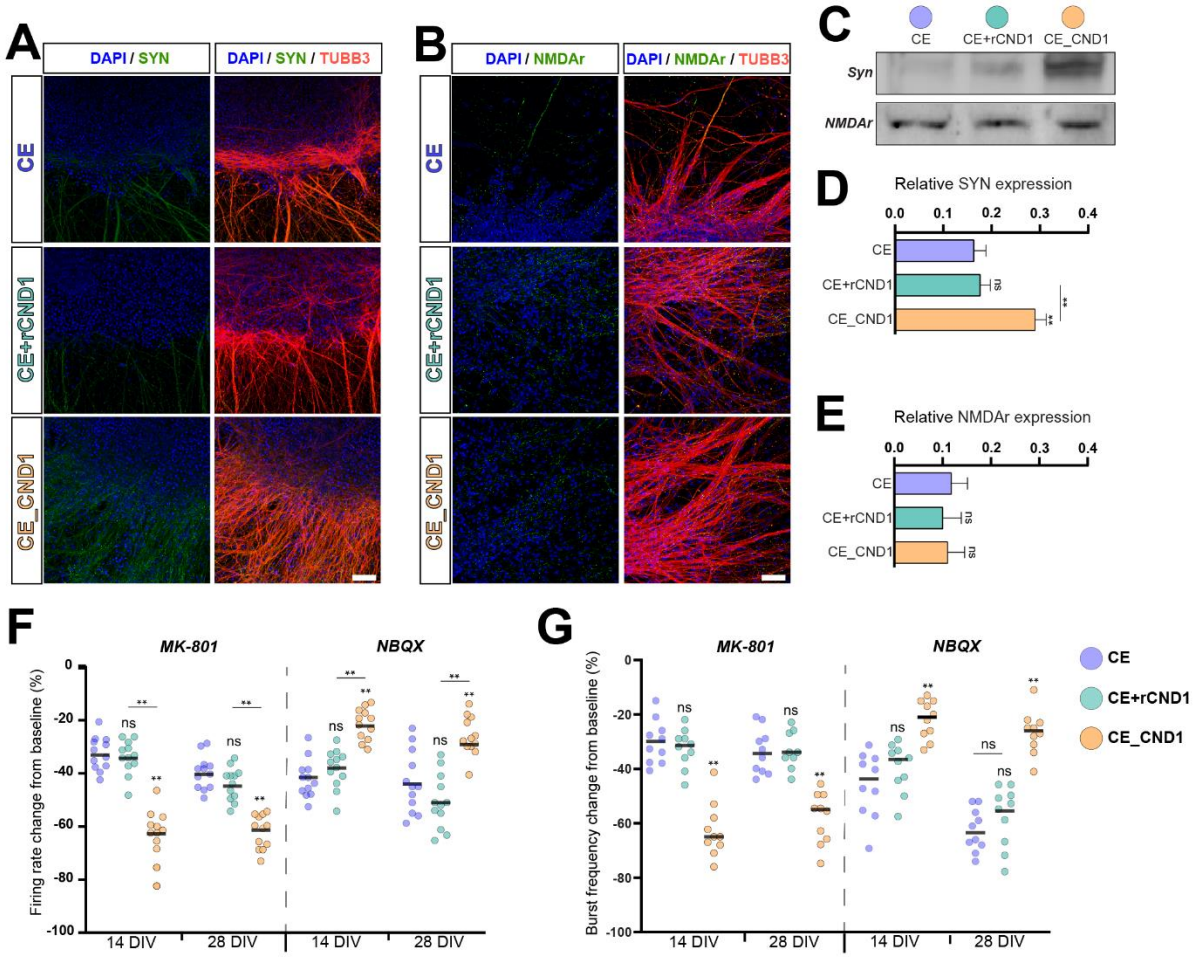

Figure 3.6: NMDA receptors greatly influence the electrophysiological signature of NP spheroids embedded in the nanocomposite. (A) Representative immunofluorescence images showing the 14-day expression of synapsin and β III-tubulin in spheroids cultured in CE, CE_rCND1 and CE_CND1 matrices. Nuclei were counterstained with DAPI. Scale bar: 100 μm. (B) Representative IF images of NMDAr and β III-tubulin in spheroids cultured in CE, CE_rCND1 and CE_CND1 matrices. Nuclei were stained with DAPI. Scale bar: 100 μm. (C) Western blot analysis of synapsin and NMDAr expressions. (D) Quantification of synapsin expression levels. (E) Quantification of NMDAr expression levels. (F) Percentage firing rate deviations from baseline recordings following acute MK-801 and NBQX treatment performed at 14 and 28 DIV. (G) Network burst frequency deviations from baseline recordings following acute MK-801 and NBQX treatment performed at 14 and 28 DIV. All numerical data are presented as mean ± s.d. Statistical significance was determined using one-way analysis of variance (ANOVA) and Tukey's Honestly Significant Difference (HSD) post hoc test: ** $p < 0.01$, * $p < 0.05$, non-significant (ns) $p > 0.05$).

However, acute treatment with MK-801, a non-competitive NMDA receptor antagonist, significantly affects the electrical activity and namely that of the spheroids embedded in the CE_CND1 nanocomposite. As depicted in **Figure 3.6F**, upon treatment with MK801 on day

14 and 28, the firing rate exhibits a reduction of 63% and 61%, respectively, compared to the spontaneous baseline recording. Furthermore, MK-801 acute treatments are also found to reduce the network activity (**Figure 3.6G**). Notably, the impact of NMDAr antagonist is significantly more severe on the firing rate and network burst of the spheroids embedded in CE_CND1, indicating an overall activity that is heavily dependent on the availability of NMDA receptors. In comparison, acute treatment with NBQX, a commonly used AMPA and kainate receptor blocker, yields the opposite trend, whereby neurospheres in CE_CND1 are significantly less susceptible to AMPA receptor antagonist than those in the CE and CD_rCND1 matrices at both 14 and 28 days.

This differential impact of the two antagonists suggests that the electrophysiological activity of NP spheroids is mainly governed by NMDAr activation. Based on these findings, we hypothesize the presence of direct interactions between the GlyCNDs in the CE_CND1 and NMDAr alters the channel dynamics and ultimately leads to channel activation. Although this theory needs further scrutiny since other surface receptors (e.g., neurotrophin and nerve growth factor) can regulate NMDAr-dependent currents,[358] our findings nonetheless indicate biomaterial-derived effects on the NMDA receptors which may, either completely or in part, explain the reported cellular effects, as NMDAr activation is known to drive neurite growth, neural differentiation and maturation as well as electrical activity.

3.4 CONCLUSION

In conclusion, this work presents a novel electroconductive nanocomposite consisting of a collagen type I matrix decorated with GlyCNDs, ultimately demonstrating its promising potential as a biomaterial for applications ranging from neural tissue engineering and neuro-regenerative medicine to bioinks and matrices for 3D cultures and biomimetic *in vitro* models. After establishing an effective anchorage method for GlyCNDs within the collagen matrix through EDC-NHS coupling, we carried out a cytotoxicity assay to inform the optimization of GlyCNDs concentration towards a biocompatibility comparable to that of pristine collagen. The biological characterization of the nanocomposite was carried out with mouse iPSCs-derived NP spheroids (and, in part, with a 3D culture of primary neurons) for a more physiologically accurate representation of *in vivo* conditions towards enhancing the reliability and translatability of our findings. The CE_CND1 nanocomposite substantially enhances the neuronal differentiation of NP spheroids and promotes *neuritogenesis*, with conspicuous dendritic arborization and axonal outgrowth, ultimately facilitating the formation of functional and highly integrated neural networks. Furthermore, acute MK-801 treatment suggests a direct interaction between collagen-immobilized GlyCNDs and post-synaptic NMDA receptors.

Results from this work thus provide the fundamental knowledge for a new biomaterial-based tissue engineering strategy for the treatment of neuronal disorders via the restoration of lost neurons and neuroanatomical connectivity, thereby aiming to address the key pathological substrate of these pathologies and ultimately improving the life of millions of patients worldwide.

CHAPTER4: Neuro-regenerative potentials of anisotropically oriented collagen hydrogel via remote magnetic field application.

4.1 INTRODUCTION

The ability of mammalian neuronal cells to self-regenerate following either physical trauma or neurodegenerative disease is limited.[359] Many efforts have thus been made toward the development of scaffolds that guide neuronal regeneration.[360,361] Among the different materials' physicochemical properties known to modulate cellular responses, topographical guidance has been shown to play a pivotal role.[362] Several works have shown the ability of specific physical cues (i.e., microchannels, pillars)[57,58,64,65,68] to guide the orientation of neurons, to determine significant morphological transitions and to guide the neurogenic differentiation of stem cells.[61,66,68,74]

Collagen type I has been traditionally recognized for its excellent biodegradability, biocompatibility, and accessibility.[363] In addition, its fibrillar nature coupled with high versatility enables the fabrication of highly anisotropic scaffolds, making collagen a promising candidate for neural tissue applications. For these reasons, many researchers have been actively exploring different fabrication techniques such as electrospinning,[364,365] microfluidics[366] and strain-induced[367] alignment to generate anisotropically oriented collagen fibrous hydrogels. Despite their proven effectiveness, these methods necessitate *ex-vivo* manipulations prior to the interactions with cells or the implantation site, which could lead to changes in the biological properties of the scaffold and increase the fabrication complexity. Hence, there is a pressing need to conceive a fabrication approach that encompasses the alignment of collagen *in vivo* that could guarantee the preservation of the biological and mechanical characteristics of the scaffold while fostering a more natural interaction with the native tissue environment.

To bridge this gap, we demonstrate that a collagen-based hydrogel containing functionalized paramagnetic beads can be aligned via the remote application of a magnetic field. While this set-up has been tested by many throughout the years,[368,369] the unique peculiarities of our

approach encompass: i) the functionalization of the paramagnetic beads with laminin ii) the establishment of an optimized timing for magnetic induction during collagen fibrillogenesis and iii) the use of a 3D culture system.

Regarding bead functionalization, our findings revealed that laminin-functionalized beads yield superior collagen alignment, outperforming both pristine (-COOH) and streptavidin-functionalized beads (the most reported choice in literature). In addition, we hypothesized that laminin, greatly known for facilitating neuronal cell population adhesion and spreading,[61,68,69] could serve in establishing additional anchorage points for better cellular adhesion. Regarding magnetic induction timing, a parameter whose importance in influencing the collagen alignment outcome has been greatly overlooked in the past, this study establishes an optimized protocol based on the in-depth study of collagen fibrillogenesis.

Mouse iPSCs-induced neural stem cells (NSCs) were employed to evaluate the biological activity of the novel collagen hydrogels. The aligned hydrogel (hereafter referred to as A_LAM) was shown to facilitate NSCs adhesion with the formation of significantly higher focal adhesion points when compared to collagen alone (hereafter referred to as COL).

Our study revealed that the anisotropic distribution of collagen fibers significantly influenced the differentiation dynamics of NSCs. In fact, within 48 hours of magnetic induction, NSCs seeded within A_LAM were found to express a significantly higher amount of NeuroD1 marker compared to COLL and to its not aligned counterpart (hereafter referred to as LAM), suggesting that A_LAM elicits an early onset toward the neurogenic differentiation. In addition, we observed that NSCs seeded within A_LAM presented a notable reduction in the levels of active-YAP1, the main effector of the Hippo pathway. This finding suggests that the anisotropic topography presented by A_LAM plays a role in eliciting differential activation patterns within the Hippo pathway, readily guiding cells toward a neurogenic fate as opposed to proliferative trajectories.

Finally, we evaluated the effect of anisotropic fiber in modulating the orientation and neurite outgrowth of NSCs, two critical aspects that greatly determine the success of neural regeneration strategies. Our findings revealed the outstanding ability of A_LAM in preferentially orienting NSCs along with the fibers' direction. In addition, despite the similar average neurite length found across conditions, NSCs embedded in A_LAM displayed a significantly higher average longest neurite length compared to the control conditions. This implies that the anisotropic orientation of collagen fibers characteristics of A_LAM facilitates a subset of NSCs to develop more elongated neurites, which could potentially serve as pivotal guides during the neuronal regeneration process.

4.2 MATERIALS AND METHODS

4.2.1 Paramagnetic beads functionalization

Carboxyl functionalized paramagnetic microbeads (Dynabeads^{TM} MyOne^{TM}, USA, 65011) were introduced in the collagen suspension. The beads were used either in their pristine state or were further functionalized with biomolecules that have a high affinity with collagen (i.e., laminin and streptavidin) by EDC-NHS coupling. Briefly, the pristine beads were immersed for 1h in the activation buffer consisting of 50mM MES buffer (pH 6.0) containing 10mM EDC and 5mM NHS. The beads were then centrifuged and washed twice in MES buffer and immersed for 30 min in the reaction buffer consisting in 50 mM MES and one of the proposed biomolecules at a concentration of 80µg/ml. The functionalized beads were then washed twice with dH_2O and stored in the fridge for future use. To confirm the effective biomolecule functionalization, the beads were labeled with Alexa Fluor™ 555 NHS Ester (ThermoFisher, A20000) and imaged with a brightfield AxioObserver Z1 microscope (Zeiss) using a 40X objectives (0.95 NA).

4.2.2 Hydrogel preparation

Hydrogels were prepared using rat tail-derived type I collagen (Corning, 9.38 mg/ml, #354249). All reagents were pre-cooled at 4 °C and placed on ice to prevent any premature gelation upon mixing. The gelling procedure was performed following the manufacturer's instructions. Briefly, under sterile conditions, collagen stock was diluted in Neurobasal expansion media (see protocol below) and PBS 10X to achieve a final matrix concentration of 1mg/ml. To ensure the proper collagen polymerization, the solution was buffered to a pH of 7.4 by adding 1N NaOH. Finally, the paramagnetic beads were introduced into the mixture at different concentrations ranging from 0.5 to 10 %vol/vol to assess the resulting alignment. Aliquots of 10uL were pipetted in 96 well-plate and a commercially available bar magnet (K&J Magnetics, USA, #BY088) was then placed atop the samples at different timepoints that were chosen according to the turbidity curve obtained by gathering the absorbance peak at 400nm. After 1h, the samples were incubated at 37 °C to ultimate the polymerization. The magnet was removed the following day.

4.2.3 Turbidity studies

The dynamics of collagen fibrillogenesis was evaluated via absorbance readings. Sinergy H1 plate reader (BioTech® Instruments, USA) was employed to gather the absorbance peak at 400nm at different timepoints.[177] The absorbance values were then employed to optimize the timing of collagen's magnetic induction which would lead to the most efficient alignment of the fibers.

4.2.4 Fiber alignment quantification

Collagen samples were visualized via confocal reflectance on a LSM880 AxioObserverZ1 equipped with a superhigh resolution Airyscan detector using a 405nm laser and W Plan-

Apochromat 20X/1.0 NA objective. Several z-stacks were gathered throughout the thickness of the samples. The images were then analyzed in ImageJ using the OrientationJ plugin to extract the fiber orientation distributions. The curves were then fitted to a Gaussian distribution on OriginPro software to determine the FWHM values.

Considering the orientation analysis, we delineate the experimental for the subsequent cell culture studies. In particular, the collagen configuration that provided the best fiber alignment (i.e., collagen matrix incorporating laminin-functionalized beads aligned through magnetic field applied after 10 minutes) was chosen as the aligned condition (hereafter referred to as A_LAM) and compared to different control conditions where the collagen fibers where not aligned. Pristine collagen (hereafter referred to as COL) and composite hydrogel made of collagen matrix incorporating pristine beads (hereafter referred to as COOH) were used to elucidate the cellular effects elicited by the introduction of laminin-functionalized beads within the collagen matrix. In addition, we included an additional control condition consisting of composite hydrogel made of collagen and laminin functionalized beads (same as A_LAM) that did not undergo fiber alignment via magnetic field (hereafter referred to as LAM), enabling us to single out the topographical effects of fiber alignment on cell functions.

4.2.5 iPSCs conversion into NSCs

Mouse iPSCs (Alstem, #IPS02m) were expanded on a mitomycin-treated mouse embryonic fibroblasts (MEFs) layer in growth media consisting in knockout DMEM (Gibco, 108290180) supplemented with 20% knockout serum replacement (Gibco, N10828028), 1% GlutaMAX (Gibco, 35050-061), 1% pen/strep (Gibco, 15070063), 1% nonessential amino acids (Gibco, 11140-050), 0.1 mM 2-mercaptoethanol (Sigma, M3148), and 1000U/ml leukemia inhibitor factor (LIF, Gibco, PMC9484). Once the colonies were formed, the cells were transferred onto

a gelatin (0.1% w/v) coated 100mm tissue culture dish to eliminate the iMEFs. The iPSCs were allowed to recreate colonies and were expanded for at least 3 passages.

Then, iPSCs were plated onto gelatin-coated 6-well tissue culture plate at a density of 8×10^4 cells/well and cultured in induction medium composed of a 1:1 mixture of DMEM/F12 and Neurobasal supplemented with 2% B27 (Invitrogen). Cells were maintained in such medium for 12 days to induce neurogenic differentiation. Then, iNSCs were dissociated and expanded as single cells on uncoated 100 mm plates in Neurobasal medium supplemented with 1% N2 and 20 ng/ml of both human epidermal growth factor (EGF, Gibco, PHG0313) and human basic fibroblast growth factor (bFGF, Gibco, PHG0367). The cells were finally passaged 2-3 times to establish the line and stored in expansion medium supplemented with 10% dimethyl sulfoxide (DMSO). To confirm the successful neural induction, iNSCs were cultivated on laminin and poly-D-lysine coated coverslips for 24h, stained with nestin and b-III- tubulin and observed under the confocal microscope.

The different steps involved in iPSCs conversion into NSCs and the staining of NSCs final stage can be seen in the Appendix section (**Figure S4.1, Appendix**).

4.2.6 NSCs culture

iNSCs suspension was mixed at a 1:1 volume ratio with the collagen solution to obtain a final collagen concentration of 1mg/ml. 10µL aliquots of the mixture (50 000 cells per well) were then seed in 96 glass-bottom well-plate previously coated with poly-D-lysine and laminin. The collagen alignment was performed following the same procedure described above (see Section 4.2.2). Once the complete polymerization of collagen was achieved, differentiation media consisting of Neurobasal medium supplemented with 1% pen/strep, 1% GlutaMAX, 2% B27, 1% N2, 10 ng/ml bFGF, 20 ng/ml BDNF (PeproTech, 450-02), and 1 mM valproic acid (Sigma Aldrich) was added to each sample. The media was changed every other day.

4.2.7 Cytotoxicity evaluation

Invitrogen™ LIVE/DEAD™ Viability/Cytotoxicity Kit (Catalog number: L3224) was employed to assess the potential cytotoxic effects of paramagnetic beads on NSCs viability. Briefly, at DIV1 and 3, the sample were washed with PBS1X prior to incubation with the staining solution consisting of 2 µM calcein (Component A), 4 µM ethidium homodimer-1 (Component B) that was complemented with Hoechst 33342 (ThermoFisher, R37605) for total cell counting. The samples were incubated for 30 min at 37C and imaged on LSM880 AxioObserverZ1 confocal microscope through a Plan-Apochromat 20X objective (NA = 0.8, Zeiss). The multi-channel z-stack images were successively processed in Fiji and the number of dead cells was calculated as the ratio between ethidium homodimer-1 positive cells and Hoechst 33342.

4.2.8 Presto blue assay

A resazurin-based PrestoBlue microplate assay was used to assess cell viability at specific time points. Briefly, a fresh 10% dilution of stock PrestoBlue (ThermoFisher, A13262) in the cell-specific culture media is prewarmed to 37°C. The original cell culture media were removed from the experimental 96 well plate and replaced with 100µL PrestoBlue solution. The media were transferred to fresh 96-well F-bottom plates after incubation at 37°C for 60 minutes, and the absorbance was determined using the BioTek Synergy H1 microplate reader (Agilent) with the ex-wavelength and e-wavelength at 570 nm and 600 nm respectively.

4.2.9 Immunofluorescence analysis

At 1, 2 and 7 DIV, the samples were fixed in fresh 4% paraformaldehyde (PFA) at room temperature for 2 h. Fixed samples were permeabilized with 0.25% Triton-X100 (Sigma-Aldrich, #11332481001) and blocked with 5% horse serum (ThermoFisher, #31874) overnight at 4 °C. Samples were successively incubated with primary antibodies for 24 h at 4 °C, rinsed for a minimum of 5 times with blocking buffer, and lastly incubated overnight at 4 °C with donkey secondary antibodies. The details and working dilutions of primary and secondary antibodies are listed in **Table 4.1**. After 5 rinses, the nuclei were stained with 4-6-diamidino-2-phenylindole-dihydrochloride (DAPI) for 4 h at room temperature.

Vinculin-based analysis of focal adhesion

Samples fixed at 1DIV, were employed to evaluate the adhesion of NSCs to the different constructs. Focal adhesion structures were classified into focal complexes (FC) and focal adhesion (FA) based on their size. The small FC (< 2 μm) are primary cell–ECM adhesion structures at the cell periphery, which either disassemble rapidly or mature into larger FAs (2–5 μm).[370] To this end, Samples were imaged on LSM800 AxioObserverZ1 confocal microscope through a Plan-Apochromat 40X oil objective (NA = 1.3, Zeiss). The multi-channel z-stack images were successively processed in FIJI for background subtraction and the generation of a maximum projection. Particle analysis plug in was then employed to quantify the size and the number of FCs and FAs.

Considering the significantly higher cytotoxicity and consequently reduced metabolic activity, we opted to exclude the COOH condition from the following cell culture work.

Evaluation of early neuronal differentiation

Samples fixed at 2 DIV, were employed to investigate the differentiation stage of NSCs cultured within the different conditions. Samples were imaged on LSM800 AxioObserverZ1 confocal microscope through a Plan-Apochromat 20X objective (NA = 0.8, Zeiss). Particle

analysis plug in was employed to extract the average number of cells positive for NeuroD1and the average nuclear expression of active-YAP1.

NSCs orientation and morphological analysis

Samples fixed at 7 DIV we employed to evaluate NSCs orientation with respect to the preferential direction of collagen fibers following magnetic field application. To this end, samples were stained with Calretinin and β-III tubulin and imaged on LSM800 AxioObserverZ1 confocal microscope through a Plan-Apochromat 20X objective (NA = 0.8, Zeiss). The cellular orientation angle was manually extracted on ZenLite 3.8 software. A minimum of 100 cells per condition and 5 samples per condition were considered.

Finally, we performed a morphological analysis mainly focusing on neurites elongation and spreading. To this end, an automated Strahler analysis (ImageJ Neurite Tracer plugin) was applied to defined 250 µm square ROIs, enabling the quantification of average branch length and average longest branch length.

Table 4.1: List of primary and secondary antibodies, with their working dilution, used in this study.

Primary antibody	Dilution	Secondary antibody	Dilution
β III-tubulin (Abcam, ab78078)	1:1000	anti-goat Alexa 488	1:500
Vinculin (SigmaAldrich, V9264)	1:400	anti-rat Alexa 555	1:500
Ki-67 (ThermoFisher, 14-569)	1:250	anti-mouse Alexa 594	1:500
NeuroD1(ThermoFisher, 1PA5-78075)	1:500	anti-rabbit Alexa 647	1:500
HDAC1 (SantaCruz, sc81598	1:200		
Nestin (Abcam, ab105389)	1:500		
Calretinin (Abcam, ab92341)	1:500		
YAP1 (proteintech, 3A7A9)	1:1000		
Active-YAP1 (Abcam, ab205270)	1:1000		

4.2.10 Western blot

Cells cultured in COL, LAM and A_LAM conditions were harvested into cold RIPA buffer by scraping and sonication of the collagen matrix. The total protein concentration of the cell lysates was determined by BCA assay (Pierce™ BCA Protein Assay Kit, # 23225,

ThermoFisher). The lysates were successively boiled for 10 min at 95 °C in the sample loading buffer. The proteins were electrophoretically resolved on a 10% SDS-PAGE gel at 100 V. Resolved proteins were transferred to PVDF membranes for 30 min at 20 V using Transblot Turbo (BioRad, USA). After washing, the membranes were blocked in 5% BSA for 1 h at room temperature. Subsequently, the PVDF membranes were blotted with primary antibodies overnight at 4 °C, washed 5 times with TBST buffer and incubated 2h at room temperature with peroxidase-conjugated secondary antibodies. After washing, the membranes were imaged by a ChemiDoc XRS+ (BioRad) system and the bands were analyzed with the ImageJ software.

4.2.11 Statistical analysis

Data are reported as mean ± standard deviation (SD) or standard error of the mean (SEM) from at least 3 separate experiments. Data were plotted with GraphPad software, version 8.0. The normality of the distribution was assayed by different tests, such as Pearson normality test and Shapiro-Wilk normality test. For normally distributed data, one-way, two-way analysis of variance (ANOVA) test followed by Tukey's Honestly Significant Difference (HSD) *post hoc* test was used. For non-normally distributed data, Kolmogorov–Smirnov test analyses were carried out. Significance was set at $p \leq 0.05$.

4.3 RESULTS AND DISCUSSION

4.3.1 Optimization of collagen alignment

In this study, we aimed to create a robust and reproducible method to produce aligned collagen hydrogels via the integration of paramagnetic micro-beads and the application of a remote magnetic field. To reach this goal, we focused on the functionalization of the beads with different biomolecules and the optimization of the magnetic field application timing via the in-depth study of collagen fibrillogenesis. We selected paramagnetic microbeads with a

diameter of 1 µm and we tested concentrations ranging from 0.5 to 10%vol. In accordance with several reported studies,[371,368,369] our investigation revealed that increasing the beads concentration beyond 1%vol did not elicit a significant enhancement of the resulting collagen fibers. For this reason, the results presented below adopt the same bead concentration of 1%vol. In addition, we observed that the majority of the studies reported an enhanced alignment of collagen fibers attained by the use of either carboxylic or streptavidin functionalized beads when compared to non-functionalized beads.[368,371] For this reason, we employed COOH-functionalized beads that enable us to covalently bond, via EDC-NHS coupling, different biomolecules. We opted to functionalize the beads with streptavidin due to the notable alignment outcomes previously documented by others.[371] In addition, we conducted laminin functionalization of the beads. We hypothesized that, given its crucial role in facilitating anchor points for neuronal cell adhesion and spreading,[104,105,108] along with its established native interactions with collagen in the extracellular matrix (ECM)[372] laminin-functionalized beads might not only promote superior collagen alignment but also foster a biologically advantageous microenvironment. **Figure 4.1A** illustrates representative confocal images of the paramagnetic beads labelled with NHS ester conjugated with Alexa Fluor 555. It is evident that the NHS ester groups reacted with the primary amines present in both streptavidin and laminin, thus confirming the successful functionalization of COOH- beads via EDC-NHS coupling.

Our investigation cast new light on the importance of the timing of application of the magnetic field in determining the resulting collagen alignment. While several studies reported the alignment obtained via the instantaneous application of the magnetic field, in this study we performed an in-depth analysis of the fibrillogenesis dynamics of collagen and we tested different timing of magnetic field application, uncovering the great influence of such variable. **Figure 4.1B** shows a representative turbidity curve in the first hour of collagen fibrillogenesis. It is possible to discern three separate phases: i) the lag phase during which collagen monomer

starts to form nucleation sites, **ii**) a fast growth phase during which the nuclei develop into fibrillar structure and iii) a plateau phase where the monomers are depleted. [373,374]

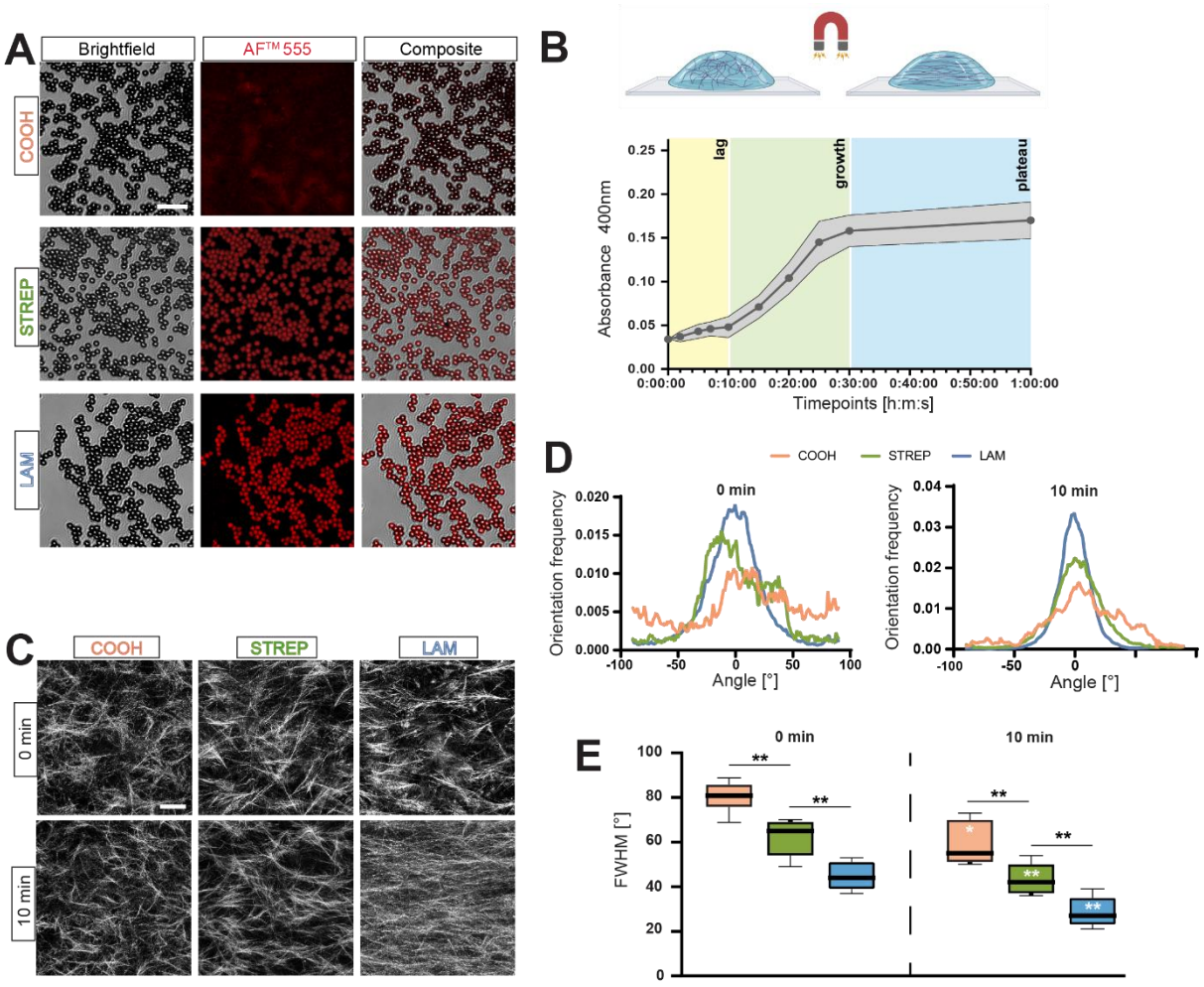

Figure 4.1: Optimization of collagen hydrogel alignment via remote magnetic field. (A) Paramagnetic beads were introduced in the collagen solution either in their pristine state (COOH) or after EDC-NHS coupling with streptavidin or laminin. The successful functionalization of the beads with the biomolecules was shown via NHS ester labelling. Scale bar: 5 µm (B) Representative turbidity curve during collagen fibrillogenesis that was used to pick different timepoints at which applying the remote magnetic field to align collagen fibers. Scale bar: 25 µm. (C) Representative confocal images of collagen using pristine (*left*), streptavidin- (*center*) and laminin- (*right*) functionalized beads. The magnetic field was applied either at the onset of fibrillogenesis (t=0min, *top*) or at the lag/growth transition phase (t=10min, *bottom*). Scale bar: 100 µm. (D) Orientation frequency distribution obtained for the two timing of magnetic field application. (E) FWHM values obtained from Gaussian fitting of the frequency distributions.

Based on the turbidity curve of collagen, we identified different timepoints to apply the magnetic field. Specifically, we chose to apply the magnetic field at the beginning of the fibrillogenesis (t=0 min) and at the lag/growth phase transition (t=10 min).

Representative images of the obtained degree of collagen alignment obtained for different timing of magnetic field application are shown in **Figure 4.1C**. It is evident that the application of the magnetic field in concomitance with the lag/growth phase compared to the beginning of fibrillogenesis led to enhanced collagen fibers alignment for the different bead functionalizations tested (*left to right*). **Figure 4.1D** shows the fiber orientation frequencies for both timing of magnetic field application. The distributions were fitted to a Gaussian curve to extract the full width at half maximum (FWHM), as an indicator of distribution spreading and dispersion (**Figure 4.1E**). From such analysis, we found that the FWHM values significantly decreased for all functionalization tested when the magnetic field was applied after 10 minutes compared to an instantaneous application of the magnetic field. In particular, for both timing of magnetic field application, we found that laminin-functionalized beads displayed the lowest FWHM values compared to the other functionalization tested (i.e., pristine and streptavidin). The lowest FWHM values were found for magnetic induction at t=10 (at the lag/growth phase transition) with laminin-functionalized beads.

In accordance with the presented results, we chose this condition (A_LAM) as the aligned experimental condition to conduct the following cell culture experiments. For completeness of the study, this condition will be compared to several controls. Specifically, pristine collagen (COL) will be used as a control condition as it will enable us to single out the effect elicited by the introduction of the pristine beads in the collagen matrix (COOH). The effects of laminin-functionalization of the beads will be pinpointed by the condition LAM. This condition will also provide a great control to point out the effect of aligned topography in the experimental

condition A_LAM. In fact, as shown in **Figure S4.1C** we did not detect any significant differences in stiffness between LAM and A_LAM conditions.

4.3.2 Cytotoxicity assays

When designing a novel biomaterial, it is important to comprehensively evaluate its potential cytotoxic effects on cell survival. In this study, we employed mouse iPSCs-derived NSCs. We evaluated NSCs survival at 1 and 3DIV through immunofluorescence imaging.

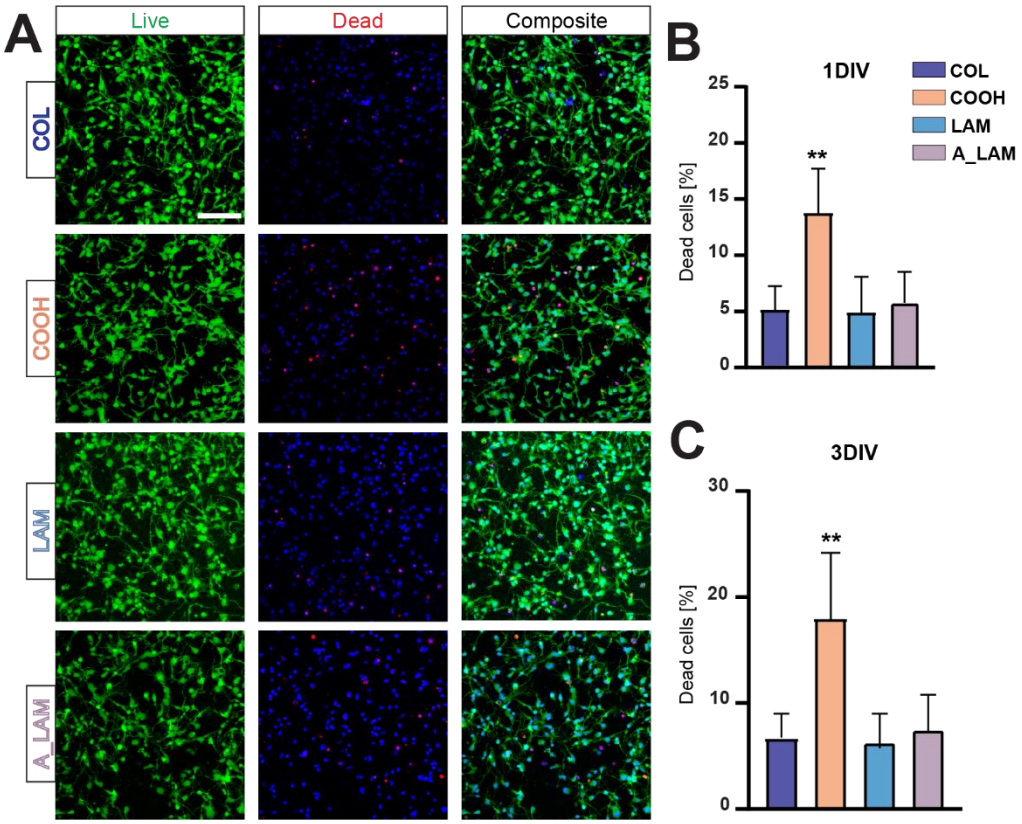

Figure 4.2: Live/dead assay performed on NSCs at 1 and 3DIV. (A) Representative confocal images of NSCs seeded into the different conditions and stained with live/dead assay kit at 1DIV. The aligned experimental condition (A_LAM) was compared to its not aligned counterpart (LAM), to collagen hydrogel supplemented with pristine beads (COOH) and standalone collagen hydrogel (COL). Scale bar: 150 µm. (B) Percentage of dead (ethidium homodimer-1 positive) cells after 1 DIV and 3 DIV (C).

Figure 4.2A shows representative images of NSCs stained with live/dead assay kit seeded on the different conditions tested at 1 DIV. As can be seen in **Figure 4.2B**, COOH condition

displayed a mean percentage of dead cells significantly higher compared to the other tested conditions. While COL, LAM and A_LAM, displayed a mean percentage of dead cells of respectively 4.9, 4.7 and 5.4 %, COOH exhibited a dead cell percentage of 13.7 %. The same trend was also depicted at 3 DIV (**Figure 4.2C**). In fact, both A_LAM (7.4 %) and LAM (6.1 %) conditions displayed similar average values of dead cell percentages compared to COL (6.3 %), whereas COOH exhibited the highest values (18.2 %). This observation, previously noted by other researchers,[375,376] led us to hypothesize that the COOH functional groups of the paramagnetic beads might engage in strong interactions that result in cellular membrane damage and compromised integrity. Compared to pristine beads (COOH), laminin-functionalized beads (both LAM and A_LAM) foster beneficial interactions that facilitate a more specific and controlled cell-bead interaction, likely reducing potential membrane damages and ultimately ensuring a more sustained cellular viability.

4.3.3 Proliferation and adhesion analysis

To evaluate the metabolic activity of NSCs seeded in the different conditions, we performed Presto blue assay. As shown in **Figure 4.3B**, LAM and A_LAM conditions showcased a significantly higher metabolic activity during the first 24h of culture when compared to COOH and COL. In particular, the absorbance readings (normalized with respect to COL) captured at 2h for LAM and A_LAM were 1.28 and 1.23, while COOH was characterized by an average value of 0.97. Similar trends were also observed at 6h and 24h, with LAM and A_LAM normalized absorbance values further increasing to respectively 1.67 and 1.78 at 6h, and to 1.75 and 1.64 at 24h. In addition, we noticed that the metabolic activity of COOH was significantly decreased at 24h, with a normalized absorbance value of 0.78. This data aligns with the previously discussed cytotoxicity analysis, illustrating a rise in cell death rates, which is reflected in the diminished overall metabolic activity of NSCs seeded into COOH construct.

At 48h, we noticed that A_LAM condition exhibited a significant decrease in metabolic activity, with an average absorbance value that was significantly lower than COOH and LAM.

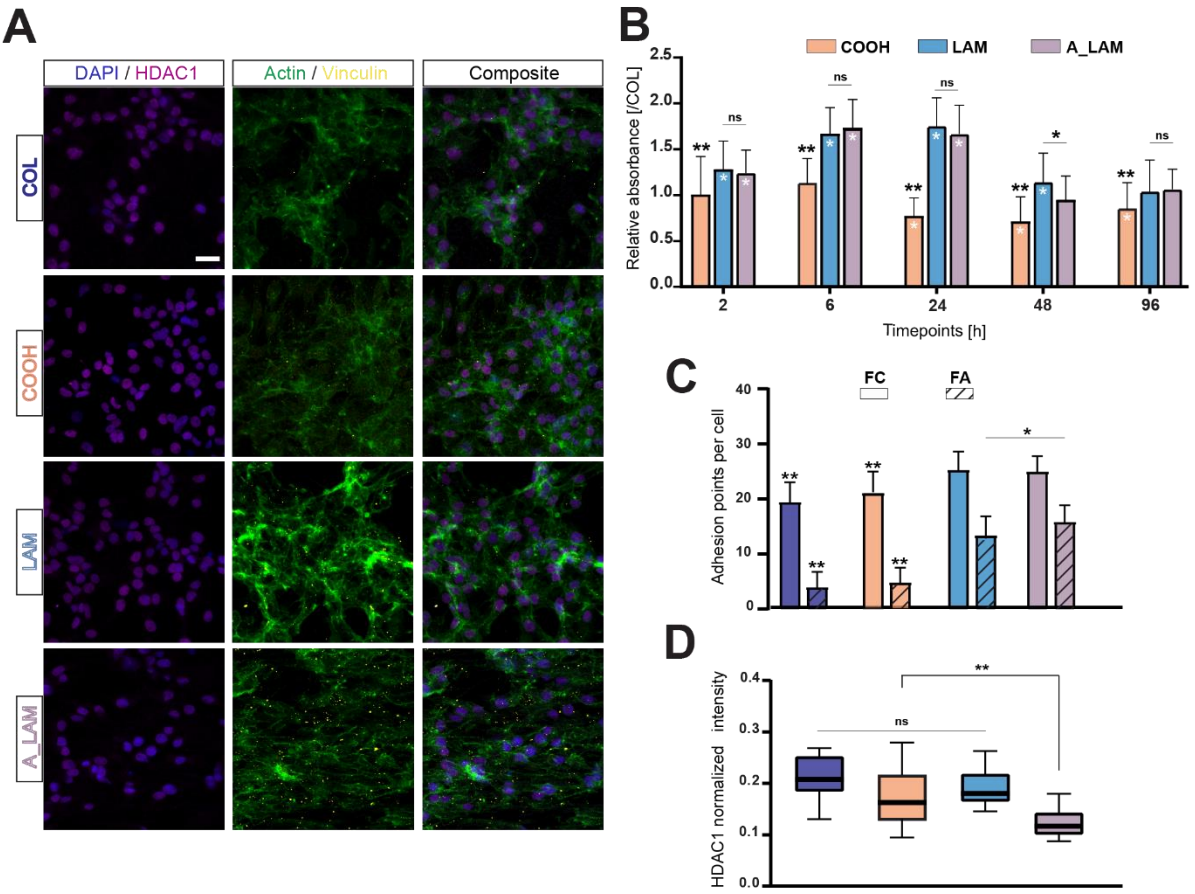

Figure 4.3: Proliferation assay and adhesion analysis of NSCs. (A) Representative confocal images of NSCs stained for HDAC1 (*magenta*), actin (*green*) and vinculin (*yellow*) 1DIV. Scale bar: 20 µm. (B) Relative metabolic activity observed over 96 hours of culture in NSCs seeded onto various scaffolds. White asterisks highlight significant differences with COL condition (C) Average adhesion points found for the different conditions. According to their size, adhesion points were categorized as either focal complexes (< 2 µm, FC) or focal adhesions (> 2 µm, FA) (D) Average normalized HDAC1 expression found for the different conditions tested,

Specifically, the normalized mean absorbance value for A_LAM was observed to be 0.92. In comparison, LAM and COOH displayed values of 1.13 and 0.69, respectively. This sudden shift in the metabolic trajectory observed in the A_LAM setup might be indicative of an accelerated initiation of neurogenic differentiation processes, potentially overtaking the proliferative phase of NSCs and ultimately impacting the overall absorbance readings. In the

next section, we will delve deeper into investigating the early differentiation stages of NSCs seeded into the different hydrogels.

Finally, at 96h, both A_LAM (1.08) and LAM (1.04) conditions displayed a metabolic activity comparable to COL, while COOH group data (0.77) confirmed the overall lower metabolic activity that likely results from an increased cytotoxicity.

In light of the interesting metabolic trends showcased by NSCs in the first 24h, we performed a vinculin staining of the samples to gain more insights on the integrin-mediated NSCs adhesion when seeded within the different conditions. Specifically, to obtain a deeper understanding of the underlying cell-substrate interactions, we distinguished between focal complexes (adhesion points smaller than 2 µm) and focal adhesions (adhesion points larger than 2 µm). Focal complexes, which are smaller and more transient, usually appear in the early stages of cell adhesion, reflecting initial cellular response to the surroundings. Conversely, the larger focal adhesions indicate well-established and enduring cell-substrate connections and have been shown to play a significant role in cellular mechanotranduction.[377–379] The resulting confocal images, depicted in **Figure 4.3A**, underlined a significant augmentation in the overall NSCs vinculin expression levels (**Figure 4.3C**) when seeded within LAM and A_LAM conditions as compared to the standalone COL and COOH. Specifically, we registered a significant increase in the number of focal complexes in both LAM (25.4) and A_LAM (24.9) conditions when compared to COL (19.3) and COOH (20.7), reinforcing the pivotal role of laminin in facilitating robust cell-matrix interactions already reported by many. [114–116] Interestingly, NSCs embedded in the A_LAM (15.5) condition presented a significantly higher number of focal adhesions compared to LAM (14.7), potentially showcasing the synergistic benefits of laminin functionalization and collagen alignment in fostering optimal adhesion dynamics.[380]

The alignment of collagen not only elicited an increased number of focal adhesions but also differentially modulated the expression levels of HDAC1, a key regulator of gene expression and cellular signaling.[381] HDAC1, being a core component of the histone deacetylase complex, plays a critical role in gene expression regulation through the removal of acetyl groups from histones, leading to a more condensed and less transcriptionally active chromatin state. In this context, several studies have reported the potential role of HDAC1 in regulating, among others, the neuronal differentiation of stem cells and neural progenitors.[381–383] As shown in **Figure 4.3D**, the nuclear analysis revealed a significant decrease in HDAC1 in A_LAM (0.12) when compared to LAM (0.19), COOH (0.17) and COL (0.21). This result suggests that the topographical rearrangement of collagen fibers in A_LAM might trigger a series of signaling pathways that ultimately led to an attenuated activity of HDAC1. A plausible explanation centers around the increased interaction displayed by A_LAM with integrin receptors, as evidenced by the elevated focal adhesion points (**Figure 4.3C**), offering a conceivable pathway influencing HDAC1 expression dynamics.[384,385] In addition, several studies have showcased the modulation of HDAC1 via specific physicochemical properties presented by the surrounding microenvironment. For instance, it was reported that specific surface micro-grooves could modulate the expression level of HDAC1 in mouse iPSCs.[386] Similarly, it has been shown that the level of HDAC1 in hMSCs was greatly modulated by the stiffness of polyacrylamide gels.[387]

4.3.4 Evaluation of early neuronal differentiation of NSCs

Considering the PrestoBlue results observed at the 48-hour mark and notably the significant reduction in the metabolic activity registered for the A_LAM group, we extended our investigation to determine the underlying cellular processes potentially in action. To this end, we employed immunofluorescence imaging and Western blot analyses to evaluate potential

differences in the expression levels of key markers representative of the diverse stages of NSCs' biological development, specifically focusing on proliferation (i.e., Ki67) and early neurogenic differentiation stage (i.e., NeuroD1) markers. **Figure 4.4A** illustrates representative nuclear staining of NSCs with Ki-67 and NeuroD1 for the different conditions tested.

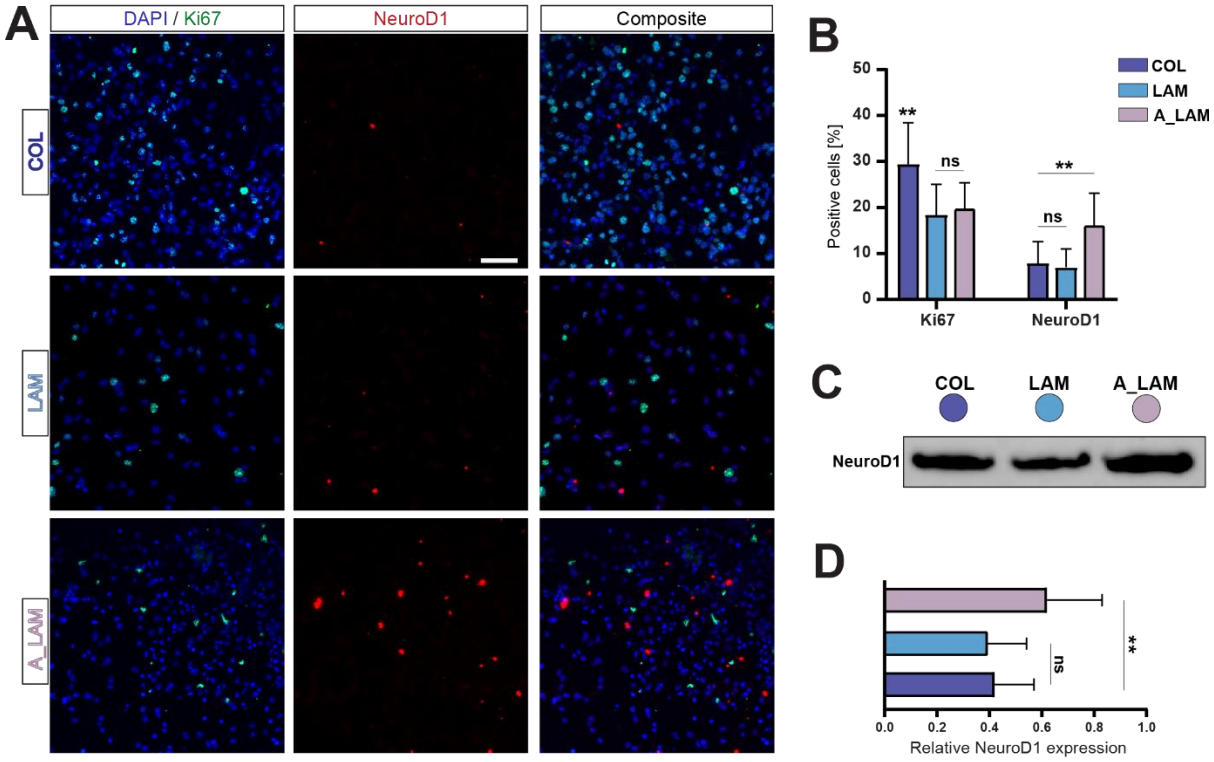

Figure 4.4: Early neuronal differentiation analysis. (A) Representative images of Ki67 *(green)* and NeuroD1 (*red*) expression levels in the different conditions tested. Scale bar: 50 µm (B) Average percentages of NSCs positive for Ki67 (*left*) and NeuroD1(*right*). (C) Western blot analysis of NeuroD1 expressions. (D) Quantification of NeuroD1 expression levels.

Nuclear analysis (**Figure 4.4B**) revealed that NSCs seeded into LAM (18.2 %) and A_LAM (19.7 %) displayed a lower average percentage of Ki-67 positive cells when compared to COL (28.7 %). On the other hand, the average percentage of NSCs positive for NeuroD1 was found to be significantly higher in A_LAM (17.3 %) when compared to both LAM (6.8 %) and COL (8.0 %) conditions. This trend was further corroborated by Western blot analyses (**Figure 4.4C-D**), where the A_LAM condition showcased a pronounced elevation in NeuroD1 expression

relative to the control groups, potentially hinting at an enhanced propensity for neurogenic differentiation. This finding suggests that the aligned structure of collagen fibers in A_LAM might be fostering a microenvironment conducive to early neuronal differentiation, a hypothesis that aligns with different studies reported in the literature that attribute a decisive role to biomaterial topography in guiding cellular differentiation paths.[57,64,66,67,71,74,365,368]

To further elucidate the mechanisms influencing the behavior of NSCs in the different conditions environments, we evaluate the expression levels of the Yes1-associated protein (YAP1) and its non-phosphorylated, active state. The Hippo signaling is in fact sensitive to mechanical stress experienced by the cells. The biomechanical regulation of Hippo signaling is revealed by the sensitivity of YAP1 localization to a variety of perturbations including the ECM stiffness, cell stretching, shear forces and topographical cues.[388–392] **Figure 4.5A** illustrates representative images of the NSCs expression levels of YAP1 and its activated (nuclear) form. Nuclear analysis (**Figure 4.5B**) revealed that laminin-functionalization determined a lower expression of nuclear/active-YAP1 compared to standalone collagen. In fact, the average nuclear expression of YAP significantly decreased from 0.37 in COL, to 0.31 and 0.25 for LAM and A_LAM, respectively.

In addition, our results pointed out the significant influence of aligned topography in the expression levels of active-YAP1, as we found a statistically significant difference between LAM and A_LAM. Quantitative Western blot analysis (**Figure 4.5C**) corroborated the IF imaging results. The average expression of active-YAP1 normalized by total YAP1 was significantly decreased in the A_LAM group **(Figure 4.5D**). Specifically, the average value significantly decreased from 0.23 (COL) and 0.19 (LAM) of control conditions to 0.10 for the experimental A_LAM condition.

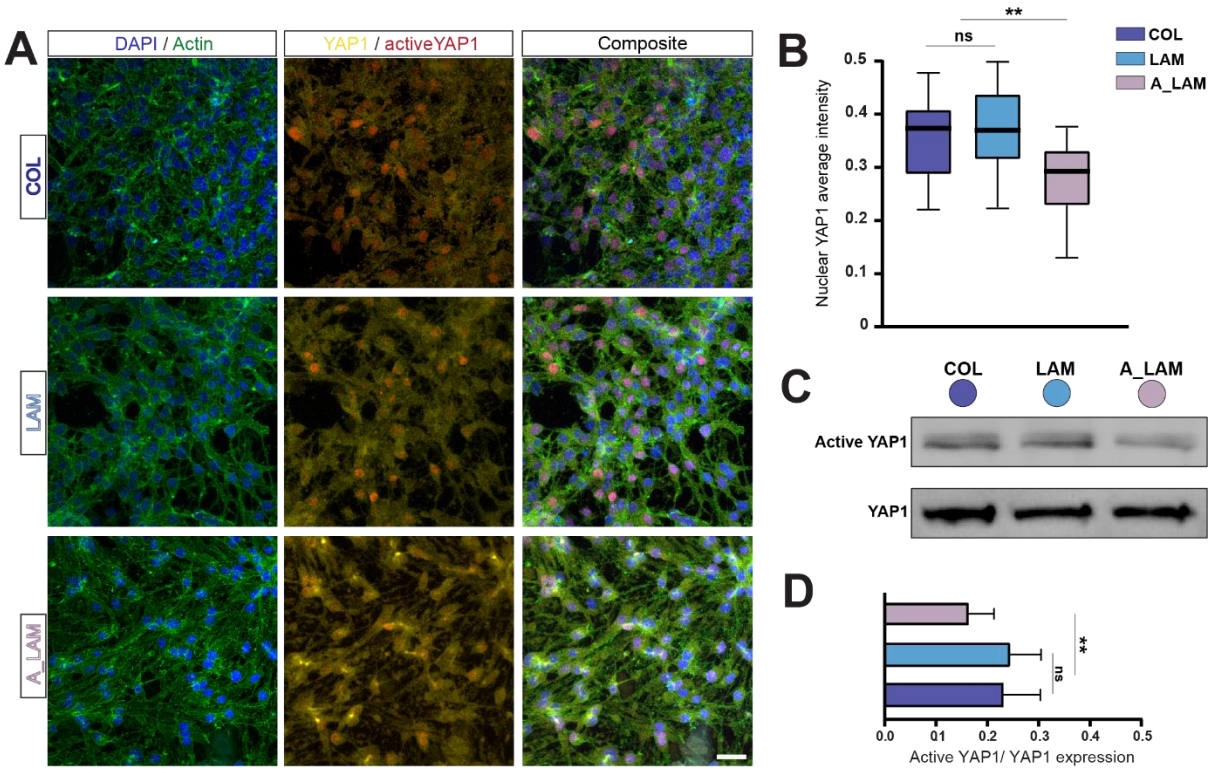

Figure 4.5: Expression of YAP1 and active-YAP1 throughout the different conditions. (A) Representative images of YAP1 (*yellow*) and active-YAP1 (*red*) expression levels in the different conditions tested. Cell bodies were stained with actin (*green*). Scale bar: 25 µm. (B) Active-YAP1average intensity expression levels for the different conditions tested. (C) Western blot analysis of YAP1 and active-YAP1 expressions. (D) Relative quantification of active-YAP1 normalized by the total expression of YAP1.

Taken together, our findings revealed that the unique physicochemical properties of A_LAM play a pivotal role in determining an early onset for the neurogenic differentiation of NSCs. The significant downregulation of HDAC1 expression at 24h, aligns with the reduced proliferation rates of A_LAM. As a known regulator of cellular differentiation processes, the reduced HDAC1 expression suggests that A_LAM offers a conducive microenvironment for neurogenic differentiation, a consideration that was further confirmed by the upregulation of the early neurogenic differentiation marker NeuroD1.

In parallel, we detected a significant modulation in the Hippo signaling pathway, particularly regarding the activity of its main effector, YAP1, in its non-phosphorylated and thus active state. This transcriptional co-activator has recently gained significant attention for

its pivotal role in mechano-transduction signaling and has been reported to be highly sensitive to the physicochemical properties presented by the ECM. The diminished active-YAP1 level found for A_LAM, suggests that the anisotropic orientation of collagen fibers could enhance the transition toward an NSCs stage that fosters neuronal differentiation.

Consequently, the apparent synchronization in the activities of HDAC1 and the Hippo signaling pathway (i.e., active-YAP1) underlines a coordinated cellular response to the specific physicochemical environment offered by A_LAM condition, emphasizing a complex yet synergistic role in guiding the early neurogenic differentiation of NSCs.

4.3.5 Orientation and morphological analysis of NSCs

Many disorders affecting the nervous system entail the damage and deterioration of axonal tracts, which consist of highly organized and aligned bundles of axons. For this reason, it is important to develop biomaterials that can foster an oriented axonal growth that will ultimately aid in repairing the injured site.[393,394] For this reason, we interrogated the ability of A_LAM to preferentially orient NSCs. **Figure 4.6A** displays representative images of NSCs after 7 DIV. It is evident how the anisotropic fiber distribution of A_LAM guided a preferential orientation of NSCs toward the direction of the collagen fibers. By extracting the angle frequency distributions of the different conditions (**Figure 4.6B**), we observed that A_LAM induced a substantial increase in the proportion of NSCs aligning within an angle deviation of ± 22.5° relative to the primary direction of the fiber alignment. Specifically, our data indicated that 55% of NSCs embedded within A_LAM were oriented within this angular range, highlighting a strong NSCs tendency to preferentially orient toward the inherent fiber orientation of A_LAM. Not surprisingly, the alignment propensity was notably decreased for COLL and LAM conditions, where the proportion of NSCs exhibiting alignment within the ± 22.5° range was 42% and 39%, respectively.

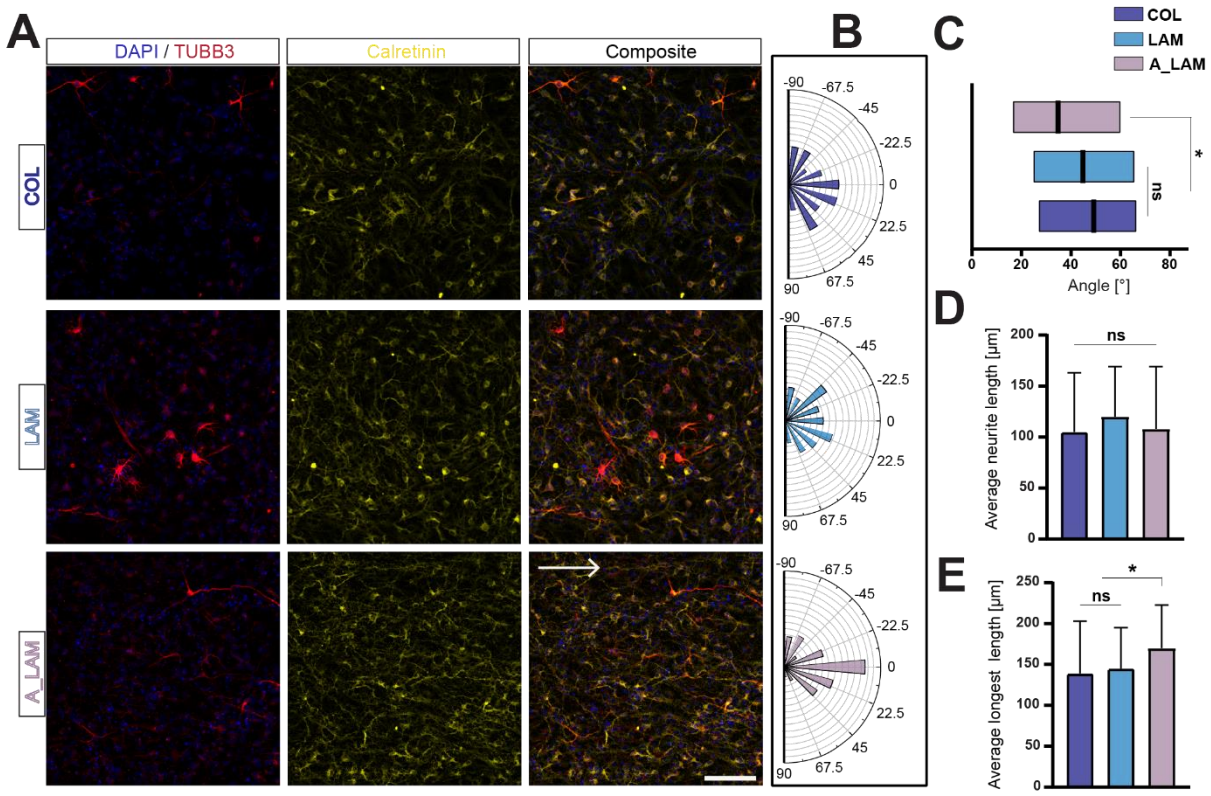

Figure 4.6: Orientation and morphological analysis of NSCs. (A) Representative images of NSCs expression of β-III tubulin (*red*) and calretinin *(yellow*) at 7DIV for the different conditions. The white arrow indicates the main fiber orientation after magnetic field application. Scale bar: 150 µm. (B) Frequency angle distribution found for NSCs in relation to the main collagen fibers orientation. (C) Average NSCs orientation angle in relation to the main collagen fibers orientation. (D) Average length of neurites spreading from NSCs in the three conditions tested. (E) Average longest neurites length found across the three conditions tested.

The great efficiency of A_LAM in providing a supportive environment for NSCs aligned was also supported by the average orientation angle displayed by NSCs. As shown in **Figure 4.6C**, the A_LAM condition displayed the lowest average angle (27.5°) that was significantly lower when compared to COL (44.7°) and LAM (42.3°). Finally, we performed a morphological investigation of NSCs namely examining neurites extension.

Figure 4.6D shows the average neurite length found across the three conditions. Despite no significant differences being observed for the average neurite length, interestingly A_LAM showed a significantly higher average longest neurite length. As shown in Figure **4.6E**, the average longest neurite length found for A_LAM (191 µm) was significantly higher when

compared to both control conditions (138 µm and 147 µm for COL and LAM, respectively). This result suggests that the distinctive anisotropic orientation of collagen fibers present in A_LAM provides a conducive environment for extended neurite formation. In the context of neuronal regeneration, such elongated neurite morphology has great implications. In fact, it has been shown that such morphological signature can elicit improved cellular communication and signal transduction,[395,396] possibly enhancing the integration of these newly formed neuronal networks within the existing neural framework.[396,397]

4.4 CONCLUSION

In conclusion, this study optimized a collagen-based hydrogel intended for neuronal regeneration that can be aligned *in situ* via the application of a remote magnetic field. While this approach has already been investigated by others, the distinct contribution of this study relies on the use of laminin-functionalized paramagnetic beads, coupled with the optimization of the timing of magnetic induction. Our finding highlighted the significant impact that the timing of the magnetic field application had on the overall collagen fibers alignment, demonstrating that the best alignment was achieved when the magnetic field was initiated in concomitance with the lag/growth phase transition of collagen fibrillogenesis.

When populated with mouse iPSCs-induced NSCs, the novel hydrogels demonstrated low *in vitro* cytotoxicity and provided a suitable environment for the establishment of mature focal adhesions. In addition, within 48h from magnetic induction, the aligned construct demonstrated the ability to expedite the neurogenic differentiation of NSCs via enhanced activation of the Hippo signaling pathway. Lastly, NSCs embedded with the aligned scaffold showcased a preferential orientation toward the collagen fibers direction and an increased average longest neurite length.

Taken together, our study highlights the advantageous properties of the newly developed injectable collagen hydrogel, which coupled with the possibility to preferentially guide its orientation remotely, make it a promising candidate for applications in neuronal regeneration.

5. THESIS' GENERAL CONCLUSIONS

The work presented in this thesis demonstrates that:

(Chapter 2) Microgroove patterning and chemical crosslinking of electrodeposited chitosan films modulate several pivotal cellular functions, including cell morphology, orientation and differentiation.

(Chapter 3) The integration of GlyCNDs within a collagen hydrogel markedly enhanced the neuronal differentiation, the neurite outgrowth and the electrophysiological maturation of mouse iPSCs-derived spheroids.

(Chapter 4) Collagen fibers alignment via remote magnetic field greatly depends on the timing of magnetic induction and on the paramagnetic-beads functionalization. The novel anisotropically oriented hydrogel provides a beneficial environment for early neurogenic differentiation and for the preferential orientation of mouse iPSCs-derived NSCs.

Taken together, these studies present novel engineered biomaterials with instructive physicochemical properties that aim at eliciting beneficial neuronal responses in the context of neural tissue engineering applications. The reported findings on the structure-functions relationship governing cell-substrate interactions are posed to offer valuable insights for the development of future biomaterials.

6. APPENDIX

6.1 CHAPTER2: SUPPLEMENTARY INFORMATION

6.1.1 Raman Spectroscopy

Materials and Methods: Infrared spectroscopic analysis was complemented by capitalizing on the Raman module of the alpha300 RSA system (WITec, Germany). Single spectra were collected from three randomly selected regions of each sample using a 785 nm Toptica XTRA Laser (Germany, 40 mW, acquisition time = 0.2 sec) through a 50X objective (EC Epiplan NEOFLUAR, NA = 0.9, Zeiss). Spectra were composed of 10 accumulations at an integration time of 30 s and a laser power at the objective of 25 mW. Analysis of the Raman bands in the 700–1900 cm^{-1} region was carried out in OriginPro following the same processing described for the FT-IR analysis, with the additional use of the Savitzky-Golay smoothing filter before baseline subtraction. Raman peak assignment was carried out according to previous literature (**Table S1.1**).

Results and Discussion: Spectra extracted from both treated samples showed an evident increase of the C-C stretching band at 934 cm^{-1} (R1) suggesting the presence of CA molecules. **Figure S1.1B** (*left*) shows the normalized area increase relative to this band, which varied from an average of 1.1 for the NC condition to 2.2 and 2.5 for the C165 and C190 samples, respectively.

Table S2.1: Raman vibrational modes.

RAMAN PEAK ASSIGNMENT		
Ref.	**Position (cm^{-1})**	**Description**
R1	934 ± 3	C-C (stretch.), C-H (def. out plane)
R2	1049 ± 1	C-O (stretch.), C-CH_2 (stretch.)
R3	1151 ± 3	C-O-C (stretch.)
R4	1261 ± 2	C-H (def. in plane), C-O (stretch.)
R5	1328 ± 3	C-N (stretch.); [*Amide III*]
R6	1371 ± 1	CH_3 (def. in plane), CH_2 (def. in plane)
R7	1411 ± 2	C-H (def. sym.)
R8	1592 ± 2	N-H; [*Amide II*]
R9	1656 ± 4	C=O; [*Amide I*]

Furthermore, the creation of covalent bonds due to the crosslinking process was demonstrated by the significant increase relative to the normalized area of the band at 1328 cm^{-1} associated with the C-N stretching vibration of the Amide III (R5), which varied from 1.8 in NC samples to 4.3 and 4.1 for the C165 and C190 conditions, respectively (**Figure S1.1B,** *right*). The combined use of FTIR and Raman spectroscopy provided consistent information regarding the chemical arrangement resulting from the CA-based crosslinking process employed in this work. Both FTIR and Raman analysis of treated samples reflected the presence of CA molecules as well as the formation of new C-N covalent bonding, thus providing significant evidence to validate the successful crosslinking process.

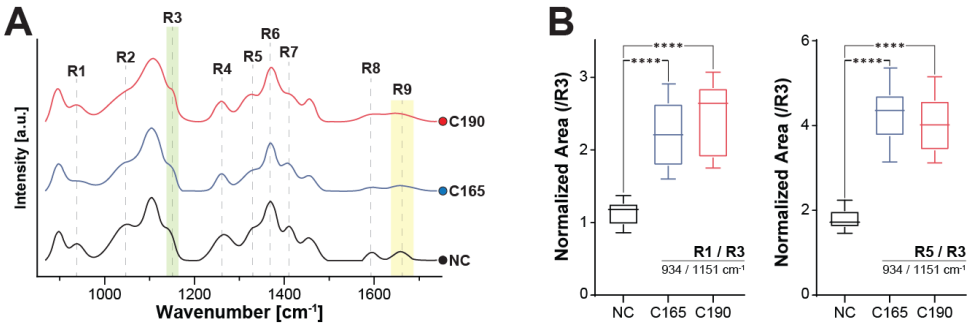

Figure S2.1: Raman analysis of chitosan substrates. (A) Representative Raman spectra for as-deposited (NC) and crosslinked chitosan treated at 165 °C (C165) and 190 °C (C190). For clarity, each band was labeled with a code ranging from R1 to R9, reported in Table S1. (B) Quantification of R1/R3 and R5/R3 peak area ratios obtained from Raman spectra.

6.1.2 Supplementary Images

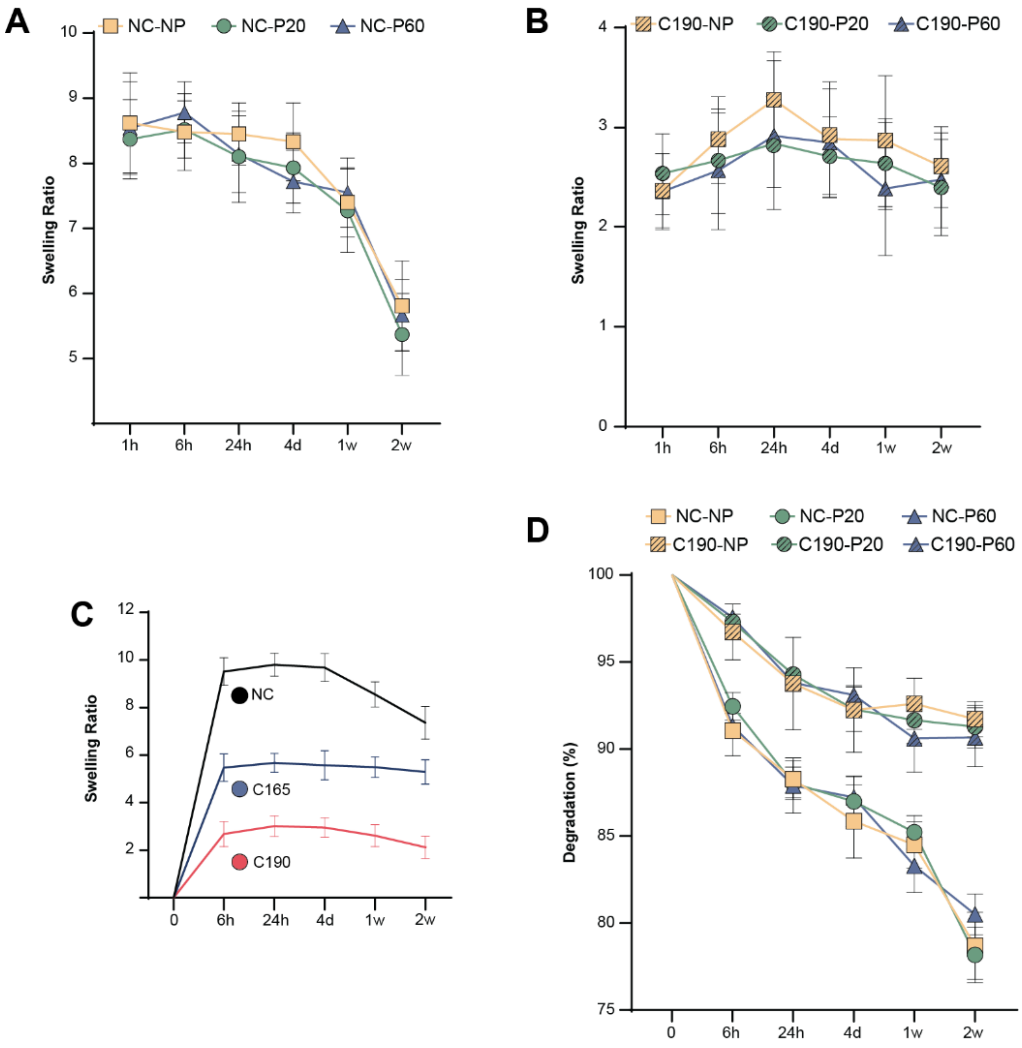

Figure S2.2: Influence of surface topography on the swelling behavior of chitosan substrates. **(**A) Swelling behavior of non-crosslinked chitosan samples with different surface micro-topographies. (B) Swelling behavior of CA-crosslinked samples with different surface micro-topographies. (C) Adjusted swelling behavior to account for mass loss. (D) Degradation profiles of both non-crosslinked and CA-treated chitosan accounting for all topography.

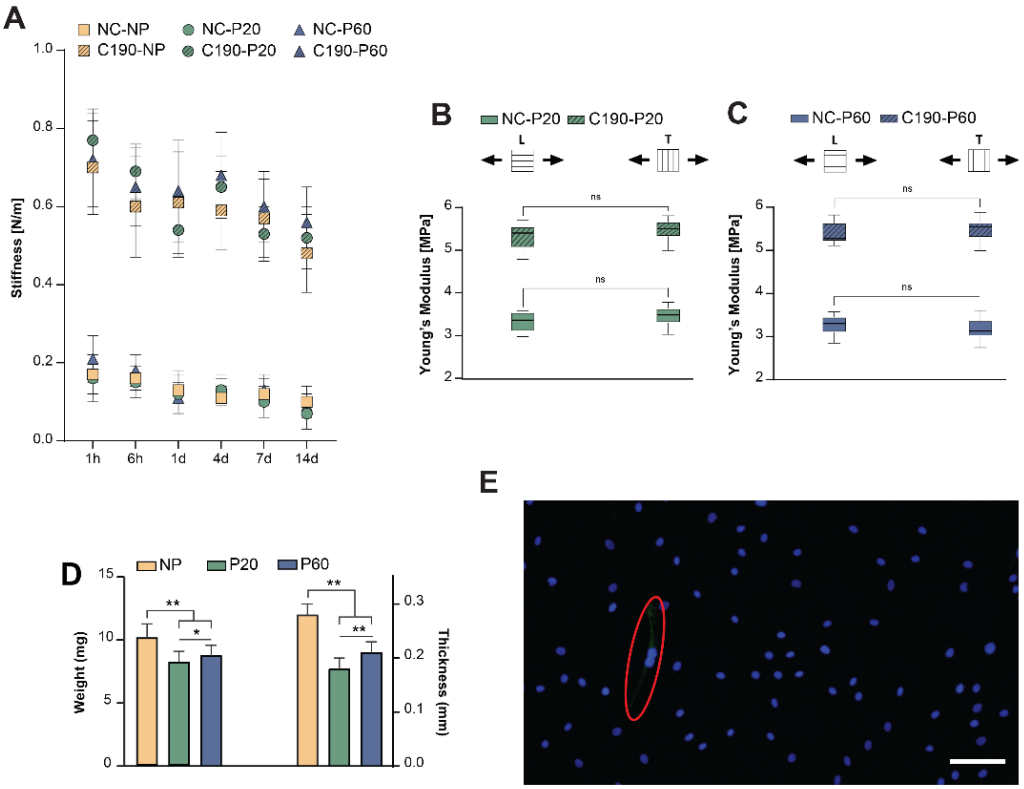

Figure S2.3: Influence of surface topography on the micro-stiffness of chitosan substrates detected via AFM indentation. **(**A) Surface stiffness obtained via AFM indentations of un-patterned (NP) and patterned (P20/P60) substrates, both as-deposited (NC) and CA-crosslinked at 190 □C (C190). (B) P20 average Young's modulus for both non-crosslinked (*bottom*) and crosslinked (*top*) conditions, obtained by applying longitudinal (*left*) and transversal (*right*) load during the axial testing. (C) P60 average Young's modulus for both non-crosslinked (*bottom*) and crosslinked (*top*) conditions, obtained by applying longitudinal (*left*) and transversal (*right*) load in axial testing. (D) Weight and thickness of electrodeposited chitosan films. E) hMSCs tubulin expression after 24h. Scale bar: 100 µm.

6.2 CHAPTER3: SUPPLEMENTARY INFORMATION

6.2.1 AFM indentation

Stiffness and Young's modulus were extracted from indentation curves performed on AFM module on an Alpha300 RSA system using a spherical silicon nitride tip with a precalibrated spring constant of 0.133 N m−1 and a diameter of 5 μm (Bruker, USA, MLCT-SPH-5UM, cantilever E). Indentations were carried out in PBS 1× to quantify the samples' stiffness in their hydrated state.

The indentation curves were processed with the OriginPro software. Specifically, a linear regression of the approach phase of indentation was used to extract the stiffness of the samples. The Young's modulus was quantified by fitting force-indentation curves with the following adapted Hertz model that accounts for the geometry of the indenter:

$$F = \frac{4}{3}\frac{E}{(1-\upsilon^2)}R^{0.5}d^{1.5}$$

where F represents the corresponding load, E represents the Young's modulus, υ is the Poisson's ratio of the material (set at 0.5 throughout the conditions), R is the radius of the indenter, and d is the indentation depth.

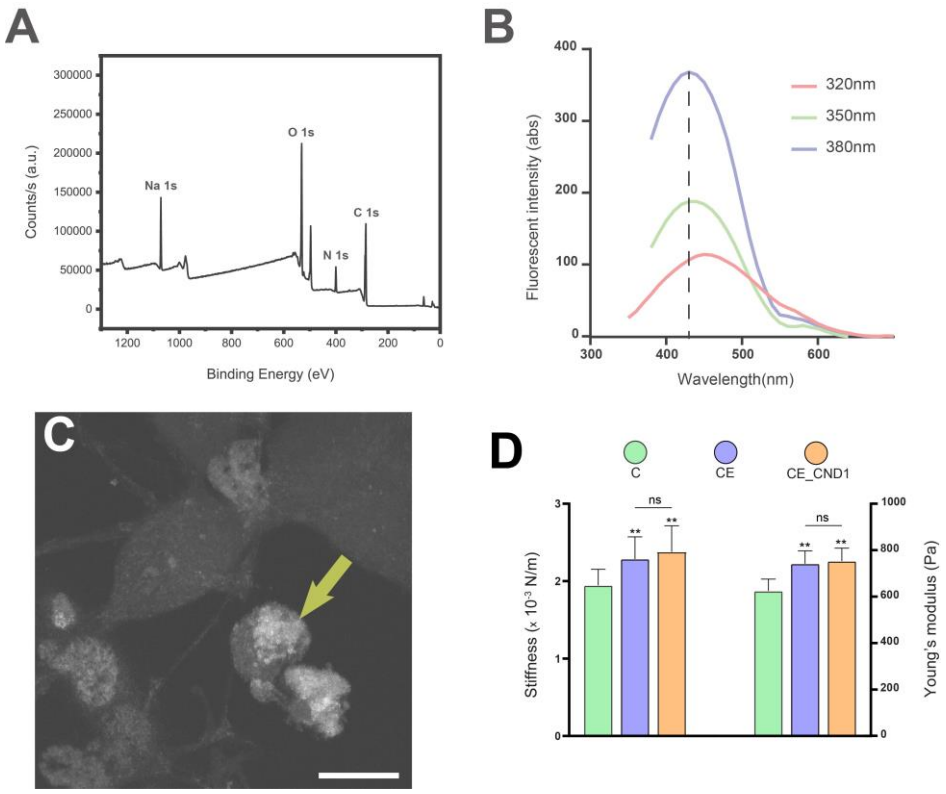

Figure S3.1: XPS survey scan, intrinsic fluorescent emission, bioaccumulation of GlyCNDs when suspended in culturing media and mechanical characterization of the nanocomposite and relevant controls via AFM nanoindentations. (A) XPS survey scan of GlyCDs revealing five binding energies ascribed to Na1s, O1s, N1s and C1s. (B) Fluorescence emission spectra at room temperature of GlyCNDs at excitation wavelengths of 320, 350 and 380 nm. (C) Representative image showing the bioaccumulation (yellow arrow) of free-suspended GlyCNDs. Scale bar: 10 µm. (D) Stiffness (*left*) and Young's Modulus (*right*) values of pristine collagen (C), EDC/NHS crosslinked collagen (CE) and nanocomposite (CE_CND1) extracted via AFM indentations.

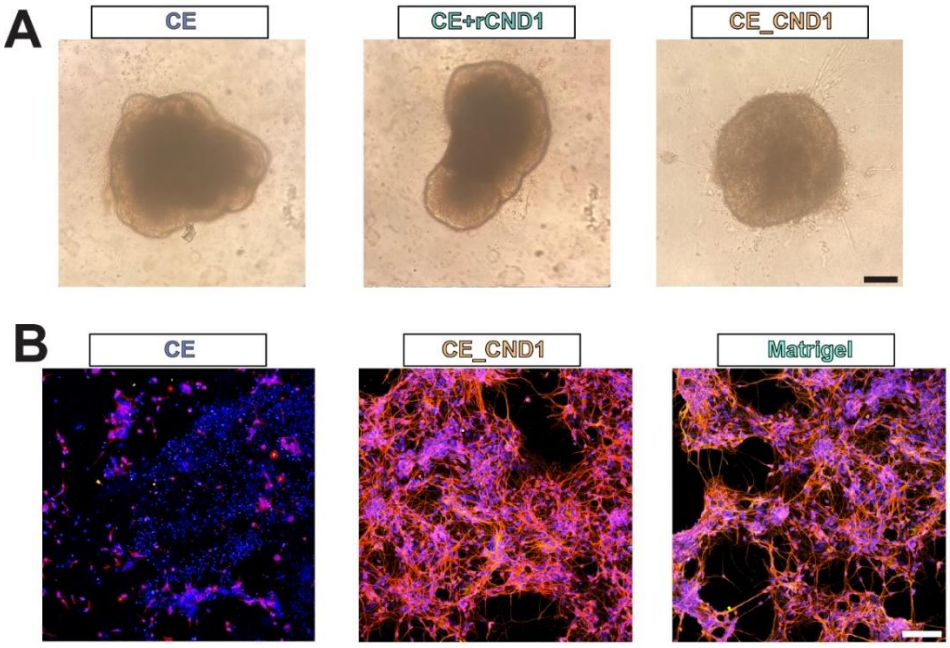

Figure S3.2: (A) Representative 5 DIV brightfield images of spheroids embedded in CE, CE+rCND1 and CE_CND1 matrices. Scale bar: 200 µm. (B) Representative immunofluorescence images showing the 10-day expression of β III-tubulin and MAP2 in mouse primary cortical neurons cultured in CE, CE_CND1 and Matrigel. Nuclei were stained with DAPI. Scale bar: 100 µm.

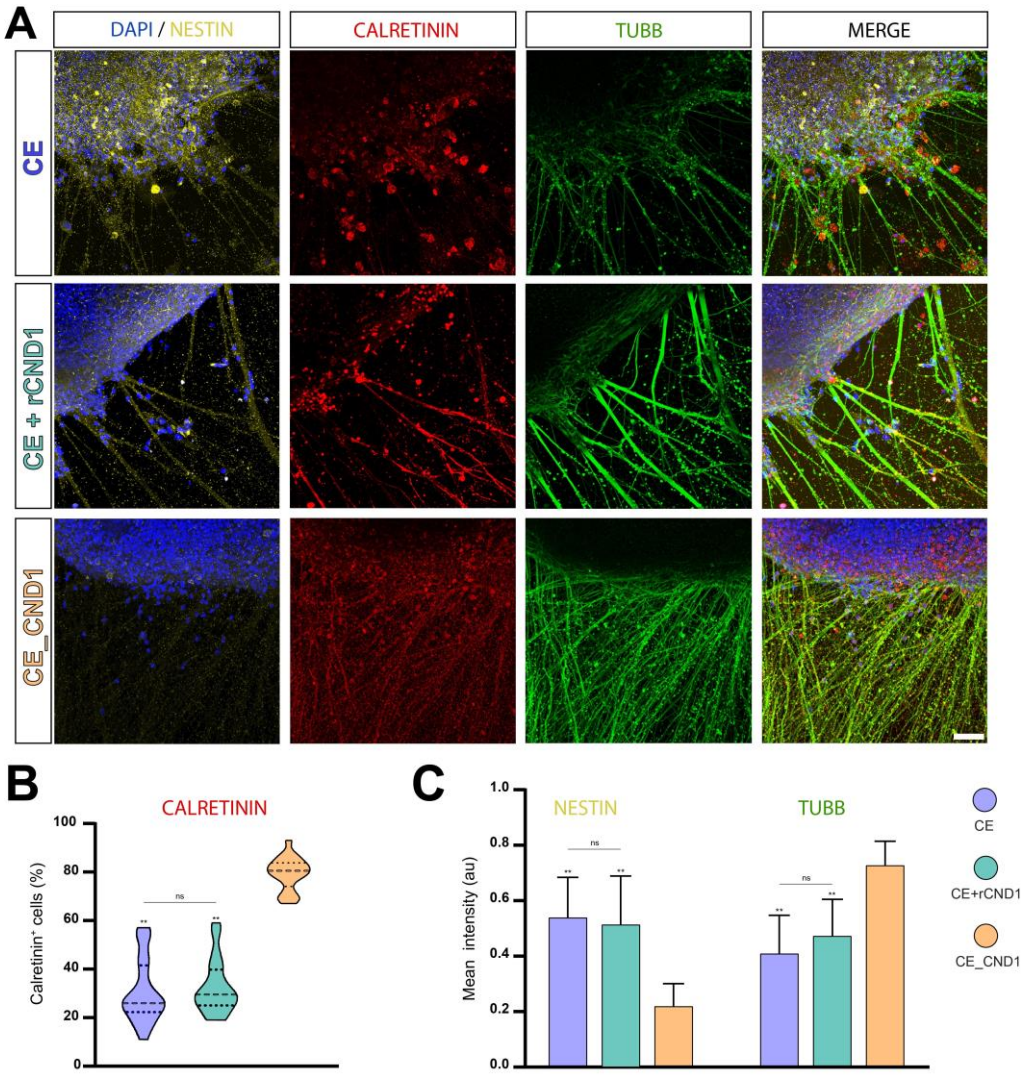

Figure S3.3: Spheroids expression of key neuronal markers at 14 DIV. (A) Representative immunofluorescence images showing the 14-day expression of nestin, calretinin and β III-tubulin in spheroids embedded in CE, CE+rCND1 and CE_CND1. Nuclei were stained with DAPI. Scale bar: 100 µm. (B) Percentage of calretinin positive NPs found across the three conditions. (C) Average intensity of nestin and β III-tubulin expressed by NP spheroids embedded in CE, CE+rCND1 and CE_CND1. All numerical data are presented as mean ± s.d. Statistical significance was determined using one-way analysis of variance (ANOVA) and Tukey's Honestly Significant Difference (HSD) post hoc test: ** $p < 0.01$, * $p < 0.05$, non-significant (ns) $p > 0.05$).

6.3 CHAPTER4: SUPPLEMENTARY INFORMATION

6.3.1 Derivation of NSCs from mouse iPSCs

Figure 4S.1A shows the step-by step process that was followed to obtain iNSCs from mouse iPSCs. Briefly, inactivated MEF were grown on 6 well plate previously coated for 2h at room temperature with 1% gelatin solution (A1). iMEF acted as a feeder layer for iPSCs. iPSCs were allowed to proliferate and create colonies (A2). iPSCs were then cultured in neurogenic induction media for 12 days (A3). Once dissociated, cells adhere on non-coated plate as single NSCs (A4).

To evaluate their successful derivation from iPSCs, NSCs were cultured on laminin coated 12 mm coverslips. After 2 DIV, the cells were stained for neural precursor marker nestin and β-III tubulin and visualized via AxioObserver.Z1 inverted epifluorescence microscope (Zeiss) through a 20X Plan-Apo (Ph2) objective (NA = 0.8, Zeiss). As shown in **Figure 4S.1B**, NSCs greatly expressed the neural precursor marker nestin. On the other hand, few cells were found positive for tubulin expression.

6.3.2 AFM nanoindentation

The samples' stiffnesses were extracted from indentation curves performed on AFM module on an Alpha300 RSA system using a spherical silicon nitride tip with a precalibrated spring constant of 0.133 N m−1 and a diameter of 5 μm (Bruker, USA, MLCT-SPH-5UM, cantilever E). Indentations were carried out in PBS 1× to quantify the samples' stiffness in their hydrated state.

The indentation curves were processed with the OriginPro software. Specifically, a linear regression of the approach phase of indentation was used to extract the stiffness of the samples.

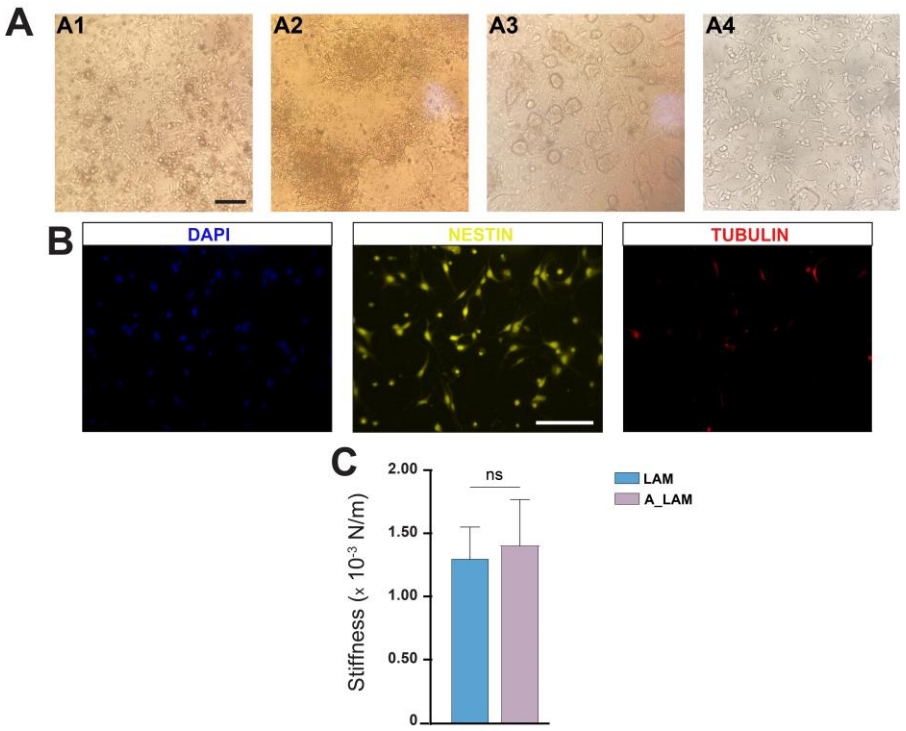

Figure S4.1: Derivation of NSCs from mouse iPSCs and mechanical characterization of aligned (A_LAM) and randomly oriented (LAM) collagen hydrogels. (A) Schematic of the steps followed for the derivation of NSCs. Scale bar: 50 µm. (B) Representative images of NSCs expression of nestin (*yellow*) and β-III tubulin (*red*) after 2DIV. Scale bar: 50 µm. (C) Stiffness values obtained for LAM and A_LAM conditions.

7. REFERENCES

1. Lee, S. J. *et al.* Advances in 3D Bioprinting for Neural Tissue Engineering. *Adv. Biosyst.* **2**, 1–18 (2018).
2. Kumar, R., Aadil, K. R., Ranjan, S. & Kumar, V. B. Advances in nanotechnology and nanomaterials based strategies for neural tissue engineering. *J. Drug Deliv. Sci. Technol.* **57**, 101617 (2020).
3. Willerth, S. M. Neural tissue engineering using embryonic and induced pluripotent stem cells. *Stem Cell Res. Ther.* 1–9 (2011).
4. Montgomery, A., Wong, A., Gabers, N. & Willerth, S. M. Engineering personalized neural tissue by combining induced pluripotent stem cells with fibrin scaffolds. *Biomater. Sci.* **3**, 401–413 (2015).
5. Armstrong, J. P. K. & Stevens, M. M. Emerging Technologies for Tissue Engineering: From Gene Editing to Personalized Medicine. *Tissue Eng. - Part A* **25**, 688–692 (2019).
6. Boni, R., Ali, A., Shavandi, A. & Clarkson, A. N. Current and novel polymeric biomaterials for neural tissue engineering. *J. Biomed. Sci.* **25**, 1–21 (2018).
7. Pina, S. *et al.* Regenerative Medicine Applications. *Materials (Basel).* **12**, 1824 (2019).
8. de Luca, A. C., Lacour, S. P., Raffoul, W. & di Summa, P. G. Extracellular matrix components in peripheral nerve repair: How to affect neural cellular response and nerve regeneration? *Neural Regen. Res.* **9**, 1943–1948 (2014).
9. Stukel, J. M. & Willits, R. K. Mechanotransduction of neural cells through cell-substrate interactions. *Tissue Eng. - Part B Rev.* **22**, 173–182 (2016).
10. Barros, C. S., Franco, S. J. & Müller, U. Extracellular Matrix: Functions in the nervous system. *Cold Spring Harb. Perspect. Biol.* **3**, 1–24 (2011).
11. Melrose, J., Hayes, A. J. & Bix, G. The CNS/PNS extracellular matrix provides instructive guidance cues to neural cells and neuroregulatory proteins in neural development and repair. *International Journal of Molecular Sciences* **22**, (2021).
12. Lau, L. W., Cua, R., Keough, M. B., Haylock-Jacobs, S. & Yong, V. W. Pathophysiology of the brain extracellular matrix: A new target for remyelination. *Nature Reviews Neuroscience*, (2013).
13. Xu, L., Nirwane, A. & Yao, Y. Basement membrane and blood-brain barrier. *Stroke and Vascular Neurology*, (2019).
14. Dityatev, A. & Schachner, M. Extracellular matrix molecules and synaptic plasticity. *Nat. Rev. Neurosci.* (2003).
15. Shetty, A. K. & Zanirati, G. The interstitial system of the brain in health and disease. *Aging and Disease*, (2020).
16. Dyck, S. M. & Karimi-Abdolrezaee, S. Chondroitin sulfate proteoglycans: Key modulators in

the developing and pathologic central nervous system. *Experimental Neurology*, (2015).

17. Fernández-Klett, F. & Priller, J. The fibrotic scar in neurological disorders. *Brain Pathol.* **24**, 404–413 (2014).
18. Tran, A. P., Warren, P. M. & Silver, J. The biology of regeneration failure and success after spinal cord injury. *Physiol. Rev.* **98**, 881–917 (2018).
19. Plantman, S. *et al.* Integrin-laminin interactions controlling neurite outgrowth from adult DRG neurons in vitro. *Mol. Cell. Neurosci.* **39**, 50–62 (2008).
20. Myers, J. P., Santiago-medina, M. & Gomez, T. M. Regulation of axonal outgrowth and pathfinding by integrin-ECM interactions. *Dev Neurobiol* **71**, 901–923 (2011).
21. McKee, K. K. *et al.* Schwann cell myelination requires integration of laminin activities. *J. Cell Sci.*, (2012).
22. Menezes, M. J. *et al.* The extracellular matrix protein laminin α2 regulates the maturation and function of the blood–brain barrier. *J. Neurosci.* (2014).
23. Zimmermann, D. R. & Dours-Zimmermann, M. T. Extracellular matrix of the central nervous system: From neglect to challenge. *Histochemistry and Cell Biology*, (2008).
24. Toole, B. P. Hyaluronan in morphogenesis. *Semin. Cell Dev. Biol.* (2001).
25. Yanagishita, M. Function of proteoglycans in the extracellular matrix. *Pathology International* (1993).
26. Maeda, N. Proteoglycans and neuronal migration in the cerebral cortex during development and disease. *Front. Neurosci.*, (2015).
27. Ozgun A., Lomboni D., Arnott H., Staines, W. A., Woulfe J., V. F. Biomaterials-based strategies for in vitro neural models. *Biomater. Sci.* **10**, 1134–1165 (2022).
28. Dias, D. O. & Göritz, C. Fibrotic scarring following lesions to the central nervous system. *Matrix Biol.* **68**–**69**, 561–570 (2018).
29. Budday, S. *et al.* Towards microstructure-informed material models for human brain tissue. *Acta Biomater.* **104**, 53–65 (2020).
30. Flanagan, L. A., Ju, Y. El, Marg, B., Osterfield, M. & Janmey, P. A. Neurite branching on deformable substrates. *Neuroreport* **13**, 2411–2415 (2002).
31. Engler, A. J. *et al.* Myotubes differentiate optimally on substrates with tissue-like stiffness: Pathological implications for soft or stiff microenvironments. *J. Cell Biol.*, (2004).
32. Morgan, E. F., Unnikrisnan, G. U. & Hussein, A. I. Bone Mechanical Properties in Healthy and Diseased States. *Annual Review of Biomedical Engineering* at https://doi.org/10.1146/annurev-bioeng-062117-121139 (2018).
33. Engler, A. J., Sen, S., Sweeney, H. L. & Discher, D. E. Matrix Elasticity Directs Stem Cell Lineage Specification. *Cell* **126**, 677–689 (2006).
34. Barnes, J. M., Przybyla, L. & Weaver, V. M. Tissue mechanics regulate brain development, homeostasis and disease. *Journal of Cell Science*, (2017).

35. Schlie-wolter, S., Ngezahayo, A. & Chichkov, B. N. The selective role of ECM components on cell adhesion , morphology , proliferation and communication in vitro. *Exp. Cell Res.* **319**, 1553–1561 (2013).
36. Lepelletier, F. X., Mann, D. M. A., Robinson, A. C., Pinteaux, E. & Boutin, H. Early changes in extracellular matrix in Alzheimer's disease. *Neuropathol. Appl. Neurobiol.* **43**, 167–182 (2017).
37. George, Naijil, H. M. G. Extracellular Matrix and Traumatic Brain Injury Naijil. *J Neurosci Res.* **96**, (2018).
38. Pitkänen, A. *et al. Neural ECM and epilepsy*. *Progress in Brain Research* vol. 214 (2014).
39. Zhang, Q. Y. *et al.* Stiff substrates enhance cultured neuronal network activity. *Sci. Rep.* **4**, 12–15 (2014).
40. Liu, J. *et al.* Control of neuronal network organization by chemical surface functionalization of multi-walled carbon nanotube arrays. *Nanotechnology* **22**, (2011).
41. Terryn, J. *et al.* Topographical Guidance of PSC-Derived Cortical Neurons. *J. Nanomater.* (2018).
42. Yu, L. M. Y., Leipzig, N. D. & Shoichet, M. S. Promoting neuron adhesion and growth. *MaterialsToday* **11**, 36–43 (2008).
43. Kim, Y. H., Baek, N. S., Han, Y. H., Chung, M. & Jung, S. Enhancement of neuronal cell adhesion by covalent binding of poly- d -lysine. *J. Neurosci. Methods* **202**, 38–44 (2011).
44. Qian, L. & Saltzman, W. M. Improving the expansion and neuronal differentiation of mesenchymal stem cells through culture surface modification. *Biomaterials* **25**, 1331–1337 (2004).
45. Lam, D. *et al.* Tissue-specific extracellular matrix accelerates the formation of neural networks and communities in a neuron-glia co-culture on a multi-electrode array. *Sci. Rep.* **9**, 1–15 (2019).
46. Soh-Zeom Yow, ze Han Lim , Evelyn K. F. Yim, C. T. L. and K. W. L. A 3D Electroactive Polypyrrole-Collagen Fibrous Scaffold for Tissue Engineering. *Polymers (Basel).* 527–544 (2011).
47. Liu, H. *et al.* Aligned graphene / silk fibroin conductive fibrous scaffolds for guiding neurite outgrowth in rat spinal cord neurons. *J. Biomed. Mater. Res. - Part A* 488–499 (2020).
48. Jakobsson, A. *et al.* Three-dimensional functional human neuronal networks in uncompressed low-density electrospun fiber scaffolds. *Nanomedicine* **13**, 1563–1573 (2017).
49. Kim, D., Kim, S., Lee, S. & Yoon, M. Investigation of neuronal pathfinding and construction of artificial neuronal networks on 3D-arranged porous fibrillar scaffolds with controlled geometry. *Sci. Rep.* 1–10 (2017).
50. Safaeijavan, R., Soleimani, M., Divsalar, A. & Eidi, A. Comparison of random and aligned PCL nanofibrous electrospun scaffolds on cardiomyocyte differentiation of human adipose-derived stem cells. *Iran. J. Basic Med. Sci.* **98**, (2014).

51. Gu, Y. *et al.* The influence of substrate stiffness on the behavior and functions of Schwann cells in culture. *Biomaterials* **33**, 6672–6681 (2012).
52. Previtera, M. L., Langhammer, C. G. & Firestein, B. L. Effects of substrate stiffness and cell density on primary hippocampal cultures. *J. Biosci. Bioeng.* **110**, 459–470 (2010).
53. Wen, Y. Q. *et al.* Substrate stiffness affects neural network activity in an extracellular matrix proteins dependent manner. *Colloids Surfaces B Biointerfaces* **170**, 729–735 (2018).
54. Silvia Buddaya, Richard Nayb, Rijk de Rooijc, Paul Steinmanna, Thomas Wyrobekb, Timothy C. Ovaertd, and E. K. Mechanical properties of gray and white matter brain tissue by indentation. *J Mech Behav Biomed Mater* **46**, (2015).
55. Alireza Karimi a, Ahmad Shojaei b, P. T. c. Mechanical properties of the human spinal cord under the compressive loading. *J. Chem. Neuroanat.* **86**, (2017).
56. De Juan Romero, C. & Borrell, V. Coevolution of radial glial cells and the cerebral cortex. *Glia* **63**, 1303–1319 (2015).
57. Diane Hoffman-Kim, Jennifer A. Mitchel, and R. V. B. Topography, Cell Response, and Nerve Regeneration. *Annu Rev Biomed Eng* **15**, 203–231 (2010).
58. Nikkhah, M., Edalat, F., Manoucheri, S. & Khademhosseini, A. Engineering microscale topographies to control the cell-substrate interface. *Biomaterials* **33**, 5230–5246 (2012).
59. Lee, C. H., Cheng, Y. W. & Huang, G. S. Topographical control of cell-cell interaction in C6 glioma by nanodot arrays. *Nanoscale Res. Lett.* **9**, 1–11 (2014).
60. Gärtner, A., Fornasiero, E. F. & Dotti, C. G. Cadherins as regulators of neuronal polarity. *Cell Adhes. Migr.* **9**, 175–182 (2015).
61. Qi, L. *et al.* The Effects of Topographical Patterns and Sizes on Neural Stem Cell Behavior. *PLoS One* **8**, 2–9 (2013).
62. Otomo, A. *et al.* Efficient differentiation and polarization of primary cultured neurons on poly(lactic acid) scaffolds with microgrooved structures. *Sci. Rep.* **10**, 1–11 (2020).
63. Pardo-Figuerez, M. *et al.* Controlled Arrangement of Neuronal Cells on Surfaces Functionalized with Micropatterned Polymer Brushes. *ACS Omega* **3**, 12383–12391 (2018).
64. Lu, D. *et al.* Microgrooved surface modulates neuron differentiation in human embryonic stem cells. *Methods Mol. Biol.* **1307**, 281–287 (2014).
65. David Y Fozdar, Jae Young Lee, Christine E Schmidt, and S. C. Hippocampal neurons respond uniquely to topographies of various sizes and shapes. *Biofabrication* **2**, (2010).
66. Chua, J. S. *et al.* Extending neurites sense the depth of the underlying topography during neuronal differentiation and contact guidance. *Biomaterials* **35**, 7750–7761 (2014).
67. Kim, J. *et al.* Nanotopographical manipulation of focal adhesion formation for enhanced differentiation of human neural stem cells. *ACS Appl. Mater. Interfaces* **5**, 10529–10540 (2013).
68. Yang, K. *et al.* Multiscale, hierarchically patterned topography for directing human neural stem cells into functional neurons. *ACS Nano* **8**, 7809–7822 (2014).

69. Amores de Sousa, M. C. *et al.* Functionalization of Electrospun Nanofibers and Fiber Alignment Enhance Neural Stem Cell Proliferation and Neuronal Differentiation. *Front. Bioeng. Biotechnol.* **8**, 1–16 (2020).
70. Vasita, R. & Katti, D. S. Nanofibers and their applications in tissue engineering. *Int. J. Nanomedicine* **1**, 15–30 (2006).
71. Shawn H. Lim, Xingyu Y. Liu, Hongjun Song, Kevin J. Yarema1, and H.-Q. M. The effect of nanofiber-guided cell alignment on the preferential differentiation of neural stem cells. *Biomaterials.* **31**, (2010).
72. Wang, Y. *et al.* The promotion of neural progenitor cells proliferation by aligned and randomly oriented collagen nanofibers through β1 integrin/MAPK signaling pathway. *Biomaterials* **32**, 6737–6744 (2011).
73. Christopher D.L. Johnson, A. R. D. and R. J. G. Electrospun fibers for drug delivery after spinal cord injury and the effects of drug incorporation on fiber properties. *Cells Tissues Organs* **202**, 116–135 (2016).
74. Smith Callahan, L. A. *et al.* Directed differentiation and neurite extension of mouse embryonic stem cell on aligned poly(lactide) nanofibers functionalized with YIGSR peptide. *Biomaterials* **34**, 9089–9095 (2013).
75. Zhang, C. *et al.* Exploration of the Effects of Substrate Stiffness on Biological Responses of Neural Cells and Their Mechanisms. *ACS Omega* **5**, 31115–31125 (2020).
76. Yiqian Zhu, Xian Li, Randall Raphael R. Janairo, George Kwong, S. L. Matrix Stiffness Modulates the Differentiation of Neural Crest Stem Cells In Vivo. *J Cell Physiol.* (2019).
77. Naqvi, S. M. & McNamara, L. M. Stem Cell Mechanobiology and the Role of Biomaterials in Governing Mechanotransduction and Matrix Production for Tissue Regeneration. *Front. Bioeng. Biotechnol.* **8**, 1–27 (2020).
78. D'Angelo, M. *et al.* The role of stiffness in cell reprogramming: A potential role for biomaterials in inducing tissue regeneration. *Cells* **8**, (2019).
79. Jansen, K. A., Atherton, P. & Ballestrem, C. Mechanotransduction at the cell-matrix interface. *Semin. Cell Dev. Biol.* **71**, 75–83 (2017).
80. Kennedy, K. M., Bhaw-Luximon, A. & Jhurry, D. Cell-matrix mechanical interaction in electrospun polymeric scaffolds for tissue engineering: Implications for scaffold design and performance. *Acta Biomater.* **50**, 41–55 (2017).
81. Georges, P. C., Miller, W. J., Meaney, D. F., Sawyer, E. S. & Janmey, P. A. Matrices with compliance comparable to that of brain tissue select neuronal over glial growth in mixed cortical cultures. *Biophys. J.* **90**, 3012–3018 (2006).
82. Arulmoli, J. *et al.* Static stretch affects neural stem cell differentiation in an extracellular matrix-dependent manner. *Sci. Rep.* **5**, 1–8 (2015).
83. Chen, W. H., Cheng, S. J., Tzen, J. T. C., Cheng, C. M. & Lin, Y. W. Probing relevant molecules

in modulating the neurite outgrowth of hippocampal neurons on substrates of different stiffness. *PLoS One* **8**, (2013).

84. Teixeira, A. I. *et al.* The promotion of neuronal maturation on soft substrates. *Biomaterials* **30**, 4567–4572 (2009).
85. Di Palma, F. *et al.* Modulation of the responses of human osteoblast-like cells to physiologic mechanical strains by biomaterial surfaces. *Biomaterials* **26**, 4249–4257 (2005).
86. Yourek, G., McCormick, S. M., Mao, J. J. & Reilly, G. C. Shear stress induces osteogenic differentiation of human mesenchymal stem cells. *Regen. Med.* **5**, 713–724 (2010).
87. Blomme, B. *et al.* Mechanical strain induces a pro-fibrotic phenotype in human mitral valvular interstitial cells through RhoC/ROCK/MRTF-A and Erk1/2 signaling pathways. *J. Mol. Cell. Cardiol.* **135**, 149–159 (2019).
88. Fan, Y. *et al.* Substrate Stiffness Modulates the Growth, Phenotype, and Chemoresistance of Ovarian Cancer Cells. *Front. Cell Dev. Biol.* **9**, 1–13 (2021).
89. Park, J. S. *et al.* The Effect of Matrix Stiffness on the Differentiation of Mesenchymal Stem Cells in Response to TGF-β. *Biomaterials* **32**, 3921–3930 (2011).
90. Du, J. *et al.* Extracellular matrix stiffness dictates Wnt expression through integrin pathway. *Sci. Rep.* **6**, 1–12 (2016).
91. Petroll, W. M., Vishwanath, M. & Ma, L. Corneal fibroblasts respond rapidly to changes in local mechanical stress. *Investig. Ophthalmol. Vis. Sci.* **45**, 3466–3474 (2004).
92. Cameron, A. R., Frith, J. E. & Cooper-White, J. J. The influence of substrate creep on mesenchymal stem cell behavior and phenotype. *Biomaterials* **32**, 5979–5993 (2011).
93. Rowena McBeath, 1 Dana M. Pirone, 2 Celeste M. Nelson, 2, Kiran Bhadriraju, 2 & Chen, and C. S. Cell Shape, Cytoskeletal Tension, and RhoA Regulate Stem Cell Lineage Commitment. *Dev. Cell* **6**, (2004).
94. Albert J. Keung, Elena M. de Juan-Pardo, D. V. S. and S. K. Rho GTPases Mediate the Mechanosensitive Lineage Commitment of Neural Stem Cells. *Stem Cell* **29**, 1886–1897 (2011).
95. Dupont, S. *et al.* Role of YAP/TAZ in mechanotransduction. *Nature* **474**, 179–184 (2011).
96. Cai, X., Wang, K. C. & Meng, Z. Mechanoregulation of YAP and TAZ in Cellular Homeostasis and Disease Progression. *Front. Cell Dev. Biol.* **9**, 1–12 (2021).
97. Aragona, M. *et al.* A mechanical checkpoint controls multicellular growth through YAP/TAZ regulation by actin-processing factors. *Cell* **154**, 1047–1059 (2013).
98. Driscoll, T. P., Cosgrove, B. D., Heo, S. J., Shurden, Z. E. & Mauck, R. L. Cytoskeletal to Nuclear Strain Transfer Regulates YAP Signaling in Mesenchymal Stem Cells. *Biophys. J.* **108**, 2783–2793 (2015).
99. Zhang, Y. *et al.* Tunable Hybrid Matrices Drive Epithelial Morphogenesis and YAP Translocation. *Adv. Sci.* **8**, 1–16 (2021).
100. Sero, J. E. & Bakal, C. Multiparametric Analysis of Cell Shape Demonstrates that β-PIX

Directly Couples YAP Activation to Extracellular Matrix Adhesion. *Cell Syst.* **4**, 84-96.e6 (2017).

101. Sun, Y. *et al.* Hippo/YAP-mediated rigidity-dependent motor neuron differentiation of human pluripotent stem cells. *Nat. Mater.* **13**, 599–604 (2014).
102. Liu, B. F., Ma, J., Xu, Q. Y. & Cui, F. Z. Regulation of charged groups and laminin patterns for selective neuronal adhesion. *Colloids Surfaces B Biointerfaces* **53**, 175–178 (2006).
103. Guillon, E. *et al.* Fibronectin is a smart adhesive that both influences and responds to the mechanics of early spinal column development. *Elife* **9**, 1–34 (2020).
104. Rao, S. S. & Winter, J. O. Adhesion molecule-modified biomaterials for neural tissue engineering. *Front. Neuroeng.* **2**, 1–14 (2009).
105. Li, G. *et al.* Laminin-coated electrospun regenerated silk fibroin mats promote neural progenitor cell proliferation, differentiation, and survival in vitro. *Front. Bioeng. Biotechnol.* **7**, (2019).
106. Kamiguchi, H., Hlavin, M. L. & Lemmon, V. Role of L1 in neural development: What the knockouts tell us. *Mol. Cell. Neurosci.* **12**, 48–55 (1998).
107. Woerly, S., Pinet, E., De Robertis, L., Van Diep, D. & Bousmina, M. Spinal cord repair with PHPMA hydrogel containing RGD peptides (NeuroGel™). *Biomaterials* **22**, 1095–1111 (2001).
108. Jia Jiaa, Robert C. Coylea, Dylan J. Richardsa, Christopher Lloyd Berrya, R. W., Barrsb, Joshua Biggsa, C. J. C. & , Thomas C. Truskd, and Ying Meia, D. Development of peptide-functionalized synthetic hydrogel microarrays for stem cell and tissue engineering applications. *Acta Biomater.* 110–120 (2016).
109. Nicolas, J. *et al.* 3D Extracellular Matrix Mimics: Fundamental Concepts and Role of Materials Chemistry to Influence Stem Cell Fate. *Biomacromolecules* **21**, 1968–1994 (2020).
110. Shantanu Sura, E. T. P., Guler, M. O., , Masao Ito, S. I. & Stupp, and T. L. A hybrid nanofiber matrix to control the survival and maturation of brain neurons. *Biomaterials* **33**, 545–555 (2012).
111. Albert J. Keung1, Sanjay Kumar2, and D. V. S. Presentation Counts: Microenvironmental Regulation of Stem Cells by Biophysical and Material Cues. *Annu Rev Cell Dev Biol.* **176**, (2010).
112. Cao, H., Duan, L., Zhang, Y., Cao, J. & Zhang, K. Current hydrogel advances in physicochemical and biological response-driven biomedical application diversity. *Signal Transduct. Target. Ther.* **6**, 1–31 (2021).
113. Caddeo, S., Boffito, M. & Sartori, S. Tissue engineering approaches in the design of healthy and pathological in vitro tissue models. *Front. Bioeng. Biotechnol.* **5**, 1–22 (2017).
114. Jensen, C. & Teng, Y. Is It Time to Start Transitioning From 2D to 3D Cell Culture? *Front. Mol. Biosci.* **7**, 1–15 (2020).
115. Justice, B. A., Badr, N. A. & Felder, R. A. 3D cell culture opens new dimensions in cell-based assays. *Drug Discov. Today* **14**, 102–107 (2009).
116. Kapałczyńska, M. *et al.* 2D and 3D cell cultures – a comparison of different types of cancer cell

cultures. *Arch. Med. Sci.* **14**, 910–919 (2018).

117. Knight, E. & Przyborski, S. Advances in 3D cell culture technologies enabling tissue-like structures to be created in vitro. *J. Anat.* **227**, 746–756 (2015).
118. Fitzgerald, K. A., Malhotra, M., Curtin, C. M., O'Brien, F. J. & O'Driscoll, C. M. Life in 3D is never flat: 3D models to optimise drug delivery. *J. Control. Release* **215**, 39–54 (2015).
119. Fontoura, J. C. *et al.* Comparison of 2D and 3D cell culture models for cell growth, gene expression and drug resistance. *Mater. Sci. Eng. C* **107**, 110264 (2020).
120. Duval, K. *et al.* Modeling physiological events in 2D vs. 3D cell culture. *Physiology* **32**, 266–277 (2017).
121. El-Sherbiny, I. M. & Yacoub, M. H. Hydrogel scaffolds for tissue engineering: Progress and challenges. *Glob. Cardiol. Sci. Pract.* **2013**, 38 (2013).
122. Anseth, M. W. T. and K. S. Hydrogels as Extracellular Matrix Mimics for 3D Cell Culture. *Biotechnol Bioeng* **103**, 655–663 (2009).
123. Výborný, K. *et al.* Genipin and EDC crosslinking of extracellular matrix hydrogel derived from human umbilical cord for neural tissue repair. *Sci. Rep.* **9**, 1–15 (2019).
124. Valmikinathan, C. M. *et al.* Photocrosslinkable chitosan based hydrogels for neural tissue engineering. *Soft Matter* **8**, 1964–1976 (2012).
125. Song, W., Ko, J., Choi, Y. H. & Hwang, N. S. Recent advancements in enzyme-mediated crosslinkable hydrogels: In vivo-mimicking strategies. *APL Bioeng.* **5**, 1–22 (2021).
126. Rebers, L. *et al.* Differentiation of physical and chemical cross-linking in gelatin methacryloyl hydrogels. *Sci. Rep.* **11**, 1–12 (2021).
127. Maitra, J. & Shukla, V. K. Cross-linking in Hydrogels - A Review. *Am. J. Polym. Sci.* **4**, 25–31 (2014).
128. Nisbet, D. R., Crompton, K. E., Horne, M. K., Finkelstein, D. I. & Forsythe, J. S. Neural tissue engineering of the CNS using hydrogels. *J. Biomed. Mater. Res. - Part B Appl. Biomater.* **87**, 251–263 (2008).
129. Chen, G. *et al.* Integrated dynamic wet spinning of core-sheath hydrogel fibers for optical-to-brain/tissue communications. *Natl. Sci. Rev.* **8**, (2021).
130. Madduma-Bandarage, U. S. K. & Madihally, S. V. Synthetic hydrogels: Synthesis, novel trends, and applications. *J. Appl. Polym. Sci.* **138**, 1–23 (2021).
131. Zhao, Y. *et al.* Using NGF heparin-poloxamer thermosensitive hydrogels to enhance the nerve regeneration for spinal cord injury. *Acta Biomater.* **29**, 71–80 (2016).
132. Ma, X. *et al. Design and Fabrication of Polymeric Hydrogel Carrier for Nerve Repair*. *Polymers* vol. 14 (2022).
133. Lampe, K. J., Kern, D. S., Mahoney, M. J. & Bjugstad, K. B. The administration of BDNF and GDNF to the brain via PLGA microparticles patterned within a degradable PEG-based hydrogel: Protein distribution and the glial response. *J. Biomed. Mater. Res. - Part A* **96**, 595–607 (2011).

134. Madhusudanan, P., Raju, G. & Shankarappa, S. Hydrogel systems and their role in neural tissue engineering. *J. R. Soc. Interface* **17**, (2020).
135. Parenteau-Bareil, R., Gauvin, R. & Berthod, F. Collagen-based biomaterials for tissue engineering applications. *Materials (Basel).* **3**, 1863–1887 (2010).
136. Doblado, L. R., Martínez-Ramos, C. & Pradas, M. M. Biomaterials for Neural Tissue Engineering. *Front. Nanotechnol.* **3**, (2021).
137. Dong, C. & Lv, Y. Application of collagen scaffold in tissue engineering: Recent advances and new perspectives. *Polymers (Basel).* **8**, 1–20 (2016).
138. Chaubaroux, C. *et al.* Cell Alignment Driven by Mechanically Induced Collagen Fiber Alignment in Collagen/Alginate Coatings. *Tissue Eng. - Part C Methods* **21**, 881–888 (2015).
139. Wright, A. L., Righelli, L., Broomhall, T. J., Lamont, H. C. & El Haj, A. J. Magnetic Nanoparticle-Mediated Orientation of Collagen Hydrogels for Engineering of Tendon-Mimetic Constructs. *Front. Bioeng. Biotechnol.* **10**, 1–14 (2022).
140. Nong, L. M. *et al.* The effect of different cross-linking conditions of EDC/NHS on type II collagen scaffolds: an in vitro evaluation. *Cell Tissue Bank.* **20**, 557–568 (2019).
141. Silvan Klein , Jody Vykoukal, Oliver Felthaus, T. D. and L. P. Collagen Type I Conduits for the Regeneration of Nerve Defects. *Materials (Basel).* **9**, (2016).
142. Kim, S. H. *et al.* Anisotropically organized three-dimensional culture platform for reconstruction of a hippocampal neural network. *Nat. Commun.* **8**, (2017).
143. Iwashita, M., Ohta, H., Fujisawa, T., Cho, M. & Ikeya, M. Brain-stiffness-mimicking tilapia collagen gel promotes the induction of dorsal cortical neurons from human pluripotent stem cells. *Sci. Rep.* 1–17 (2019).
144. Labour, M., Vigier, S., Lerner, D., Marcilhac, A. & Belamie, E. 3D compartmented model to study the neurite-related toxicity of A b aggregates included in collagen gels of adaptable porosity. *Acta Biomater.* (2016).
145. Rouleau, N. *et al.* A Long-Living Bioengineered Neural Tissue Platform to Study Neurodegeneration. *Macromol Biosci* **20**, (2020).
146. Fathi-Achachelouei, M. *et al.* Use of Nanoparticles in Tissue Engineering and Regenerative Medicine. *Front. Bioeng. Biotechnol.* **7**, 1–22 (2019).
147. Hasan, A. *et al.* Nanoparticles in tissue engineering: Applications, challenges and prospects. *Int. J. Nanomedicine* **13**, 5637–5655 (2018).
148. Khan, F. A., Almohazey, D., Alomari, M. & Almofty, S. A. Impact of nanoparticles on neuron biology: Current research trends. *Int. J. Nanomedicine* **13**, 2767–2776 (2018).
149. Scarpa, E. *et al.* Tuning cell behavior with nanoparticle shape. *PLoS One* **15**, 1–16 (2020).
150. Lei, Y. *et al.* Gold nanoclusters-assisted delivery of NGF siRNA for effective treatment of pancreatic cancer. *Nat. Commun.* **8**, (2017).
151. Dowding, J. M. *et al.* Cerium oxide nanoparticles protect against Aβ-induced mitochondrial

fragmentation and neuronal cell death. *Cell Death Differ.* **21**, 1622–1632 (2014).

152. Kumar, R., Aadil, K. R., Ranjan, S. & Kumar, V. B. Advances in nanotechnology and nanomaterials based strategies for neural tissue engineering. *J. Drug Deliv. Sci. Technol.* **57**, 101617 (2020).
153. Yang, Z. *et al.* A review of nanoparticle functionality and toxicity on the central nervous system. *Nanotechnology, Brain, Futur.* 313–332 (2013).
154. Laleh Ghasemi-Mobarakeh1, Molamma P Prabhakaran2∗, MohammadMorshed3, Mohammad Hossein Nasr-Esfahani4, Hossein Baharvand5, Sahar Kiani5, S. S. A.-D. and S. R. Application of conductive polymers, scaffolds and electrical stimulation for nerve tissue engineering. *J Tissue Eng Regen Med 2011;5* (2011).
155. Burnstine-Townley, A., Eshel, Y. & Amdursky, N. Conductive Scaffolds for Cardiac and Neuronal Tissue Engineering: Governing Factors and Mechanisms. *Adv. Funct. Mater.* **30**, 1–27 (2020).
156. Baranes, K., Shevach, M., Shefi, O. & Dvir, T. Gold Nanoparticle-Decorated Scaffolds Promote Neuronal Differentiation and Maturation. *Nano Lett.* **16**, 2916–2920 (2016).
157. Tuccitto, N. *et al.* Carbon Quantum Dots as Fluorescence Nanochemosensors for Selective Detection of Amino Acids. *ACS Appl. Nano Mater.* **4**, 6250–6256 (2021).
158. Alzahrani, H. A. H. *et al.* Gold nanoparticles immobilised in a superabsorbent hydrogel matrix: Facile synthesis and application for the catalytic reduction of toxic compounds. *Chem. Commun.* **56**, 1263–1266 (2020).
159. I. Ghiuță, D. C. Silver nanoparticles for delivery purposes. *Nanoeng. Biomater. Adv. Drug Deliv.* 347–371 (2020).
160. Söderstjerna, E., Johansson, F., Klefbohm, B. & Englund Johansson, U. Gold- and Silver Nanoparticles Affect the Growth Characteristics of Human Embryonic Neural Precursor Cells. *PLoS One* **8**, 1–13 (2013).
161. Kogan, M. J. *et al.* Peptides and metallic nanoparticles for biomedical applications. *Nanomedicine* **2**, 287–306 (2007).
162. Zare Marzouni, H. *et al.* Cytotoxic Effects of Coated Gold Nanoparticles on PC12 Cancer Cell. *Galen Med. J.* **7**, e1110 (2018).
163. Xiong, P. *et al.* Cytotoxicity of Metal-Based Nanoparticles: From Mechanisms and Methods of Evaluation to Pathological Manifestations. *Adv. Sci.* **9**, 1–22 (2022).
164. Azam, N., Najabat Ali, M. & Javaid Khan, T. Carbon Quantum Dots for Biomedical Applications: Review and Analysis. *Front. Mater.* **8**, 1–21 (2021).
165. Shen, C. *et al.* Theranostics Recent progress of carbon dots in targeted bioimaging and cancer therapy. *Theranostics* **12**, 29–32 (2022).
166. Li, M. & Zhang, S. X. A. Carbon dots with continuously tunable full-color emission and their application in ratiometric pH sensing". *Chem. Mater.* **26**, 6084 (2014).

167. Wen, X., Nadirah, A., Romainor, B., Fun, S. & Muk, S. Journal of Analytical and Applied Pyrolysis Carbon dots production via pyrolysis of sago waste as potential probe for metal ions sensing. *J. Anal. Appl. Pyrolysis* **105**, 157–165 (2014).
168. Ye, L. *et al.* Carbon Nanotube–Hydrogel Composites Facilitate Neuronal Differentiation While Maintaining Homeostasis of Network Activity. *Adv. Mater.* **33**, (2021).
169. Noh, E. *et al.* Carbon nanodot-based self-delivering microRNA sensor to visualize microRNA124a expression during neurogenesis. *J. Mater. Chem. B* 4438–4445 (2013) doi:10.1039/c3tb20710b.
170. Xu Han, Zhifeng Jing, Wei Wu, Bing Zou, Zhili Peng, Pengyu Ren, A. & Wikramanayake, Zhongmin Lu, and R. M. L. Biocompatible and Blood-Brain Barrier Permeable Carbon Dots for Inhibition of Aβ Fibrillation and Toxicity, and BACE1 Activity. *Nanoscale* **9**, 12862–12866 (2017).
171. Onoda, A., Umezawa, M., Takeda, K., Ihara, T. & Sugamata, M. Effects of maternal exposure to ultrafine carbon black on brain perivascular macrophages and surrounding astrocytes in offspring mice. *PLoS One* **9**, (2014).
172. Lee, H. *et al.* Effect of carbon nanomaterial dimension on the functional activity and degeneration of neurons. *Biomaterials* **279**, 121232 (2021).
173. Kumar, V. B., Kumar, R., Gedanken, A. & Shefi, O. Fluorescent Metal-Doped Carbon Dots for Neuronal. *Ultrason. - Sonochemistry* (2018) doi:10.1016/j.ultsonch.2018.11.017.
174. Beaudoin, G. M. J. *et al.* Culturing pyramidal neurons from the early postnatal mouse hippocampus and cortex. *Nat. Protoc.* **7**, 1741–1754 (2012).
175. Zhang, J. *et al.* Recent progresses in novel in vitro models of primary neurons: A biomaterial perspective. *Front. Bioeng. Biotechnol.* **10**, 1–22 (2022).
176. Jennifer Gordon, Shohreh Amini, and M. K. W. General overview of neuronal cell culture. *Methods Mol Biol.* **1078**, 35–44 (2013).
177. Yin, K., Baillie, G. J. & Vetter, I. Neuronal cell lines as model dorsal root ganglion neurons: A transcriptomic comparison. *Mol. Pain* (2016).
178. Xicoy, H., Wieringa, B. & Martens, G. J. M. The SH-SY5Y cell line in Parkinson's disease research: a systematic review. *Molecular Neurodegeneration* (2017).
179. Slanzi, A., Iannoto, G., Rossi, B., Zenaro, E. & Constantin, G. In vitro Models of Neurodegenerative Diseases. *Front. Cell Dev. Biol.* **8**, (2020).
180. Frattini, A. *et al.* High variability of genomic instability and gene expression profiling in different HeLa clones. *Sci. Rep.* (2015).
181. Li, J., Settivari, R. S. & LeBaron, M. J. Genetic instability of in vitro cell lines: Implications for genetic toxicity testing. *Environ. Mol. Mutagen.* **60**, 559–562 (2019).
182. Edwards, M. A., Loxley, R. A., Williams, A. J., Connor, M. & Phillips, J. K. Lack of functional expression of NMDA receptors in PC12 cells. *Neurotoxicology* **28**, 876–885 (2007).

183. Jane Kovalevich and Dianne Langford. Considerations for the Use of SH-SY5Y Neuroblastoma Cells in Neurobiology. *Methods Mol Biol.* **1078**, (2013).
184. Ahmadi, N., Razavi, S., Kazemi, M. & Oryan, S. Tissue and Cell Stability of neural differentiation in human adipose derived stem cells by two induction protocols. *Tissue Cell* **44**, 87–94 (2012).
185. Maxim A. Vodyanik, Junying Yu, Xin Zhang, Shulan Tian, Ron Stewart, J. A. & Thomson, and I. I. S. A mesoderm-derived precursor for mesenchymal stem and endothelial cells. *Cell Stem Cell.* **7**, 718–729 (2010).
186. Hernández, R. *et al.* Differentiation of human mesenchymal stem cells towards neuronal lineage: Clinical trials in nervous system disorders. *Biomol. Ther.* **28**, 34–44 (2020).
187. Zha, K. *et al.* Nerve growth factor (NGF) and NGF receptors in mesenchymal stem/stromal cells: Impact on potential therapies. *Stem Cells Transl. Med.* **10**, 1008–1020 (2021).
188. Nihal Karakaş, Sadık Bay,Nezaket Tu¨rke, G. O. ztu¨rk. Neurons from human mesenchymal stem cells display both spontaneous and stimuli responsive activity. *PLoS One* 1–18 (2020).
189. Costa, H. J. Z. R. *et al.* Mesenchymal bone marrow stem cells within polyglycolic acid tube observed in vivo after six weeks enhance facial nerve regeneration. *Brain Res.* **1510**, 10–21 (2013).
190. Andrzejewska, A., Dabrowska, S., Lukomska, B. & Janowski, M. Mesenchymal Stem Cells for Neurological Disorders. *Adv. Sci.* **8**, 1–27 (2021).
191. Cui, L. Z. • H.-F. Use of chitosan conduit combined with bone marrow mesenchymal stem cells for promoting peripheral nerve regeneration. *J Mater Sci Mater Med* 1713–1720 (2010).
192. Chopp, M., Li, Y. & Zhang, Z. G. Mechanisms underlying improved recovery of neurological function after stroke in the rodent after treatment with neurorestorative cell-based therapies. *Stroke* **40**, 10–13 (2009).
193. Li Hong Shena, Qi Gaoa, Yi Lia, Smita Savant-Bhonsaleb, and M. C. Down-regulation of neurocan expression in reactive astrocytes promotes axonal regeneration and facilitates the neurorestorative effects of bone marrow stromal cells in the ischemic rat brain. *Glia.* (2008).
194. Asim Mahmood, 1 Changsheng Qu, 1 Riuzuo Ning, 1 Hongtao Wu, 1 Anton Goussev, 1 Ye Xiong, 1 & Susan Irtenkauf, 1 Yi Li, 2 and Michael Chopp2, 3. Treatment of TBI with Collagen Scaffolds and Human Marrow Stromal Cells Increases the Expression. *J. Neurotrauma* 1199–1207 (2011).
195. Zanier, E. R. *et al.* Bone Marrow Mesenchymal Stromal Cells Drive Protective M2 Microglia Polarization After Brain Trauma. *Neurotherapeutics* 679–695 (2014).
196. Volarevic, V. *et al.* Ethical and safety issues of stem cell-based therapy. *Int. J. Med. Sci.* **15**, 36–45 (2018).
197. Omole, A. E. & Fakoya, A. O. J. Ten years of progress and promise of induced pluripotent stem cells: Historical origins, characteristics, mechanisms, limitations, and potential applications.

PeerJ **2018**, 1–47 (2018).

198. Steven A. Sloan1, Jimena Andersen1, Anca M. Pașca2,*, Fikri Birey1, and S. P. P. Generation and Assembly of Human Brain Region-Specific Three-Dimensional Cultures. *Nat Protoc.* **13**, (2018).
199. Martin L. Tomov, Alison O'Neil, Hamdah S. Abbasi, Beth A. Cimini, Anne E. Carpenter, Lee L. Rubin & Mark Bathe Martin L. Tomov, Alison O'Neil, Hamdah S. Abbasi, Beth A. Cimini, Anne E. Carpenter, L. L. R. & M. B. Resolving cell state in iPSC-derived human neural samples with multiplexed fluorescence imaging. *Commun. Biol.* **4**, (2021).
200. Valadez-Barba, V. *et al.* iPSC for modeling neurodegenerative disorders. *Regen. Ther.* **15**, 332–339 (2020).
201. Logan, S. *et al.* Studying Human Neurological Disorders Using Induced Pluripotent Stem Cells: From 2D Monolayer to 3D Organoid and Blood Brain Barrier Models. *Compr. Physiol.* **9**, 565–611 (2019).
202. Renner, M. *et al.* Self-organized developmental patterning and differentiation in cerebral organoids. *EMBO J.* **36**, 1316–1329 (2017).
203. L. Papadimitriou, P. Manganas, A. R. and E. S. Biofabrication for neural tissue engineering applications. *Mater. Today Bio* (2020).
204. J. K. Yoon, M. L. Kang, J. H. Park, K. M. Lee, Y. M. S. and & Lee, J. W. Direct control of stem cell behavior using biomaterials and genetic factors. *Stem Cells Int.* (2018).
205. H. Amani, H. Arzaghi, M. Bayandori, A. S. D. & Shafiee, H. P.-T. and A. Controlling cell behavior through the design of biomaterial surfaces: A focus on surface modification techniques,. *Adv. Mater. Interfaces* **6**, (2019).
206. M. Shahrousvand, G. M. M. Sadeghi, E. S. & SalimI, M. G. and A. Superficial physicochemical properties of polyurethane biomaterials as osteogenic regulators in human mesenchymal stem cells fates,. *Colloids Surf., B* **156**, (2017).
207. S. R. Moxon, N. J. Corbett, K. Fisher, G. P. & Hooper, M. D. and N. M. Blended alginate/collagen hydrogels promote neurogenesis and neuronal maturation. *Mater. Sci. Eng* **104**, (2019).
208. B. G. Munoz-Robles, I. K. and C. A. D. Surface patterning of hydrogel biomaterials to probe and direct cell–matrix interactions. *Adv. Mater. Interfaces* **7**, (2020).
209. M. Pardo-Figuerez, N. R. W. Martin, D. J. Player, P. R. & Capel, S. D. R. C. and A. J. Controlled arrangement of neuronal cells on surfaces functionalized with micropatterned polymer brushes. *ACS Omega* **3**, (2018).
210. E. G. Long, M. Buluk, M. B. Gallagher, J. M. S. and & Brown, J. L. Human mesenchymal stem cell morphology, migration, and differentiation on micro and nano-textured titanium. *Bioact. Mater.* **4**, (2019).
211. G. S. Lorite, L. Yla ¨-Outinen, L. Janssen, O. Pitka ¨nen, T. J. & Koivisto, and J. T. Carbon

nanotube micropillars trigger guided growth of complex human neural stem cells networks,. *Nano Res* **12**, (2019).

212. A. Tijore, S. A. Irvine, U. Sarig, P. Mhaisalkar, V. B. & Venkatraman, and S. Contact guidance for cardiac tissue engineering using 3D bioprinted gelatin patterned hydrogel. *Biofabrication* **10**, (2018).
213. M. Mattotti, L. Micholt, D. B. and D. K. ˇic ´. Characterization of spiral ganglion neurons cultured on silicon micro-pillar substrates for new auditory neuro-electronic interfaces,. *J. Neural Eng* **12**, (2015).
214. H. Lv, L. Li, M. Sun, Y. Zhang, L. C. and Y. R. Mechanism of regulation of stem cell differentiation by matrix stiffness. *Stem Cell Res. Ther* **6**, (201AD).
215. Engler, J. R. T. and A. J. Stiffness gradients mimicking in vivo tissue variation regulate mesenchymal stem cell fate. *PLoS One* **6**, (2011).
216. T. Neuroscience, Atomic force microscopy as an advanced tool in neuroscience. *Transl. Neurosci* (2015).
217. A. M. Ross, Z. Jiang, M. B. and J. L. Physical aspects of cell culture substrates: Topography, roughness, and elasticity. *Small* **3**, (2012).
218. R. C. F. Cheung, T. B. Ng, J. H. W. and W. Y. C. Chitosan: An update on potential biomedical and pharmaceutical applications. *Mar. Drugs* **13**, (2015).
219. ´roˆme, F. C. and C. J. Chitosan-based biomaterials for tissue engineering. *Eur. Polym. J* **49**, (2013).
220. M. Mattotti, Z. Alvarez, L. Delgado, M. A. MateosTimoneda, C. A. and J. A. P. Differential neuronal and glial behavior on flat and micro patterned chitosan films. *Colloids Surf., B* **158**, (2017).
221. C. Y. Sung, C. Y. Yang, W. S. Chen, Y. K. Wang, J. A. Y. & Cheng, and C. M. Probing neural cell behaviors through micro-/nano-patterned chitosan substrates. *Biofabrication* **7**, (2015).
222. W. Daly, L. Yao, D. Zeugolis, A. W. and A. P. A biomaterials approach to peripheral nerve regeneration: Bridging the peripheral nerve gap and enhancing functional recovery. *J. R. Soc., Interface* (2012).
223. M. Zhu, W. Li, X. Dong, X. Yuan, A. C. M. and H. C. n vivo engineered extracellular matrix scaffolds with instructive niches for oriented tissue regeneration. *Nat. Commun* **10**, (2019).
224. A. Subramanian, U. M. K. and S. S. Development of biomaterial scaffold for nerve tissue engineering: Biomaterial mediated neural regeneration. *J. Biomed. Sci* **16**, (2009).
225. S. Yao, X. Liu, X. Wang, A. M. and X. C. Progress in natural science: Materials international directing neural stem cell fate with biomaterial parameters for injured brain regeneration. *Prog. Nat. Sci. Mater. Int.* **23**, (2013).
226. Y. Yang, Y. Zhang, R. C. and Z. G. Designs of biomaterials and microenvironments for neuroengineering. *Neural Plast.* (2018).

227. M. Sarker, S. Naghieh, A. D. McInnes, D. J. S. and & Chen, X. Strategic design and fabrication of nerve guidance conduits for peripheral nerve regeneration. *Biotechnol. J.* **13**, (2018).
228. S. Ali, I. B. Wall, C. Mason, A. E. P. and F. S. V. The effect of Young' s modulus on the neuronal differentiation of mouse embryonic stem cells. *Acta Biomater* **25**, (2015).
229. M. Rahmati, E. A. Silva, J. E. Reseland, C. A. H. and & Haugen, H. J. Biological responses to physicochemical properties of biomaterial surface. *Chem. Soc. Rev.* **49**, (2020).
230. Lin, M. J. and C. K. Researches on biomechanical properties and models of peripheral nerves – A review. *J. Biomech. Sci* **12**, (2017).
231. G. H. Borschel, K. F. Kia, W. M. K. and R. G. D. Mechanical properties of acellular peripheral nerve. *J. Surg. Res.* **139**, (2003).
232. B. D. Stemper, D. Board, N. Y. and C. E. W. Biomechanical properties of human thoracic spine disc segments. *J. Craniovertebr. Junct. Spine*, **1**, (2010).
233. D. Wyrzykowski, E. Hebanowska, G. N.-W. & Chmurzyn´ski, M. M. and L. Thermal behavior of citric acid and isomeric aconitic acids. *J. Therm. Anal. Calorim* **104**, (2011).
234. J. Khouri, A. P. and C. M. Viscoelastic properties of crosslinked chitosan films. *Processes* **7**, (2019).
235. Bouropoulos, G. P. and N. Swelling studies and in vitro release of verapamil from calcium alginate and calcium alginate–chitosan beads,. *Int. J. Pharm.* (2006).
236. Y. Hong, H. Song, Y. Gong, Z. Mao, C. G. and J. S. Covalently crosslinked chitosan hydrogel: Properties of in vitro degradation and chondrocyte encapsulation. *Acta Biomater.* **3**, (2007).
237. G. Lu, L. Kong, B. Sheng, G. Wang, Y. G. and X. Z. Degradation of covalently cross-linked carboxymethyl chitosan and its potential application for peripheral nerve regeneration,. *Eur. Polym. J* **43**, (2007).
238. R. Nirmala, B. W. Il, R. Navamathavan, M. H. E.-N. & Kim, and H. Y. Preparation and characterizations of anisotropic chitosan nanofibers via electrospinning. *Macromol. Res* **19**, (2011).
239. W. Cao, D. Jing, J. Li, Y. Gong, N. Z. and X. Z. Effects of the degree of deacetylation on the physicochemical properties and Schwann cell affinity of chitosan films. *J. Biomater. Appl* **20**, (2005).
240. M. F. Queiroz, K. R. T. Melo, D. A. Sabry, G. L. S. and & Rocha, H. A. O. Does the use of chitosan contribute to oxalate kidney stone formation? *Mar. Drugs* **1**, (2015).
241. Y. Liu, X. Shen, H. Zhou, Y. W. and L. D. Chemical modification of chitosan film via surface grafting of citric acid molecular to promote the biomineralization,. *Appl. Surf. Sci* **370**, (2016).
242. D. Nataraj, S. Sakkara, M. M. and N. R. Crosslinked chitosan films with controllable properties for commercial applications. *nt. J. Biol. Macromol.* **120**, (2018).
243. A. Zajac, J. Hanuza, M. W. and L. D. ¸´ska. Determination of N-acetylation degree in chitosan using Raman spectroscopy. *Spectrochim. Acta, Part A Mol. Biomol. Spectrosc.*, **134**, (2015).

244. M. Kaya, T. Baran, I. Saman, M. A. O. & Mentes, Y. S. C. and A. Physicochemical characterization of chitin and chitosan obtained from resting eggs of ceriodaphnia quadrangula. *J. Crustac. Biol* **34**, (2014).

245. S. M. L. Silva, C. R. C. Braga, M. V. L. F. & C. M. O. Raposo, L. H. C. and E. L. C. Application of infrared spectroscopy to analysis of chitosan/clay nanocomposites. *Infrared Spectrosc. Mater. Sci. Eng. Technol.* (2012).

246. Klapetek, D. N. ˇas and P. Gwyddion: An open-source software for SPM data analysis. *Cent. Eur. J. Phys* (2012).

247. A. J. Steeves, A. Atwal, S. C. S. and F. V. Evaluation of the direct effects of poly(dopamine) on the: In vitro response of human osteoblastic cells. *J. Mater. Chem. B* **4**, (2016).

248. C. A. Rezende, L. T. L. and F. G. Surface mechanical properties of thin polymer films investigated by AFM in pulsed force mode. *Langmuir* **25**, (2009).

249. P. Tropel, N. Platet, J.-C. Platel, D. Noe ¨l, M. A. and & A.-L. Benabid, et al. Functional neuronal differentiation of bone marrow-derived mesenchymal stem cells. *Stem Cells* (2006).

250. K. C. Choi, D. S. Yoo, K. S. Cho, P. W. Huh, D. S. K. and & Park, C. K. Effect of single growth factor and growth factor combinations on differentiation of neural stem cells. *J. Korean Neurosurg. Soc.* **44**, (2008).

251. V. Brunetti, G. Maiorano, L. Rizzello, B. Sorce, S. S. & and R. Cingolani, et al. Neurons sense nanoscale roughness with nanometer sensitivity. *Proc. Natl. Acad. Sci. U. S. A.* **107**, (2010).

252. A. Ranella, M. Barberoglou, S. Bakogianni, C. F. and & Stratakis, E. Tuning cell adhesion by controlling the roughness and wettability of 3D micro/nano silicon structures. *Acta Biomater* **6**, (2010).

253. F. Ruini, C. Tonda-Turo, V. C. and G. C. Chitosan membranes for tissue engineering: Comparison of different crosslinkers. *Biomed. Mater.* **10**, (2015).

254. H. Park, K. P. and D. K. Preparation and swelling behavior of chitosan-based superporous hydrogels for gastric retention application. *J. Biomed. Mater. Res* (2006).

255. S. Bagheri-Khoulenjani, S. M. T. and H. M. An investigation on the short-term biodegradability of chitosan with various molecular weights and degrees of deacetylation. *Carbohydr. Polym.* (2009).

256. N. Kim, N. Minami, M. Y. and H. I. Immobilized pH in culture reveals an optimal condition for somatic cell reprogramming and differentiation of pluripotent stem cells. *Reprod. Med. Biol* (2017).

257. B. Yang, X. Y. Li, S. Shi, X. Y. Kong, G. G. and & M. J. Huang, et al. Preparation and characterization of a novel chitosan scaffold. *Carbohydr. Polym.* **80**, (2010).

258. Q. Li, X. Wang, X. Lou, H. Yuan, H. T. and B. L. Genipin-crosslinked electrospun chitosan nanofibers: Determination of crosslinking conditions and evaluation of cytocompatibility. *Carbohydr. Polym* **130**, (2015).

259. Kumar, S. Cellular mechanotransduction: Stiffness does matter,. *Nat. Mater.* **13**, (2014).
260. T. Yeung, P. C. Georges, L. A. Flanagan, B. Marg, M. O. & Funaki, and M. Effects of substrate stiffness on cell morphology, cytoskeletal structure, and adhesion. *Cell Motil Cytoskelet* **60**, (2005).
261. S. P. Lacour, R. Atta, J. J. FitzGerald, M. Blamire, E. T. & Fawcett, and J. Polyimide micro-channel arrays for peripheral nerve regenerative implants. *Sens. Actuators* (2008).
262. C. W. Li, B. Davis, J. Shea, H. Sant, B. K. G. and & J. Agarwal. Optimization of micropatterned poly(lacticcoglycolic acid) films for enhancing dorsal root ganglion. *Neural Regen. Res.* **13**, (2018).
263. B. W. Tuft, L. Zhang, L. Xu, A. Hangartner, B. L. and & M. R. Hansen. Material stiffness effects on neurite alignment to photopolymerized micropatterns. *Biomacromolecules* **15**, (2014).
264. A. Farrukh, S. Z. and A. del C. Microenvironments designed to support growth and function of neuronal cells. *Front. Mater.* **5**, (2018).
265. D. Tarus, L. Hamard, F. Caraguel, D. Wion, A. S. and B. V. D. S. Design of hyaluronic acid hydrogels to promote neurite outgrowth in three dimensions. *ACS Appl. Mater. Interfaces* **8**, (2016).
266. D. D. Deligianni, N. D. Katsala, P. G. K. and & Missirlis, Y. F. Effect of surface roughness of hydroxyapatite on human bone marrow cell adhesion, proliferation, differentiation and detachment strength. *Biomaterials* **22**, (2000).
267. M. J. Mahoney, R. R. Chen, J. T. and W. M. S. The influence of microchannels on neurite growth and architecture. *Biomaterials* **26**, (2005).
268. P. Clark, S. B. and P. C. Growth cone guidance and neuron morphology on micropatterned laminin surfaces. *J. Cell Sci* (1993).
269. D. Shahriari, G. Loke, I. Tafel, S. Park, P. H. C. and & Fink, Y. Scalable fabrication of porous microchannel nerve guidance scaffolds with complex geometries. *Adv. Mater.* **31**, (2019).
270. J. C. Clarke, B. W. Tuft, J. D. Clinger, R. Levine, L. S. F. & Hansen, C. A. G. and M. R. Micropatterned methacrylate polymers direct spiral ganglion neurite and Schwann cell growth. *Hear. Res* (2011).
271. Y. Sugimura-Wakayama, W. Katagiri, M. Osugi, T. K. & Sakaguchi, K. O. and K. Peripheral nerve regeneration by secretomes of stem cells from human exfoliated deciduous teeth. *Stem Cells Dev* **24**, (2015).
272. J. R. Fowler, M. Lavasani, J. H. and R. J. G. Biologic strategies to improve nerve regeneration after peripheral nerve repair,. *J. Reconstr. Microsurg* **31**, (2015).
273. R. A. Marklein and J. A. Burdick. patially controlled hydrogel mechanics to modulate stem cell interactions. *Soft Matter* **6**, (2009).
274. B. Venugopal, P. Mogha, J. D. and A. M. Cell density overrides the effect of substrate stiffness on human mesenchymal stem cells' morphology and proliferation. *Biomater. Sci.* **6**, (2018).

275. H. Sasaki, I. Takeuchi, M. Okada, R. S. Label-free morphology-based prediction of multiple differentiation potentials of human mesenchymal stem cells for early evaluation of intact cells. *PLoS One* **9**, (2014).
276. F. Matsuoka, I. Takeuchi, H. Agata, H. Kagami, H. S. & and Y. Kiyota. Morphology-based prediction of osteogenic differentiation potential of human mesenchymal stem cells. *PLoS One* **8**, (2013).
277. Y. Hou, W. Xie, L. Yu, L. C. Camacho, C. N. and M. Z. Surface roughness gradients reveal topography-specific mechanosensitive responses in human mesenchymal stem cells. *Small* (2020).
278. S. Martino, F. D'Angelo, I. Armentano, J. M. K. and & Orlacchio, A. Stem cell–biomaterial interactions for regenerative medicine. *Biotechnol. Adv* **30**, (2012).
279. X. Zhao, K. C. and Z. L. The role of biomaterials in stem cell-based regenerative medicine. *Futur. Med. Chem.* **11**, (2019).
280. P. G. Di Summa, P. J. Kingham, W. Raffoul, M. W. & Kalbermatten, G. T. and D. F. Adipose-derived stem cells enhance peripheral nerve regeneration. *Reconstr. Aesthetic Surg.* (2010).
281. X. Nie, Y. J. Zhang, W. D. Tian, M. Jiang, R. D. and & Chen, J. W. Improvement of peripheral nerve regeneration by a tissue-engineered nerve filled with ectomesenchymal stem cells. *Int. J. Oral Maxillofac. Surg* **36**, (2007).
282. C. Liu, Y. Zhong, A. A. and S. F. Neural differentiation of human embryonic stem cells as an in vitro tool for the study of the expression patterns of the neuronal cytoskeleton during neurogenesis. *Biochem. Biophys. Res. Commun.* **439**, (2013).
283. Y. W. Cho, D. S. Kim, I. R. Suhito, D. K. Han, T. L. and & Kim, T. H. Enhancing neurogenesis of neural stem cells using homogeneous nanohole pattern-modified conductive platform. *Int. J. Mol. Sci* **21**, (2010).
284. M. Li, W. Zhao, Y. Gao, P. Hao, J. Shang and H. Duan, et al. Differentiation of bone marrow mesenchymal stem cells into neural lineage cells induced by bFGF-chitosan controlled release system. *Biomed. Res. Int.* (2019).
285. F. Hu, X. Wang, G. Liang, L. Lv, Y. Z. and B. S. Effects of epidermal growth factor and basic fibroblast growth factor on the proliferation and osteogenic and neural differentiation of adipose-derived stem cells. *Cell Reprogr.* **15**, (2013).
286. D. Foudah, J. Redondo, C. Caldara, F. Carini, G. T. & Miloso, and M. Human mesenchymal stem cells express neuronal markers after osteogenic and adipogenic differentiation. *Cell Mol. Biol. Lett* **18**, (2013).
287. J. Deng, B. E. Petersen, D. A. Steindler, M. L. J. and & Laywell, E. D. Mesenchymal stem cells spontaneously express neural proteins in culture and are neurogenic after transplantation. *Stem Cells* **24**, (2006).
288. E. Y. Kim, K. B. Lee, J. Yu, J. H. Lee, K. J. K. and & K. W. Han, et al. Neuronal cell

differentiation of mesenchymal stem cells originating from canine amniotic fluid. *Hum. Cell*, **27**, (2014).

289. J. Lee, A. A. Abdeen, D. Z. and K. A. K. Directing stem cell fate on hydrogel substrates by controlling cell geometry, matrix mechanics and adhesion ligand composition. *Biomaterials* (2013).
290. G. J. Her, H. C. Wu, M. H. Chen, M. Y. Chen, S. C. C. and & T. W. Wang. Control of three-dimensional substrate stiffness to manipulate mesenchymal stem cell fate toward neuronal or glial lineages. *Acta Biomater.*, **9**, (2013).
291. A. J. Engler, S. Sen, H. L. S. and D. E. D. Matrix elasticity directs stem cell lineage specification. *Cell* **126**, (2006).
292. A. M. Loye, E. R. Kinser, B. Sabrine, M. Shayan, R. D. & Wang, and R. Regulation of mesenchymal stem cell differentiation by nanopatterning of bulk metallic glass. *Sci. Rep* (2018).
293. A. B. Faia-torres, M. Charnley, T. Goren, S. Guimondlischer, M. Rottmar and K. Maniura-weber, et al. Osteogenic differentiation of human mesenchymal stem cells in the absence of osteogenic supplements: A surfaceroughness gradient study. *Acta Biomater* **28**, (2015).
294. J. Zhang, X. Wei, R. Zeng, F. X. and X. L. Stem cell culture and differentiation in microfluidic devices toward organon-a-chip. *Futur. Sci. OA* **3**, (2017).
295. L. E. Monfoulet, P. Becquart, D. Marchat, K. V. & M. Bourguignon and E. Pacard. The pH in the microenvironment of human mesenchymal stem cells is a critical factor for optimal osteogenesis in tissueengineered constructs,. *Tissue Eng., Part A*, **20**, (2014).
296. Wenker, S. D. & Pitossi, F. J. Cell therapy for Parkinson′s disease is coming of age: current challenges and future prospects with a focus on immunomodulation. *Gene Ther.* **27**, (2020).
297. Guo, X., Tang, L. & Tang, X. Current Developments in Cell Replacement Therapy for Parkinson's Disease. *Neuroscience* (2021).
298. Elsworth, J. D. Parkinson's disease treatment: past, present and future. *J. Neural Transm.* **127**, (2020).
299. Gordián-Vélez, W. J. et al. Restoring lost nigrostriatal fibers in Parkinson's disease based on clinically-inspired design criteria. *Brain Res. Bull.* **175**, (2021).
300. Doblado, L. R., Martínez-Ramos, C. & Pradas, M. M. Biomaterials for Neural Tissue Engineering. *Front. Nanotechnol.* **3**, (2021).
301. Gu, X. Progress and perspectives of neural tissue engineering. *Front. Med.* **9**, (2015).
302. Liu, Z., Wan, X., Wang, Z. L. & Li, L. Electroactive Biomaterials and Systems for Cell Fate Determination and Tissue Regeneration: Design and Applications. *Adv. Mater.* **33**, (20221).
303. Roth, J. G. et al. Advancing models of neural development with biomaterials. *Nat. Rev. Neurosci.* **22**, (2022).
304. Liu, H. et al. An Electroconductive Hydrogel Scaffold with Injectability and Biodegradability to Manipulate Neural Stem Cells for Enhancing Spinal Cord Injury Repair. *Biomacromolecules*

24, (2023).

305. Gao, C., Song, S., Lv, Y., Huang, J. & Zhang, Z. Recent Development of Conductive Hydrogels for Tissue Engineering: Review and Perspective. *Macromol. Biosci.* **22**, (2022).
306. Xu, X. et al. Conductive Collagen-Based Hydrogel Combined With Electrical Stimulation to Promote Neural Stem Cell Proliferation and Differentiation. *Front. Bioeng. Biotechnol.* **10**, (2022).
307. Yang, S. et al. Polypyrrole/Alginate Hybrid Hydrogels: Electrically Conductive and Soft Biomaterials for Human Mesenchymal Stem Cell Culture and Potential Neural Tissue Engineering Applications. *Macromol. Biosci. 1* **16**, (2016).
308. Ko, W. K. et al. Direct Injection of Hydrogels Embedding Gold Nanoparticles for Local Therapy after Spinal Cord Injury. *Biomacromolecules* **22**, (2021).
309. Ye, L. et al. Carbon Nanotube–Hydrogel Composites Facilitate Neuronal Differentiation While Maintaining Homeostasis of Network Activity. *Adv. Mater.* **33**, (2021).
310. Kumar, R., Aadil, K. R., Ranjan, S. & Kumar, V. B. Advances in nanotechnology and nanomaterials based strategies for neural tissue engineering. *J. Drug Deliv. Sci. Technol.* (2020).
311. Samadian, H., Khastar, H., E. Bioengineered 3D nanocomposite based on gold nanoparticles and gelatin nanofibers for bone regeneration: in vitro and in vivo study. *Sci. Rep.* **11**, (2021).
312. Carlos Redondo-Gomez, Rocıo Leandro-Mora, D. B.-B. & Christopher Espinoza-Araya, D. & Hidalgo-Barrantes, and J. V.-B. Recent Advances in Carbon Nanotubes for Nervous Tissue Regeneration. *Adv. Polym. Technol.* (2020).
313. Barrejón, M. et al. TEGylated Double-Walled Carbon Nanotubes as Platforms to Engineer Neuronal Networks. *ACS Appl. Mater. Interfaces* (2022).
314. Ławkowska, K. et al. Application of graphene in tissue engineering of the nervous system. *J. Mol. Sci.* **23**, (2022).
315. Anirban, A. Fuzzy graphene for neuron control. *Nat. Rev. Phys.* **2**, (2020).
316. Seven, F. et al. Guiding neural extensions of PC12 cells on carbon nanotube tracks dielectrophoretically formed in poly(ethylene glycol) dimethacrylate. *RSC Adv.* **10**, (2020).
317. Marapureddy, S. G. et al. Rheology and direct write printing of chitosan - graphene oxide nanocomposite hydrogels for differentiation of neuroblastoma cells. *Carbohydr. Polym.* **269**, (2021).
318. Dominguez-Alfaro, A. et al. Toward Spontaneous Neuronal Differentiation of SH-SY5Y Cells Using Novel Three-Dimensional Electropolymerized Conductive Scaffolds. *ACS Appl. Mater. Interfaces* **12**, (2020).
319. Centeno, E. G. Z., Cimarosti, H. & Bithell, A. 2D versus 3D human induced pluripotent stem cell-derived cultures for neurodegenerative disease modelling. *Mol. Neurodegener.* **13**, (2018).
320. Rathore, R. S., R Ayyannan, S. & Mahto, S. K. Emerging three-dimensional neuronal culture assays for neurotherapeutics drug discovery. *Expert Opin. Drug Discov.* **17**, (2022).

321. Taylor-Whiteley, T. R., Le Maitre, C. L., Duce, J. A., Dalton, C. F. & Smith, D. P. Recapitulating Parkinson's disease pathology in a three-dimensional human neural cell culture model. *DMM Dis. Model. Mech.* (2019).
322. Ferrari, E., Cardinale, A., Picconi, B. & Gardoni, F. From cell lines to pluripotent stem cells for modelling Parkinson's Disease. *J. Neurosci. Methods* **340**, (2020).
323. Kumar, R., Kumar, V. B. & Gedanken, A. Sonochemical synthesis of carbon dots, mechanism, effect of parameters, and catalytic, energy, biomedical and tissue engineering applications. *Ultrason. Sonochem.* **64**, (2020).
324. Zeng, Q., Feng, T., Tao, S., Zhu, S. & Yang, B. Precursor-dependent structural diversity in luminescent carbonized polymer dots (CPDs): the nomenclature. *Light Sci. Appl.* **10**, (2021).
325. Pas, S. P. The rise of three-dimensional human brain cultures. *Nature* **553**, (2018).
326. Castellanos-Montiel, M. J. et al. An Optimized Workflow to Generate and Characterize iPSCDerived Motor Neuron (MN) Spheroids. *Cells* **12**, (2023).
327. Brüningk, S. C., Rivens, I., Box, C., Oelfke, U. & ter Haar, G. 3D tumour spheroids for the prediction of the effects of radiation and hyperthermia treatments. *Sci. Rep.* **10**, (2020).
328. Chan, M. H. et al. Natural carbon nanodots: Toxicity assessment and theranostic biological application. *Pharmaceutics* **13**, (2021).
329. Kang, K. S. et al. In-vitro cytotoxicity assessment of carbon-nanodot-conjugated Fe-aminoclay (CD-FeAC) and its bio-imaging applications. *J. Nanobiotechnology* **13**, (2015).
330. Lee, H. et al. Effect of carbon nanomaterial dimension on the functional activity and degeneration of neurons. *Biomaterials* **279**, (2021).
331. Gullekson, C., Lucas, L., Hewitt, K. & Kreplak, L. Surface-sensitive Raman spectroscopy of collagen I fibrils. *Biophys. J.* **100**, (2011).
332. Acri, G. et al. Preliminary study for the application of Raman spectroscopy for the identification of Leishmania infected dogs. *Sci. Rep.* (2022).
333. Bonifacio, A. & Sergo, V. Effects of sample orientation in Raman microspectroscopy of collagen fibers and their impact on the interpretation of the amide III band. *Vib. Spectrosc.* **53**, (2010).
334. Nguyen, T. T. et al. Characterization of type i and IV collagens by Raman microspectroscopy: Identification of spectral markers of the dermo-epidermal junction. *Spectrosc. (New York)* **27**, (2012).
335. Arshadi, C., Günther, U., Eddison, M., Harrington, K. I. S. & Ferreira, T. A. SNT: a unifying toolbox for quantification of neuronal anatomy. *Nat. Methods* **18**, (2021).
336. Macina, A., De Medeiros, T. V. & Naccache, R. A carbon dot-catalyzed transesterification reaction for the production of biodiesel. *J. Mater. Chem. A* (2019).
337. Wissink, M. J. B. et al. Immobilization of heparin to EDC/NHS-crosslinked collagen. Characterization and in vitro evaluation. *Biomaterials* (2001).

338. Nong, L. M. et al. The effect of different cross-linking conditions of EDC/NHS on type II collagen scaffolds: an in vitro evaluation. *Cell Tissue Bank.* **20**, (2019).
339. Nair, M., Johal, R. K., Hamaia, S. W., Best, S. M. & Cameron, R. E. Tunable bioactivity and mechanics of collagen-based tissue engineering constructs: A comparison of EDC-NHS, genipin and TG2 crosslinkers. *Biomaterials* (2020).
340. Kharlamova, M. V & Kramberger, C. Cytotoxicity of Carbon Nanotubes , Graphene , Fullerenes , and Dots. (2023).
341. Zakrzewska, K. E. et al. Analysis of the cytotoxicity of carbon-based nanoparticles, diamond and graphite, in human glioblastoma and hepatoma cell lines. *PLoS One* **10**, (2015).
342. Yuan, X., Zhang, X., Sun, L., Wei, Y. & Wei, X. Cellular Toxicity and Immunological Effects of Carbon-based Nanomaterials. *Part. Fibre Toxicol.* **16**, (2019).
343. Devasena, T. et al. Insights on the Dynamics and Toxicity of Nanoparticles in Environmental Matrices. *Bioinorg. Chem. Appl.* (2022).
344. Zhang, C., Cui, L., He, W., Zhang, X. & Liu, H. Dl-3-n-butylphthalide promotes neurite outgrowth of primary cortical neurons by Sonic Hedgehog signaling via upregulating Gap43. *Exp. Cell Res.* **398**, (2021).
345. Wang, Z. et al. PEITC promotes neurite growth in primary sensory neurons via the miR-17-5p/STAT3/GAP-43 axis. *J. Drug Target.* **27**, (2019).
346. Holahan, M. R. A shift from a pivotal to supporting role for the growth-associated protein (GAP-43) in the coordination of axonal structural and functional plasticity. *Front. Cell. Neurosci.* **11**, (2017).
347. Fang, Y. & Eglen, R. M. Three-Dimensional Cell Cultures in Drug Discovery and Development. *SLAS Discov.* **22**, (2017).
348. Dalgin, G. et al. Developmental defects and impaired network excitability in a cerebral organoid model of KCNJ11 p.V59M-related neonatal diabetes. *Sci. Rep.* **11**, (2021).
349. Park, S. Y. et al. Human Mesenchymal Stem Cell-Derived Extracellular Vesicles Promote Neural Differentiation of Neural Progenitor Cells. *Int. J. Mol. Sci.* (2022).
350. Santos, A. K. et al. Mouse Neural Stem Cell Differentiation and Human Adipose Mesenchymal Stem Cell Transdifferentiation Into Neuron- and Oligodendrocyte-like Cells With Myelination Potential. *Stem Cell Rev. Reports* **18**, (2022).
351. Szymańska-Chabowska, A., Świątkowski, F., Jankowska-Polańska, B., Mazur, G. & C. & M. Nestin Expression as a Diagnostic and Prognostic Marker in Colorectal Cancer and Other Tumors. *Clin. Med. Insights Oncol.* **15**, (2021).
352. Yao, H. et al. CHD7 promotes neural progenitor differentiation in embryonic stem cells via altered chromatin accessibility and nascent gene expression. *Sci. Rep.* **10**, (2020).
353. Armijo, E. et al. Induced pluripotent stem cell-derived neural precursors improve memory, synaptic and pathological abnormalities in a mouse model of alzheimer's disease. *Cells* **10**,

(2021).

354. Klincumhom, N. et al. Generation of neuronal progenitor cells and neurons from mouse sleeping beauty transposon-generated induced pluripotent stem cells. *Cell. Reprogram.* **14**, (2012).
355. Rajani, V., Sengar, A. S. & Salter, M. W. Tripartite signaling by NMDA receptors. *Front. Neurosci.* **13**, (2019).
356. Liao, M. et al. 3D Ti3C2TxMXene-Matrigel with Electroacoustic Stimulation to Promote the Growth of Spiral Ganglion Neurons. *ACS Nano* **16**, (2022).
357. Hartmann, J. et al. Alginate-Laminin Hydrogel Supports Long-Term Neuronal Activity in 3D Human Induced Pluripotent Stem Cell-Derived Neuronal Networks. *Adv. Mater. Interfaces* **10**, (2023).
358. Jarvis, C. R. et al. Neurotrophin modulation of NMDA receptors in cultured murine and isolated rat neurons. *J. Neurophysiol.* **78**, (1997).
359. Gao, Y. & Li, Z. Y. and X. Regeneration strategies after the adult mammalian central nervous system injury—biomaterials. *Regen. Biomater.* (2016).
360. Sakiyama-Elbert, R. T. and S. Using biomaterials to promote pro-regenerative glial phenotypes after nervous system injuries. *Biomed. Mater.* **13**, (2018).
361. Al., F. L. M. et. Biomaterial systems to resolve brain inflammation after traumatic injury. *APL Bioeng.* **2**, (2018).
362. Li, Wei, Qing Yuan Tang, Amol D. Jadhav, Ankit Narang, Wei Xian Qian, P. S. & Pang, & S. W. Large-scale Topographical Screen for Investigation of Physical Neural-Guidance Cues. *Sci. Rep.* (2015).
363. Wen-Hui Huang, et al. Collagen for neural tissue engineering: Materials, strategies, and challenges. *Mater. Today Bio* (2023).
364. Christopherson, Gregory T., et al. The influence of fiber diameter of electrospun substrates on neural stem cell differentiation and proliferation. *Biomaterials* **30**, (2009).
365. F. Yang, et al. Electrospinning of nano/micro scale poly(L-lactic acid) aligned fibers and their potential in neural tissue engineering. *Biomaterials* **26**, (2005).
366. Philip Lee, Rob Lin, J. M. & L. P. L. Microfluidic alignment of collagen fibers for in vitro cell culture. *Biomed. Microdevices Vol.* **8**, (2006).
367. Christopher M. Voge, Mihalis Kariolis, Rebecca A. MacDonald, J. P. S. Directional conductivity in SWNT-collagen-fibrin composite biomaterials through strain-induced matrix alignment. *J. Biomed. Mater. Res. - Part A* (2008).
368. Merav Antman-Passig, and O. S. Remote magnetic orientation of 3D collagen hydrogels for directed neuronal regeneration. *Nano Lett.* (2016).
369. Paul V. Taufalele, et al. Fiber alignment drives changes in architectural and mechanical features in collagen matrices. *PLoS One* **14**, (2019).
370. Li Xiao, et al. A novel culture platform for fast proliferation of human annulus fibrosus cells.

Cell Tissue Res (2017).

371. Cheng Guo, L. J. K. Flow and magnetic field induced collagen alignment. *Biomaterials* **28**, (2007).
372. A. Sainio, et al. Extracellular matrix-cell interactions: Focus on therapeutic applications. *Cell. Signal.* **66**, (2020).
373. Kaufman, J. Z. and L. J. Collagen I Self-Assembly: Revealing the Developing Structures that Generate Turbidity. *Biophys J* **106**, (2014).
374. F H Silver, D. E. B. Kinetic analysis of collagen fibrillogenesis: I. Use of turbidity--time data. *Coll Relat Res* . **3**, (1983).
375. Paul Thevenot, Jai Cho, Dattatray Wavhal, Ashwin Nair, Richard B. Timmons, L. T. Surface chemistry influences cancer killing effect of TiO2 nanoparticles. *Nanomedicine in Cancer* (2017).
376. Jin Qian, et al. Effects of polystyrene nanoplastics on extracellular polymeric substance composition of activated sludge: The role of surface functional groups. *Environ. Pollut.* **279**, (2021).
377. Wolfgang H. Goldmann. Role of vinculin in cellular mechanotransduction. *Cell Biol. Int.* (2015).
378. Alba Zuidema, Wei Wang, A. S. Crosstalk between Cell Adhesion Complexes in Regulation of Mechanotransduction. *BioEssays* (2020).
379. Mishra, Y. G. Focal adhesion dynamics in cellular function and disease. *Cell. Signal.* **85**, (2021).
380. Xuyan Li, et al. Effects of aligned and random fibers with different diameter on cell behaviors. *Colloids Surfaces B Biointerfaces* **171**, (2018).
381. Surabhi Shukla, B. L. T. Histone Deacetylases Inhibitors in Neurodegenerative Diseases, Neuroprotection and Neuronal Differentiation. *Front. Pharmacol* (2020).
382. Julián Esteban Sáez, et al. Decreased Expression of CoREST1 and CoREST2 Together with LSD1 and HDAC1/2 during Neuronal Differentiation. *PLoS One* (2015).
383. Sujeong Jang, et al. Histone deacetylase inhibition-mediated neuronal differentiation via the Wnt signaling pathway in human adipose tissue-derived mesenchymal stem cells. *Neurosci. Lett.* **668**, (2018).
384. Steffen Wedel, Lukasz Hudak, Jens-Michael Seibel, Jasmina Makarević, Eva Juengel, Igor Tsaur, Christoph Wiesner, Axel Haferkamp & Roman A. BlahetaSteffen Wedel, Lukasz Hudak, Jens-Michael Seibel, Jasmina Makarević, Eva Juengel, Igor Tsaur, Christoph Wiesn, A. H. & R. A. B. Impact of combined HDAC and mTOR inhibition on adhesion, migration and invasion of prostate cancer cells. *Clin. Exp. Metastasis* **28**, (2011).
385. Yong-Bae Kim, Sung-Yul Lee, Sang-Kyu Ye, and J. W. L. Epigenetic regulation of integrin-linked kinase expression depending on adhesion of gastric carcinoma cells. *Cell Physiol.* (2007).
386. Timothy L. Downing, et al. Biophysical Regulation of Epigenetic State and Cell

Reprogramming. *Nat Mater* **12**, (2013).

387. Yanfen Li, C. B. T. & K. A. K. Matrix Mechanics Influence Fibroblast–Myofibroblast Transition by Directing the Localization of Histone Deacetylase 4. *Cell. Mol. Bioeng.* **10**, (2017).
388. Genglei Chu, et al. Substrate stiffness- and topography-dependent differentiation of annulus fibrosus-derived stem cells is regulated by Yes-associated protein. *Acta Biomater.* **92**, (2019).
389. Genglei Chu, Weidong Zhang, Pinghui Zhou, Zhangqin Yuan, C. Z. Substrate Topography Regulates Differentiation of Annulus Fibrosus-Derived Stem Cells via CAV1-YAP-Mediated Mechanotransduction. *ACS Biomater. Sci. Eng.* **7**, (20121).
390. Misra, J. R., & Irvine, K. D. The Hippo signaling network and its biological functions. *Annu. Rev. Genet.* **52**, (2018).
391. Perestrelo, T., et al. Metabolic and mechanical cues regulating pluripotent stem cell fate. *Trends Cell Biol.* **22**, (2019).
392. Abolfazl Barzegari, et al. The role of Hippo signaling pathway and mechanotransduction in tuning embryoid body formation and differentiation. *Cell. Physiol.* (2019).
393. Naohiro Egawa, et al. Mechanisms of axonal damage and repair after central nervous system injury. *Transl Stroke Res* (2018).
394. Ben Kaplan, et al. The Role of Biomaterials in Peripheral Nerve and Spinal Cord Injury: A Review. *Int J Mol Sci.* **23**, (2022).
395. Monia Barnat, Hervé Enslen, Friedrich Propst, Roger J. Davis, S. S. and F. N. Distinct Roles of c-Jun N-Terminal Kinase Isoforms in Neurite Initiation and Elongation during Axonal Regeneration. *J. Neurosci.* **30**, (2010).
396. Alba C. de Luca, et al. Extracellular matrix components in peripheral nerve repair: how to affect neural cellular response and nerve regeneration? *Neural Regen Res.* **9**, (2014).
397. Shuo Tang, et al. The effects of gradients of nerve growth factor immobilized PCLA scaffolds on neurite outgrowth in vitro and peripheral nerve regeneration in rats. *Biomaterials* **34**, (2013).